Competition between Charge-Density-Wave and Antiferromagnetic Order in One-Dimension: Phase Diagram and Dynamics

Dissertation

zur Erlangung
des Doktorgrades der Naturwissenschaften
(Dr. rer. nat.)

dem Fachbereich Physik
der Philipps-Universität Marburg

vorgelegt von

Cornelius Mund

aus Marburg an der Lahn

Marburg an der Lahn, 2009

Vom Fachbereich der Physik der Philipps-Universität
als Dissertation angenommen am 2.11.2009
Erstgutachter: Prof. Dr. Reinhard Noack
Zweitgutachter: Prof. Dr. Peter Lenz

Tag der mündlichen Prüfung: 14.12.2009

Zusammenfassung

In unserer normalen Umgebung finden wir typischerweise ausschließlich Körper, die eine dreidimensionale Struktur aufweisen. Die Erklärung von elektronischen Phänomenen in solchen dreidimensionalen Strukturen war daher für eine lange Zeit der Hauptfokus der Festkörperphysik. Ein großer Durchbruch wurde auf diesem Gebiet im Jahre 1956 durch den russischen Physiker Lev Davidovich Landau erzielt. Er formulierte die Theorie der Fermi-Flüssigkeit. Diese besagt, dass bei niedrigen Temperaturen und für ausreichend kleine Anregungsenergien in einem Festkörper Quasiteilchen *entstehen* die eine direkte Korrespondenz zu den Elektronen in einem freien Elektronengas haben. Sie besitzen die selbe Ladung und den selben Spin wie die freien Elektronen, haben jedoch eine renormierte Masse und eine endliche Lebensdauer.

Die zunehmende Miniaturisierung in der modernen Industrie hat jedoch dazu geführt, dass man in vielen Anwendungen mit immer mehr Materialien in Kontakt kommt, die effektiv weniger als drei Dimensionen besitzen. So stellte man sehr bald fest, dass bei effektiv eindimensionalen Materialien die Fermiflüssigkeitstheorie gänzlich versagt. Dies ist in erster Linie darauf zurück zu führen, dass die Bewegungsmöglichkeiten von Teilchen in einer Dimension massiv eingeschränkt sind und daher eine Anregung eines Teilchens zwangsläufig auch eine Anregung der umgebenen Teilchen erzwingt. Dieses sehr spezielle Verhalten wurde im Jahre 1963 von Joaquin Mazdak Luttinger vorhergesagt. Er formulierte die Theorie der nach ihm benannten Luttinger-Flüssigkeit. Diese besagt, dass in einem eindimensionalen Material eine Aufspaltung der Freiheitsgrade in ein ladungstragendes und spinloses Quasiteilchen, das Holon, und in ein ladungsfreies, aber Spin tragendes Quasiteilchen, das Spinon, stattfindet.

Diese Aufspaltung in Spin- und Ladungsfreiheitsgrade wird deutlich bei der Betrachtung von winkelaufgelösten Spektralfunktionen. Die Eigenschaften dieser Spektralfunktion bestimmen zum Beispiel das Verhalten eines Materials unter Streuexperimenten wie der Photonen-, der Elektronen- oder der Neutronenstreuung. Auch optische und Leitungseigenschaften eines Materials sind durch seine Spektralfunktion bestimmt.

Diese Arbeit beschäftigt sich daher mit der Vorhersage von winkelaufgelösten Spektralfunktionen in verschiedenen Phasen von eindimensionalen Modellsystemen. Um eine solche Vorhersage zu ermöglichen, benötigen wir eine Methode um Modellsysteme, die die selben physkalischen Eigenschaften zeigen wie die tatsächlichen 10^{23}-Teilchen-großen Festkörper, effizient zu berechnen. Zu diesem Zweck entwickelte Steven White zu Beginn der 90er Jahre die Dichte-Matrix-Renomierungs-Gruppe. Dies ist eine numerische Methode zur Berechnung von Zuständen in eindimensionalen Modellsystemen. Im Rahmen dieser Arbeit wurden neue Methoden der Quanteninformationstheorie, nämlich die Quantenentropie, verwendet, um zuerst ein Phasendiagramm für ein bekanntes und grundlegendes quantenmechanisches Modell, das erweiterte Hubbard-Modell, zu etablieren. Im weiteren wurde die bereits erwähnte Dichte-Matrix-Renomierungs-Gruppe um die Funktionalität, die Zeitentwicklung von quantenmechanischen Zuständen zu berechnen, erweitert. Dies wurde dann genutzt, um winkelaufgelöste Spektralfunktionen in den verschiedenen im Modell vorkommenden Phasen zu berechnen. Die so erzeugten Daten können in Zukunft mit Ergebnissen aus Streuexperimenten verglichen werden und dienen so unter anderem zur Klassifizierung von Materialien in verschiedenen Modellklassen sowie zur Vorhersage von Eigenschaften der in die entsprechende Modellklasse gehörenden Materialien.

Contents

1 Introduction **1**

1.1 Structure of the Thesis 2

1.2 Publications 4

I Theory 5

2 Models **7**

2.1 Tight Binding Model 8

2.2 Hubbard Model 9

2.3 Common Extensions to the Hubbard Model 11

2.3.1 Extended Hubbard Model 11

2.3.2 Ionic Hubbard Model 13

2.3.3 Peierls Hubbard Model 13

2.3.4 The t-t' Hubbard model 14

3 Phenomena **15**

3.1 1D Physics 15

3.2 Phase Transitions 17

4 Measured Quantities **21**

4.1 Quantum Entropy 21

4.1.1 One-site entropy 23

4.1.2 Two-site entropy 24

4.1.3 Block entropy 25

4.2 Spectral Function & Density of States 25

4.2.1 Finite Systems 26

II Methods and Implementation 29

5 Evolution of the DMRG **33**

5.1 Exact Diagonalization 33
    5.1.1 Lanczos Diagonalization 33
    5.1.2 Davidson Diagonalization 35
5.2 The Renormalization Group 36
5.3 The Numerical Renormalization Group 38

6 DMRG **43**
6.1 Truncation Schemes 44
6.2 Quantum Numbers and Symmetries 45
6.3 DMRG Algorithms 46
    6.3.1 The Infinite System Algorithm 46
    6.3.2 The Finite System Algorithm 51
6.4 The Wave Function Transformation 52
6.5 Measurements 55

7 DMRG using Tensor Networks **57**
7.1 Tensors 57
7.2 Matrix Product States 59
7.3 Matrix Product Operators 60
7.4 Singular Value Decomposition 61
7.5 The DMRG Algorithm 62
7.6 Periodic Boundary Conditions 63
7.7 Two-Dimensional Systems 64
    7.7.1 Projected Entangled Pair States 66

8 Time Evolution **69**
8.1 Time Evolution Using Exact Diagonalization 69
8.2 Time Evolution Using Trotter Decomposition 70
8.3 Basis Adaptation 71

9 Dynamics **73**
9.1 Continued Fraction Method 74
9.2 Dynamical DMRG 74
9.3 Time Evolution and Fourier Transformation 76
    9.3.1 Extrapolation in Time 77
    9.3.2 Discrete Fourier Transform 78
9.4 Implementation Issues 83

III Results **85**

10 Tests **89**

11 Phases in the Extended Hubbard Model **93**
- 11.1 Computational Details . . . 93
- 11.2 Entropy Profiles . . . 94
- 11.3 The CDW-BOW Transition . . . 97
- 11.4 The BOW-SDW Transition . . . 98
- 11.5 Bond-Order-Parameter Results . . . 100
- 11.6 Phase Diagram and Discussion . . . 102

12 Spectral Functions and Density of States **105**
- 12.1 Computational Details . . . 105
- 12.2 The Spin-Density-Wave Phase . . . 106
- 12.3 The Charge-Density-Wave Phase . . . 116
- 12.4 The Transition Region . . . 124

13 Conclusion **137**
- 13.1 Achievements . . . 137
- 13.2 Outlook . . . 138

Appendices **141**

A Solution of the Tight Binding Model **143**

B Fourier Transformation of the Green's Function **149**

C Spectral Representation of the Green's Function **151**

D Continued Fraction Method **153**

Danksagung **163**

Lebenslauf **165**

List of Figures

2.1 Depiction of the t-t' Hubbard model as a system of two coupled chains. 14

5.1 Block-spin transformation on a two-dimensional square lattice. 37
5.2 The ground-state wave function for a particle on a tight binding chain for two 16-site blocks and one 32-sites block. 40

6.1 A pictorial representation of the finite system DMRG algorithm. 53

7.1 From left to right: A two-legged, three-legged, four-legged and five-legged tensor. 58
7.2 A matrix product state represented in terms of tensor diagrams. 59
7.3 A matrix product operator represented as a tensor diagram. . 60
7.4 A contracted pair of tensors corresponding to two sites. . . . 61
7.5 A four legged tensor with the indices combined to form a matrix. 62
7.6 The two tensors from Fig. 7.4 now disjoint. 62
7.7 Tensor network diagram of a Hamiltonian which only acts on two sites. 63
7.8 An MPS ring state, used to better represent a target state with periodic boundary conditions. 64
7.9 A superblock in a two-dimensional system. The system block has a red and the restblock a blue outline. Dashed lines stand for truncated, solid lines for full bases. 65
7.10 A PEPS state for a two-dimensional system. 66

9.1 Real and imaginary part of the example signal. 80
9.2 Real part of the inverse Fourier transform of the signal in Fig. 9.1. The red line denotes the artificial cut-off. 81

9.3 Fourier transform of signal shown in Fig. 9.2. The Fourier transform of the full signal, the truncated signal and the truncated signal multiplied with a Kaiser filter function are as indicated in the legend. 82

10.1 Angle-resolved spectral function of the Hubbard model for $U/t = 7.74$. (a) Results from Jeckelmann et al. [1] and (b) results obtained in this thesis. 90
10.2 The density of states for the half-filled Hubbard model with $U/t = 7.74$. 91

11.1 Two-site entropy $S_{N/2+1}(2)$ for $V/t = 3$, plotted as a function of U/t. System sizes range from $N = 64$ to $N = 512$ sites. . . 95
11.2 Block entropy at the center of the chain $S(N/2+1)$ for $V/t = 3$ and system sizes from $N = 64$ to $N = 512$ sites. 96
11.3 Finite-size extrapolation of the peaks in Figs. 11.1 and 11.2 to the thermodynamic limit, $1/L \to 0$, using fourth order polynomials in $1/L$. “2s” labels the two-site entropy and “B” the block entropy. 97
11.4 Extrapolated one-site entropy $S_{N/2}(1)$ plotted as a function of U/t for various values of V/t. 98
11.5 The phase diagram in the tilted U-V-plane, showing phase boundaries determined using the two-site entropy (2s), the block entropy (B), and including results from Ref. [2], determined from QMC calculations. 99
11.6 Bond order parameter B extrapolated to the thermodynamic limit using fits to three different functions: fit to a third-order polynomial in $1/N$ (Poly), fit to a third-order polynomial in $1/\sqrt{N}$ (Sqrt Poly), and fit to a power law $1/N^{\alpha}$ (Power-law) with α a fitting parameter, plotted as a function of U/t. The vertical lines indicate the transition point determined using the two-site entropy (2s) and the block entropy (B). 101
11.7 The phase diagram in the U-V-Plane obtained from our calculations. On this scale, uncertainties in the position of the transition lines are smaller or about the size of the symbols. The phase in the narrow region between the two transition lines is BOW. 103

12.1 A simplified depiction of a SDW. 107
12.2 Angle-resolved spectral function $A(k,\omega)$ of the half-filled extended Hubbard model at $U/t = 8$ and V/t from 0.5 to 1. . . 108

12.3 Angle-resolved spectral function $A(k, \omega)$ of the half-filled extended Hubbard model at $U/t = 8$ and V/t from 1.5 to 2. . . 109
12.4 Angle-resolved spectral function $A(k, \omega)$ of the half-filled extended Hubbard model at $U/t = 8$ and V/t from 2.5 to 3. . . 110
12.5 Angle-resolved spectral function $A(k, \omega)$ of the half-filled extended Hubbard model at $U/t = 8$ and V/t from 3.5 to 4. . . 111
12.6 Density of states $N(\omega)$ of the half-filled extended Hubbard model at $U/t = 8$ and V/t from 0.5 to 1. 112
12.7 Density of states $N(\omega)$ of the half-filled extended Hubbard model at $U/t = 8$ and V/t from 1.5 to 2. 113
12.8 Density of states $N(\omega)$ of the half-filled extended Hubbard model at $U/t = 8$ and V/t from 2.5 to 3. 114
12.9 Density of states $N(\omega)$ of the half-filled extended Hubbard model at $U/t = 8$ and V/t from 3.5 to 4. 115
12.10 Simplified depiction of a CDW phase. 116
12.11 Angle-resolved spectral function $A(k, \omega)$ of the half-filled extended Hubbard model for $V/t = 4$ and U/t from 1 to 2. . . . 118
12.12 Angle-resolved spectral function $A(k, \omega)$ of the half-filled extended Hubbard model for $V/t = 4$ and U/t from 3 to 4. . . . 119
12.13 Angle-resolved spectral function $A(k, \omega)$ of the half-filled extended Hubbard model for $V/t = 4$ and U/t from 5 to 6. . . . 120
12.14 Density of states $N(\omega)$ of the half-filled extended Hubbard model for $V/t = 4$ and U/t from 1 to 2. 121
12.15 Density of states $N(\omega)$ of the half-filled extended Hubbard model for $V/t = 4$ and U/t from 3 to 4. 122
12.16 Density of states $N(\omega)$ of the half-filled extended Hubbard model for $V/t = 4$ and U/t from 5 to 6. 123
12.17 Angle-resolved spectral function $A(k, \omega)$ of the half-filled extended Hubbard model for $V/t = 4$ and U/t from 7 to 7.25. . 125
12.18 Angle-resolved spectral function $A(k, \omega)$ of the half-filled extended Hubbard model for $V/t = 4$ and U/t from 7.5 to 7.77. 126
12.19 Angle-resolved spectral function $A(k, \omega)$ of the half-filled extended Hubbard model for $V/t = 4$ and U/t from 7.86 to 8. . 127
12.20 Density of states $N(\omega)$ of the half-filled extended Hubbard model for $V/t = 4$ and U/t from 7 to 7.25. 128
12.21 Density of states $N(\omega)$ of the half-filled extended Hubbard model for $V/t = 4$ and U/t from 7.5 to 7.77. 129
12.22 Density of states $N(\omega)$ of the half-filled extended Hubbard model for $V/t = 4$ and U/t from 7.86 to 8. 130
12.23 Angle-resolved spectral function $A(k, \omega)$ of the half-filled extended Hubbard model for $V/t = 3$ and U/t from 5 to 5.75. . 131

12.24 Angle-resolved spectral function $A(k, \omega)$ of the half-filled extended Hubbard model for $V/t = 3$ and U/t from 6 to 7. . . . 132
12.25 Angle-resolved spectral function $A(k, \omega)$ of the half-filled Hubbard model at $U/t = 2$. 133
12.26 Density of states $N(\omega)$ of the half-filled extended Hubbard model for $V/t = 3$ and U/t from 5 to 5.75. 134
12.27 Density of states $N(\omega)$ of the half-filled extended Hubbard model for $V/t = 3$ and U/t from 6 to 7. 135

List of Tables

3.1 Commonly used critical exponents for a magnetic system. . . . 19

5.1 Lowest energies after 10 block size increases for the single particle on a tight binding chain keeping the 8 lowest states as a basis [3]. 41

Chapter 1

Introduction

A central issue in natural sciences such as chemistry, materials science, and physics is understanding and predicting the relations between material properties on the one hand and their structure and composition on the other. The exact knowledge of these relations would allow one to construct materials in such a way that they exhibit all properties that one deems desirable and none of those which are deemed undesirable in a given context.

Since the field of solid state physics is, as far as we know, completely described by quantum mechanics, we could, in principle, exactly determine all of the properties of any given material by solving the time dependent Schroedinger equation

$$i\hbar\frac{\partial\psi}{\partial t} = \left(-\sum_{i=1}^{N} \frac{\hbar^2}{2m_i}\nabla_i^2 + \sum_{\substack{i,j=1 \\ i<j}}^{N} V_{i,j}(|\vec{r}_i - \vec{r}_j|) \right)\psi \tag{1.1}$$

for the many-particle wave function $\psi(\vec{r}_1, \ldots, \vec{r}_N, t)$. Here i runs over all particles in the system and $V_{i,j}$ describes the interaction between particle i and particle j.

Unfortunately, due to the number of particles that are present in a typical material ($N > 10^{22}$), this knowledge is generally not particularly useful because finding an analytic solution of the full Schroedinger equation (1.1) has proven to be almost impossible even for relatively simple choices of $V_{i,j}$. The only option one is left with in these cases is to drastically simplify the problem at hand by making approximations which leave the interesting physics intact while dramatically reducing the level of complication and therefore allowing for an analytical or numerical solution of the problem.

In recent years, a number of methods have made it possible to produce many additional materials with lower dimensionality than that of our three-dimensional surroundings. In these zero-, one-, and two-dimensional materials, one commonly encounters properties and electronic structures that differ tremendously from those of truly three-dimensional materials. Since such low-dimensional materials include, for example, quantum dots, quantum wires, modern semiconductors, high-temperature superconductors, and fullerene nanotubes, they find application in many modern device starting from superconducting wires as the means to transport current up to the most efficient solar cells and the most advanced CPUs.

While approximative techniques work reasonably well in many cases, for three-dimensional materials, this is, unfortunately, typically not the case in one dimension due to the collective nature of the excitations. In the limit of extremely low excitation energies, the Luttinger-liquid theory describes the dynamics of these systems very well, but for almost all other non-trivial cases, it turns out that one needs to treat the full problem of interacting electrons because neglecting or strongly approximating the electron-electron interaction yields results which deviate qualitatively from experimental data.

Over the last 15 years, it has turned out that numerical methods are especially well-suited for calculating the properties of one-dimensional models to very high precision. One of these methods, the Density Matrix Renormalization Group (DMRG) [4, 5], is extended and then used as part of this thesis to calculate dynamical correlation functions, which are then used to predict angle resolved spectral functions and density of states for one-dimensional systems.

1.1 Structure of the Thesis

This thesis consists of three main parts.

Part I. The first part gives an introduction to the basic theory that governs one-dimensional many-body physics. Chapter 2 introduces the most important models that are used to describe one-dimensional systems and outlines their most important properties. Various extensions to these models and their effect on the underlying physics are explained briefly.

Chapter 3 deals with the most important effects that are present in one-dimensional systems and contrasts them to the behavior of three-dimensional systems. The concept of a Luttinger-liquid is explained and its derivation is outlined briefly. Here different quantum phases are explained as well as what kind of phase transitions can occur at zero temperature and why.

In Chapter 4, the various measured quantities that have been calculated in this thesis are explained in detail, and a short discussion of why these are sensible quantities to measure and how they can be used is given. Also briefly discussed are what assumptions have to be made to be able to use the calculated data for finite systems to make reasonable predictions for macroscopic (infinite) systems.

Part II. In Part II of this thesis, the methods and algorithms developed and used to calculate the results presented here are discussed in detail. Chapter 5 gives an introduction to the DMRG and explains how it came to be. It outlines the evolution of different algorithms into what we know today as the DMRG and points out what advantages the DMRG has over its predecessors.

Chapter 6 gives a detailed insight into how the DMRG works. In this chapter we also address various implementation issues, give detailed explanations of the two main DMRG algorithms, and point out various problems that standard DMRG implementations have to cope with.

In Chapter 7, we discuss recent developments in DMRG-related methods. We show that these new developments not only make it easier to understand and implement the standard DMRG algorithm, but also partially succeed in eliminating some of the problems mentioned in the previous chapter. This chapter should also allow the reader to gain a more intuitive understanding of how and why the DMRG works.

Chapter 8 explains how the DMRG algorithm can be extended to allow for the evolution of a given quantum state in time. It describes the two most widely-used algorithms, one of which has been implemented as part of this thesis, and also discusses the pitfalls related to calculating time evolution within the DMRG.

In Chapter 9, we discuss how to further extend the time evolution scheme explained in the previous chapter to allow for the calculation of dynamical correlation functions, a method also implemented as part of this thesis. We explain the necessary additions and modifications to the existing algorithm and outline what problems can arise and why.

Part III. In the last part of this thesis, we describe the results obtained using the methods that have been implemented here. Chapter 10 starts by comparing results obtained from the newly implemented methods to results calculated for the same model with the same parameters but using an entirely different algorithm which is based on a minimization principle, thereby demonstrating the validity of the method used here.

Chapter 11 gives a detailed picture of the phase diagram in the one-dimensional half-filled extended Hubbard model which has been obtained using quantum information entropy measurements. Also discussed briefly is why other, more straightforward measures fail.

In Chapter 12, we present the density of states and the angle resolved spectral functions for the different phases which occur in the extended Hubbard model. We also explain their most prominent features and how they depend on the values of the model parameters.

Finally we summarize and discuss our newly found results and conclude with an outlook covering physical and numerical challenges in Chapter 13.

1.2 Publications

Some parts of this thesis have already been published or are being prepared for publication at the time of writing. The related publications are:

- *Quantum information analysis of the phase diagram of the half-filled extended Hubbard model*

  C. Mund, Ö. Legeza, and R. M. Noack

  Physical Review B 79, 245130 (2009)

- *Dynamics of the half-filled extended Hubbard model*

  C. Mund and R. M. Noack

  in preparation

Part I

Theory

Chapter 2

Models

In the field of solid state physics, one usually has to deal with an extremely large number of atoms, each of which is composed of a nucleus and of electrons. To find an exact solution for any state in a material, all of theses particles and their mutual interactions would have to be described by a Hamiltonian, which would then, in turn, have to be solved exactly. While the formulation of such a Hamiltonian is, in principle, possible, solving it is not.

Therefore, the first step to finding reasonable and calculable results is finding sensible approximations to the full Hamiltonian which simplify calculations as much as possible while still retaining the important physics. One of the most common approximations is the single-particle approximation, e.g., Hartree or Hartree-Fock [6], where it is assumed that the interactions between the aforementioned particles are weak enough so that it is reasonable to assume that the influence of a particular particle on the other particles is so small that the induced change in the other particles will in turn have a negligible influence on the first particle. In these cases the particle in focus can be viewed as moving in a static potential caused by all the other particles. The field of strongly interacting systems however concerns itself with those kinds of materials where these interactions between different particles are *so* strong that such an approximation leads to qualitatively wrong results. In these cases different approximations have to be found. Two of the most straightforward approximation which are possible are:

The Born Oppenheimer Approximation [7] makes use of the high ratio between nuclear and electronic masses. It assumes that due to this high ratio it is sensible to think about the nuclei as stationary in comparison to the electrons. Because of that the full wave function can be considered a product of the electronic wave function and the nuclear wave function.

$$|\psi\rangle = |\psi\rangle_{\text{nuclear}} \otimes |\psi\rangle_{\text{electronic}} \tag{2.1}$$

Hence if one is only interested in the electronic behaviour of a material one can treat the nuclear part of the wave function as being constant in time and only calculate the electronic part. Other effects that are excluded by the Born Oppenheimer approximation such as vibrations of the lattice can usually be treated by adding phonons to the system as long as they are comparably small.

The Tight-Binding Approximation assumes that one can, in principle, divide electrons into two classes. Those which are tightly bound to a specific atomic site are called core electrons. These electrons are basically fixed to their respective atomic site and are therefore of negligible importance for the calculation. The other class, the valence electrons, are loosely bound to their respective atomic sites and have the possibility of tunneling between the different sites which is usually referred to as *hopping*. With these two approximations one arrives at the tight binding model [8].

2.1 Tight Binding Model

The tight binding model treats the aforementioned valence electrons as being localized at particular sites and usually only allows for nearest-neighbor hopping between those sites with a set hopping amplitude t. As an example the Hamiltonian for a one-dimensional tight binding model with N sites is given below in second quantization formulation.

$$H_{tb} = -t \sum_{i=1}^{N-1} \sum_{\sigma=\uparrow,\downarrow} \left(c^\dagger_{i+1,\sigma} c_{i,\sigma} + c^\dagger_{i,\sigma} c_{i+1,\sigma} \right) . \tag{2.2}$$

Here the operators $c^\dagger_{i,\sigma}/c_{i,\sigma}$ create/annihilate an electron on site i with spin σ, and t is the hopping amplitude, which corresponds directly to the overlap between the different atomic orbitals and therefore to the kinetic energy in the system.

Here and in the remainder of this thesis units will be used so that $\hbar = 1$ and so that the lattice spacing a is set to unity. The operators $c^\dagger_{i,\sigma}$ and $c_{i,\sigma}$ fulfill the usual fermionic anti-commutation relations.

$$\begin{aligned}\left[c^\dagger_{i,\sigma}, c_{j,\sigma'}\right]_+ &= \delta_{i,j}\,\delta_{\sigma,\sigma'} \\ \left[c^\dagger_{i,\sigma}, c^\dagger_{j,\sigma'}\right]_+ &= \left[c_{i,\sigma}, c_{j,\sigma'}\right]_+ = 0,\end{aligned} \tag{2.3}$$

where $[\cdots]_+$ denotes anti-commutators.

A complete analytic solution of Hamiltonian (2.2) is possible through Fourier transformation which translates the operators into momentum space and is given in appendix A. Since the tight binding model is one of the very few models which are solvable exactly and, in the case of the one-dimensional tight binding model, with relative ease, it can be very useful for comparison with numerically generated data to verify the proper functioning of one's algorithm.

2.2 Hubbard Model

One of the most straightforward extensions to the tight binding model is to take into account the Coulomb interaction between the different electrons. In the simplest case, only interactions local to each site are taken into account. This yields the Hubbard model, which was proposed independently by Gutzwiller [9], Kanamori [10], and Hubbard [11] in 1963. The Hubbard Hamiltonian, given here for a one dimensional chain with 2 spin species ($\uparrow, \downarrow$), is

$$H_{\text{Hub}} = -t \sum_{i=1}^{N-1} \sum_{\sigma=\uparrow,\downarrow} \left(c^\dagger_{i+1,\sigma} c_{i,\sigma} + c^\dagger_{i,\sigma} c_{i+1,\sigma} \right) + U \sum_{i=1}^{N-1} n_{i,\uparrow} n_{i,\downarrow}. \tag{2.4}$$

The first term is the same kinetic energy term as in the tight binding model (2.2). The second term in the sum is the on-site interaction, where $n_{i,\sigma}$ is the number operator $\left(n_{i,\sigma} = c^\dagger_{i,\sigma} c_{i,\sigma}\right)$.

Despite its apparent simplicity, the one-dimensional Hubbard model already contains an abundance of physical phenomena, some of which will be outlined in Section 3.1. It is believed that the two-dimensional Hubbard model captures the physics that is necessary to explain High T_c superconductivity, even though this is not proven yet [12]. Although it has not been possible so far to solve the two-dimensional Hubbard model analytically and even numerical access is very limited, the one-dimensional Hubbard model has been solved analytically via Bethe-Ansatz [13].

Two important properties of the Hubbard model that can easily be deduced starting from the formulation of the Hamiltonian (2.4) are going to be explained in the following.

Spin rotational symmetry describes the fact that the Hamiltonian is invariant under spin rotations. We can, for example, consider a spin inversion function

$$
\begin{aligned}
f_{sc}: \quad \mathrm{End}_{\mathbb{C}}(\mathcal{F}) &\longrightarrow \mathrm{End}_{\mathbb{C}}(\mathcal{F}) \\
c_{i,\uparrow} &\longmapsto c_{i,\downarrow} \\
c_{i,\downarrow} &\longmapsto c_{i,\uparrow} \\
c^{\dagger}_{i,\uparrow} &\longmapsto c^{\dagger}_{i,\downarrow} \\
c^{\dagger}_{i,\downarrow} &\longmapsto c^{\dagger}_{i,\uparrow},
\end{aligned}
\tag{2.5}
$$

where $\mathrm{End}_{\mathbb{C}}(\mathcal{F})$ denotes the space of endomorphisms of Fock space $\mathcal{F}$ over the field $\mathbb{C}$.

It can then be easily seen that the Hubbard Hamiltonian (2.4) is invariant under this transformation function, due to the commutative property of the summation and bosonic character of the number operator. Hence

$$
f_{sc}\left(H_{\mathrm{Hub}}\right) = H_{\mathrm{Hub}}. \tag{2.6}
$$

Since no particular spin direction stands out, we are not only restricted to spin inversions but arbitrary rotations in spin space work as well. Since the group of rotations in spin space is represented by unitary 2x2 matrices with a determinant of 1, this kind of symmetry is commonly referred to as SU(2) symmetry.

Particle-hole symmetry is the name for the fact that in the case of half-filling the Hubbard Hamiltonian (2.4) is invariant under a particle hole transformation defined as

$$
\begin{aligned}
f_{ph}: \quad \mathrm{End}_{\mathbb{C}}(\mathcal{F}) &\longrightarrow \mathrm{End}_{\mathbb{C}}(\mathcal{F}) \\
c_{i,\sigma} &\longmapsto (-1)^{i}\, c^{\dagger}_{i,\sigma} \\
c^{\dagger}_{i,\sigma} &\longmapsto (-1)^{i}\, c_{i,\sigma}.
\end{aligned}
\tag{2.7}
$$

This is easily seen because

$$
\begin{aligned}
f_{ph}\left(H_{\text{Hub}}\right) &= -t\sum_{i=1}^{N-1}\sum_{\sigma}\left(-c_{i+1,\sigma}c_{i,\sigma}^{\dagger}-c_{i,\sigma}c_{i+1,\sigma}^{\dagger}\right)+U\sum_{i=1}^{N}c_{i,\uparrow}c_{i,\uparrow}^{\dagger}c_{i,\downarrow}c_{i,\downarrow}^{\dagger}\\
&= -t\sum_{i=1}^{N-1}\sum_{\sigma=\uparrow,\downarrow}\left(c_{i+1,\sigma}^{\dagger}c_{i,\sigma}+c_{i,\sigma}^{\dagger}c_{i+1,\sigma}\right)+U\sum_{i=1}^{N}\left(1-n_{i,\uparrow}\right)\left(1-n_{i,\downarrow}\right)\\
&= -t\sum_{i=1}^{N-1}\sum_{\sigma=\uparrow,\downarrow}\left(c_{i+1,\sigma}^{\dagger}c_{i,\sigma}+c_{i,\sigma}^{\dagger}c_{i+1,\sigma}\right)+U\sum_{i=1}^{N}\left(1-n_{i,\uparrow}-n_{i,\downarrow}+n_{i,\uparrow}n_{i,\downarrow}\right)\\
&= H_{\text{Hub}}+\underbrace{UN-U\hat{N}}_{=0},
\end{aligned}
$$

where $\hat{N}$ is the number operator while N denotes the number of lattice sites. One should note that $UN-U\hat{N}=0$ only holds true at half-filling.

The particle hole symmetry of the Hubbard Hamiltonian (2.4) is also the reason for its density of states being reflection symmetric around $U/2$. This symmetry is due to the fact that the process of creating a hole and creating an electron are equivalent; therefore, the upper and the lower Hubbard band necessarily have to be indistinguishable. This reflection symmetry is also used in Chapter 10 as a test for the validity of our method.

2.3 Common Extensions to the Hubbard Model

In this section we will examine the most common extensions that can be made to the Hubbard Hamiltonian and some of the physical results which those yield.

2.3.1 Extended Hubbard Model

In the extended Hubbard model, an additional term is added to the Hubbard Hamiltonian which introduces nearest-neighbor Coulomb interaction. The Hamiltonian of the one-dimensional extended Hubbard model reads

$$
\begin{aligned}
H_{eH} = -t\sum_{i=1}^{N-1}\sum_{\sigma=\uparrow,\downarrow}&\left(c_{i+1,\sigma}^{\dagger}c_{i,\sigma}+c_{i,\sigma}^{\dagger}c_{i+1,\sigma}\right)\\
&+U\sum_{i=1}^{N-1}n_{i,\uparrow}n_{i,\downarrow}\\
&+V\sum_{i=1}^{N-1}n_{i+1}n_{i},
\end{aligned}
\tag{2.8}
$$

where $n_i = n_{i,\uparrow} + n_{i,\downarrow}$ is the density operator on site i. The addition of a nearest-neighbor interaction leads to a much richer phase diagram which includes a charge-density-wave (CDW) phase for $U \ll 2V$, a spin-density-wave phase (SDW) for $U \gg 2V$, and even a bond-order-wave phase (BOW) for appropriate values of U and V around $U \approx 2V$ [2, 14].

The CDW phase is characterized by a modulated charge density ρ_0. In the hopping $t \longrightarrow 0$ limit on a periodic lattice with open boundary conditions at half filling one would find alternating doubly occupied and empty sites. The CDW phase is an insulating phase with non-zero charge and spin gaps which are in the $t \longrightarrow 0$ limit easily determined to be equal to $4V$ and $3V - U$ respectively. The order parameter associated with a CDW phase is

$$m_c = \frac{1}{N} \sum_{i=1}^{N} (-1)^i \langle n_i \rangle \,, \tag{2.9}$$

where $n_i = n_{i,\uparrow} + n_{i,\downarrow}$. Also $\langle \cdot \rangle$ denotes here and from hereon out the ground state expectation value.

The SDW phase is like the CDW phase a density-wave phase, but

$$\rho_{\uparrow(\downarrow)}(\vec{r}) = \frac{1}{2}\rho_0(\vec{r}) \left[1 \pm A \cos(\vec{Q} \cdot \vec{r}) \right] , \tag{2.10}$$

rather than the charge density. Here A is the amplitude and $\vec{Q}$ is the wave vector of the spin density wave. The SDW phase has a finite charge gap which is equal to U in the $t \longrightarrow 0$ limit but has a vanishing spin gap. The order parameter associated with a SDW phase is

$$m_s = \frac{1}{N} \sum_{i=1}^{N} (-1)^i \langle n_{i,\uparrow} - n_{i,\downarrow} \rangle \,. \tag{2.11}$$

The BOW phase displays an alternating pattern in the kinetic bond energy. It typically appears as a transitional phase between a CDW and a SDW phase [2, 15]. It has a finite spin and charge gap and the associated order parameter is

$$m_{\mathrm{BO}} = \frac{1}{N} \sum_{i=1,\sigma}^{N-1} (-1)^i \left\langle c^\dagger_{i+1,\sigma} c_{i,\sigma} + c^\dagger_{i,\sigma} c_{i+1,\sigma} \right\rangle . \tag{2.12}$$

All of these phases appear for positive U and V, i.e., for repulsive on-site and nearest-neighbor interaction, respectively. For negative U and V, the phase diagram also includes a variety of superconducting phases [16].

2.3.2 Ionic Hubbard Model

The Ionic Hubbard model features an additional alternating on-site potential. Such a potential is, as the name suggests, appropriate for ionic lattices with two alternating species of atoms. The Hamiltonian for the Ionic Hubbard model reads

$$\begin{aligned} H_{eH} = -t \sum_{i=1}^{N-1} \sum_{\sigma=\uparrow,\downarrow} \left(c^\dagger_{i+1,\sigma} c_{i,\sigma} + c^\dagger_{i,\sigma} c_{i+1,\sigma} \right) \\ +U \sum_{i=1}^{N-1} n_{i,\uparrow} n_{i,\downarrow} + \frac{\delta}{2} \sum_{i=1}^{N} \sum_{\sigma=\uparrow,\downarrow} (-1)^i \, n_{i,\sigma}. \end{aligned} \tag{2.13}$$

Interestingly enough the alternating on-site potential has a very similar physical effect to a repulsive nearest-neighbor interaction. It can be seen fairly easily by examining the $t \to 0$ limit that the system will be in a CDW phase for $U \ll \delta$ and in a SDW phase for finite t and $U \gg \delta$. It has also been shown [15] that a BOW phase emerges for appropriate values of U and δ between those two phase.

2.3.3 Peierls Hubbard Model

The Peierls Hubbard Model is used to model a dimerized lattice in which the distance between two atoms is alternating. Its Hamiltonian is

$$\begin{aligned} H_{\mathrm{PH}} = -t \sum_{i=1}^{N-1} \sum_{\sigma=\uparrow,\downarrow} \left(1 + (-1)^i \frac{\delta}{2} \right) \left(c^\dagger_{i+1,\sigma} c_{i,\sigma} + c^\dagger_{i,\sigma} c_{i+1,\sigma} \right) \\ +U \sum_{i=1}^{N-1} n_{i,\uparrow} n_{i,\downarrow}, \end{aligned} \tag{2.14}$$

with $\delta < 2$. In the $U = 0$ limit, the alternating hopping amplitude causes the previously metallic tight binding energy dispersion to split up into an upper and a lower Peierls band and therefore become an insulator at half filling. Since there is an energy gain associated with the lowering of the lower Peierls band near the gap, the dimerization of a lattice can happen spontaneously if the energy savings due to the lowering of the lower Peierls band outweighs the energy cost of rearranging the atoms. This is commonly referred to as the Peierls transition [17].

2.3.4 The t-t' Hubbard model

The t-t' Hubbard model is a Hubbard model with additional next-nearest-neighbour hopping. Its Hamiltonian is

$$\begin{aligned} H_{t\text{-}t'} = -t\sum_{i=1}^{N-1}\sum_{\sigma=\uparrow,\downarrow}\left(c^\dagger_{i+1,\sigma}c_{i,\sigma}+c^\dagger_{i,\sigma}c_{i+1,\sigma}\right) \\ -t'\sum_{i=1}^{N-2}\sum_{\sigma=\uparrow,\downarrow}\left(c^\dagger_{i+2,\sigma}c_{i,\sigma}+c^\dagger_{i,\sigma}c_{i+2,\sigma}\right) \\ +U\sum_{i=1}^{N-1}n_{i,\uparrow}n_{i,\downarrow}. \end{aligned} \tag{2.15}$$

This model can either be regarded as a chain of atoms with a finite probability for an electron to hop two sites at once, which makes sense for $t' \ll t$, or as a system of two coupled chains as shown in Fig. 2.1, which is a good starting point when $t' \geq t$.

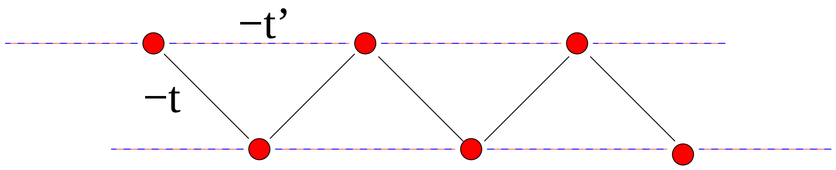

Figure 2.1: Depiction of the t-t' Hubbard model as a system of two coupled chains.

It, like the tight binding model, is exactly solvable via Fourier transformation in the case of $U = 0$. One then finds the dispersion relation to be

$$\epsilon(k) = -2t\cos(k) - 2t'\cos(2k). \tag{2.16}$$

This dispersion relation shows us that for sufficiently large fillings and $t' > 0.25$ or for sufficiently small fillings and $t' < -0.25$ the system has four Fermi points, yielding metallic behaviour. For $U \neq 0$, a metallic behaviour can only be found for sufficiently large t' and sufficiently small U. This is a significant difference to the Hubbard model (2.4), which is only metallic at $U = 0$. An insulating phase with a nonzero spin gap can be found in the same regime for larger U. For further information the reader is referred to Refs. [18] and [19] and references therein.

Chapter 3

Phenomena

3.1 1D Physics

In typical three-dimensional solids, the Coulomb interaction is of the same order of magnitude as the kinetic energy, and it is usually not possible to see one as dominant and the other one as negligible. Therefore, perturbation theory cannot be used. Fortunately, however, the effects of the Coulomb interaction in higher dimensions are, at least for small excitation energies, almost perfectly described by Landau's Fermi liquid theory [20]. In Fermi liquid theory, the excitations can be described as quasi-particles, which are essentially electrons dressed with density fluctuations in the form of particle-hole excitations. Since these quasi-particles are composed of particle-hole excitations, which are basically bosons, and one electron, they still behave like fermions. These quasi-particles can be considered to be free and have a direct correspondence to the free electron excitations of the non-interacting system. Essentially, they can be viewed as electrons with a renormalized mass; therefore, each excitation is directly associated with the creation of one or more of these electron like quasi-particles.

Unfortunately, these convenient properties do not hold true for one dimensional systems. This is mainly due to the fact that in one dimension the possibility for excitations stemming from a single particle does not exist. Hence all excitations have the form of collective motion, i.e., collective modes. This fact alone makes the existence of Landau quasi-particles impossible and therefore invalidates the concept of Fermi-liquid theory in one dimension.

Here the Tomonaga-Luttinger-liquid theory is used to explain the low-frequency behaviour. It is based on the Tomonaga-Luttinger model which is based on some very insightful approximations. A short outline of these approximations will be given here and the reader is referred to Ref. [21] for further information.

If we assume that the interactions are much smaller than the bandwidth of the model treated and if we are only interested in the low-energy physics of this model, it is a reasonable approximation to linearize the dispersion relation near the two Fermi points. This makes sense because interactions far below the Fermi edge are forbidden by Pauli blocking and interactions far above the Fermi edge are not possible because we are considering only low-energy processes. Due to this, it is reasonable to introduce left-moving and right-moving fermions leading to the Tomonaga-Luttinger Hamiltonian

$$H_{\mathrm{TL}} = \sum_{k;r=R,L} \frac{k_F}{m_e}(\epsilon_r k - k_F) c^\dagger_{r,k} c_{r,k} + H_{\mathrm{Int}}, \tag{3.1}$$

where $\epsilon_R = 1$ for right-moving particles and $\epsilon_L = -1$ for left-moving particles and H_{Int} is the part of the Hamiltonian containing the interactions. The interaction part can be written as [21]

$$H_{\mathrm{Int}} = \frac{1}{2\Omega} \sum_{k,k',q} V(q) c^\dagger_{k+q} c^\dagger_{k'-q} c_{k'} c_k, \tag{3.2}$$

where Ω is the Volume of the system and $c^\dagger_k / c_k$ creates/annihilates an electron with momentum k. One should note that the most important processes here are the ones close to the Fermi surface. This fact restricts the possible terms in the interaction to four different classes [22], i.e.,

$$H_{\mathrm{Int}} = H_1 + H_2 + H_3 + H_4 \tag{3.3}$$

with the terms:

1. Scattering of particles either in the vicinity of the left or the right Fermi point (amplitude g_4):

$$\begin{aligned} H_4 = \frac{1}{2L} \sum_{\sigma,\sigma',k_1,k_2,q} g_4^{\sigma,\sigma'} \Big(& r^\dagger_{k_1,\sigma} r^\dagger_{k_2,\sigma'} l_{k_2+q,\sigma'} l_{k_1-q,\sigma} \\ & + l^\dagger_{k_1,\sigma} l^\dagger_{k_2,\sigma'} r_{k_2+q,\sigma'} r_{k_1-q,\sigma} \Big) . \end{aligned} \tag{3.4}$$

2. Scattering of one particle in the vicinity of the left/right Fermi point and of the other particle in the vicinity of the other Fermi point (amplitude g_2):

$$H_2 = \frac{1}{L} \sum_{\sigma,\sigma',k_1,k_2,q} g_2^{\sigma,\sigma'} r^\dagger_{k_1,\sigma} l^\dagger_{k_2,\sigma'} r_{k_2+q,\sigma'} l_{k_1-q,\sigma}. \tag{3.5}$$

3. Backscattering of a particle in which a left-moving particle is scattered into a right-moving particle and vice versa (amplitude g_1):
$$H_1 = \frac{1}{L} \sum_{\sigma,\sigma',k_1,k_2,q} g_1^{\sigma,\sigma'} r^\dagger_{k_1,\sigma} l^\dagger_{k_2,\sigma'} r_{k_2+2k_F+q,\sigma'} l_{k_1-2k_F-q,\sigma}. \tag{3.6}$$

4. Umklapp process in which two right-moving particles are scattered to two left-moving particles and vice versa (amplitude g_3). This process is only possible at half band filling ($4k_f = 2\pi$):
$$H_3 = \frac{1}{2L} \sum_{\sigma,\sigma',k_1,k_2,q} g_3^{\sigma,\sigma'} \left(r^\dagger_{k_1,\sigma} r^\dagger_{k_2,\sigma'} l_{k_2-2k_F+q,\sigma'} l_{k_1+2k_F-q-2\pi,\sigma} + \text{h.c.} \right). \tag{3.7}$$

In all four equations above $r^\dagger_{k,\sigma}/r_{k,\sigma}$ creates/annihilates a particle in the vicinity of the right Fermi point and $l^\dagger_{k,\sigma}/l_{k,\sigma}$ creates/annihilates a particle in the vicinity of the left Fermi point. The naming of the different terms $g_1 - g_4$ has a historical origin, leading to the term *g-ology.* Solving this model for electrons with spin yields two different velocities, one for the charge degrees of freedom and one for the spin degrees of freedom. This clearly shows that the notion of electron-like quasi-particles like those found in Fermi liquids is not sensible in Luttinger liquids. Instead, there is a separation of the elementary excitations into charge degrees of freedom (holons) and spin degrees of freedom (spinons). This, together with the fact that the one-particle spectral function does not show typical Fermi-liquid pole structure, indicating the lack of electron-like quasi-particles is the most prominent feature of one-dimensional systems.

3.2 Phase Transitions

Phase transitions are transitions of a substance between two qualitatively different states. These transitions more often than not involve symmetry-breaking. In classical physics, phase transitions are driven by thermal fluctuations. The different types of transitions are classified by whether the transition involves latent heat (first order transition) or not (continuous transition). In addition, there is a special class of continuous phase transition which do not involve symmetry-breaking. Such transitions are usually referred to as infinite-order phase transitions. The most well-known example of an infinite order transition is the Kosterlitz Thouless transition in the two-dimensional classical XY-model [23].

There are clearly no thermal fluctuations in quantum mechanical systems at zero temperature ($T = 0$); instead, a quantum phase transition is driven by quantum fluctuations due to the Heisenberg uncertainty principle. For a Hamiltonian that depends on the parameter λ,

$$H = H(\lambda), \tag{3.8}$$

there are possibly some distinct critical values of λ at which phase transitions occur (λ_c). The phases on either site of such a phase transition are typically distinguishable through an order parameter which is nonzero inside one of the phases and zero outside. Some examples of such order parameters are given in Eqs. (2.9),(2.11), and (2.12). Since the classification of quantum phase transitions through latent heat is obviously not sensible, one typically uses a classification scheme that is closely related to the now deprecated Ehrenfest classification for classical phase transitions. The ground-state energy is viewed as the quantum mechanical equivalent to the free energy in classical phase transitions. Hence, phase transitions which have a discontinuity in the first derivative of the ground-state energy are regarded as first-order phase transitions. Those with a discontinuity in the second derivative of the ground-state energy are second-order transitions and those that are analytical in all derivatives of the ground-state energy are usually termed infinite-order or Kosterlitz Thouless transitions [23].

Unfortunately, the classification of phase transitions using the scheme outlined above is not always easily possible. Especially for numerically generated data, a small discontinuity is very hard to resolve in any derivative. Therefore it is useful to realize that other quantities can be used to determine the order of a phase transition. One of these quantities is, for example, the functional character of the size of the energy gap Δ_E with respect to the distance to the critical point λ_c at which the phase transition occurs. For infinite-order transitions, the energy gap Δ_E opens exponentially, i.e., as

$$\Delta_E \sim \frac{A}{e^{|\lambda-\lambda_c|\sigma}}, \tag{3.9}$$

where A and σ are model-dependent parameters. This equation only holds true for λ near λ_c. For second-order transitions the gap opens with a power-law dependence

$$\Delta_E \sim J|\lambda - \lambda_c|^{z\nu}, \tag{3.10}$$

where J corresponds to the energy scale of the underlying model and z and ν are critical exponents.

Even though it has not been rigorously proven, it can be strongly argued [24] that all second-order quantum phase transitions belong to universality

Zero-field specific heat	$C_H \sim \lvert t\rvert^{-\alpha}$
Zero-field magnetization	$M \sim (-t)^{\beta}$
Zero-field isothermal susceptibility	$\chi_T \sim \lvert t\rvert^{-\gamma}$
Critical isotherm ($t = 0$)	$H \sim \lvert M\rvert^{\delta}\mathrm{sign}(M)$
Correlation length	$\xi \sim \lvert t\rvert^{-\nu}$
Pair correlation function at T_c	$G(\vec{r}) \sim 1/r^{d-2+\eta}$

Table 3.1: Commonly used critical exponents for a magnetic system.

classes which are independent of the microscopic details of the underlying model. Instead, they depend only on the dimensionality of the system and on the symmetries of the model of interest. These universality classes posses characteristic critical exponents. One of the reasons why this assumption is sensible is that for certain models (e.g., the Ising model) a mapping exists from the d-dimensional quantum model to a $d+1$-dimensional classical model [24]. Hence, we can relate the quantities and the associated critical exponents for the quantities as well.

Some of the most commonly used quantities for a magnetic system are given in Table 3.1 [25]. Here t is the normalized distance to the critical temperature

$$t = \frac{T - T_c}{T_c}$$

which translates to the normalized distance to the critical parameter value in quantum systems.

These critical exponents are not completely independent but obey the inequalities [25]

$$\alpha + 2\beta + \gamma \geq 2 \tag{3.11}$$

$$\alpha + \beta(1 + \delta) \geq 2 \tag{3.12}$$

$$\gamma \leq (2 - \eta)\nu \tag{3.13}$$

$$d\nu \geq 2 - \alpha \tag{3.14}$$

$$\gamma \geq \beta(\delta - 1), \tag{3.15}$$

where d is the dimensionality of the classical system. For the two-dimensional Ising model with [25]

$$\alpha = 0 \qquad \beta = \frac{1}{8} \qquad \gamma = \frac{7}{4}$$

$$\delta = 15 \qquad \nu = 1 \qquad \eta = \frac{1}{4},$$

one can verify that the above listed inequalities actually hold as equalities.

The one critical exponent which has not yet been discussed is the dynamic critical exponent z, which appears, for example, in Eq. (3.10). It links the correlation length with the energy gap as

$$\Delta_E \sim \xi^{-z}. \tag{3.16}$$

These critical exponents are widely used to classify second-order phase transitions such as those shown in Ref. [15].

Chapter 4

Measured Quantities

4.1 Quantum Entropy

Quantum entropy is a fairly recent concept stemming mainly from quantum information theory. It is closely related to the classical concept of entropy in that there is a very close relation between information and structure and the gain in entropy for erasing such. There are various measures of quantum entropy, such as the concurrence [26], the negativity [27] or the Von Neumann entropy [28]. Although they these are all, in principle, equivalent, we will discuss and use solely the Von Neumann entropy in this thesis, mostly because it has the closest relation to the DMRG procedure, as will be explained more thoroughly in Sec. 6.

The Von Neumann entropy is defined directly through the eigenvalues of the density matrix. If we consider an arbitrary ensemble of quantum states expressed through a density matrix

$$\rho = \sum_j p_j |\psi_j\rangle\langle\psi_j|, \tag{4.1}$$

where the coefficients p_j are the weights of $|\psi_j\rangle$ in the ensemble and hence fulfill the relation

$$\sum_j p_j = 1,$$

then the corresponding Von Neumann entropy is defined as

$$S = -\sum_j p_j \ln(p_j). \tag{4.2}$$

From this definition, it is directly clear that, for an ensemble which only contains one state, the corresponding Von Neumann entropy is $S = 0$ whereas for an ensemble of N equally weighted states, the corresponding Von Neumann entropy is

$$S = -\sum_{j=1}^{N} \frac{1}{N} \ln\left(\frac{1}{N}\right) = \ln(N).$$

While there are different uses for entropy measurements, one of the main uses is the measurement of entanglement in a pure quantum state. This is done by dividing the quantum state into two parts and then measuring the entropy in one of the two subsystems. The more the two blocks are entangled, the larger a value the entropy measurement will yield.

The Schmidt decomposition is the theorem which assures us that if we divide a system into two parts we do not have to worry about getting different results for the entropy in the different parts of system. It states that every state $|\psi\rangle_{AB}$ which is defined on $\mathcal{H}_A \otimes \mathcal{H}_B$ can be written as

$$|\psi\rangle_{AB} = \sum_j \sqrt{p_j}|j\rangle_A|j'\rangle_B, \tag{4.3}$$

where p_j are the weights of the states $|j\rangle$ in subsystem A as well as of the states $|j'\rangle$ in subsystem B. Therefore, we know for certain that

$$S_A = S_B$$

regardless of the partitioning scheme we chose. This property of the quantum entropy is extensively used in Chapter 6.

Another useful property of quantum entropy is that the value of the quantum entropy depends on what phase a system is in. Therefore it has become apparent in recent work [16, 29] that quantum entropy measurements can be used to detect quantum phase transitions (QPTs) in various one-dimensional models with high precision and reliability. Unfortunately, one always has to have access to the reduced density matrix $\rho_{A/B}$ of at least one of the subsystems.

Given a general description of a quantum state on two systems $\mathcal{H}_A \otimes \mathcal{H}_B$ it can always be expressed as

$$|\psi\rangle_{AB} = \sum_{i,j} C_{ij}\,|i\rangle_A \otimes |j\rangle_B, \tag{4.4}$$

where C_{ij} is a matrix with complex entries and $|i\rangle$ and $|j\rangle$ represent orthonormal bases on subsystems A and B, respectively. The reduced density matrix of subsystem A is then given by

$$\begin{aligned}\rho_A &= \mathrm{Tr}_B\left(|\psi\rangle\langle\psi|\right)\\ &= \sum_j \langle j|\psi\rangle\langle\psi|j\rangle\\ &= \sum_{i,i',j} C_{ij}C^*_{i'j}|i\rangle\langle i'|.\end{aligned} \tag{4.5}$$

If we now imagine one of the subsystems to be very large and the other one to be very small, then we either have to sum over a lot of states $|j\rangle$ in the trace or we end up with a very large reduced density matrix, neither of which is desirable. Therefore, it is useful to realize that is is also possible to express the density matrix of a subsystem in terms of projectors from all possible states in that subsystem to all possible states in that subsystem,

$$\langle i|\rho_A|i'\rangle \equiv \langle\psi|P_{i',i}|\psi\rangle = \langle\psi|\left(\sum_j |i\rangle\otimes|j\rangle\langle j|\otimes\langle i'|\right)|\psi\rangle. \tag{4.6}$$

For simple subsystems and an appropriate choice of the basis $|i\rangle$, the operator $P_{i',i}$ can be expressed in terms of relatively simple operators so that its matrix elements can be directly calculated using the corresponding observables [30].

In the following, we will describe the three most useful types of quantum entropy for detecting QPTs in numerical calculation marked by different choices of subsystems.

4.1.1 One-site entropy

In order to form the one-site entropy, which we will denote $S_l(1)$, the subsystem A is simply taken to be a particular single site l. Since the Hamiltonians we usually deal with (e.g., the extended Hubbard Hamiltonian (2.8)) contain no spin-flip processes, the reduced density matrix can be obtained directly in diagonal form if we take the spin occupation basis $(|0\rangle, |\uparrow\rangle, |\downarrow\rangle, |\uparrow\downarrow\rangle)$ as the basis states $|i\rangle$ in Eq. (4.6). In this basis, we can directly obtain the eigenvalues from the expectation values of the four operators [30]

$$\begin{aligned}\langle\uparrow\downarrow|\rho_l|\uparrow\downarrow\rangle &= \langle n_{l\uparrow}n_{l\downarrow}\rangle,\\ \langle\downarrow|\rho_l|\downarrow\rangle &= \langle(1-n_{l\uparrow})n_{l\downarrow}\rangle,\\ \langle\uparrow|\rho_l|\uparrow\rangle &= \langle n_{l\uparrow}(1-n_{l\downarrow})\rangle,\\ \text{and } \langle 0|\rho_l|0\rangle &= \langle(1-n_{l\uparrow})(1-n_{l\downarrow})\rangle\,.\end{aligned}$$

The one-site entropy is relatively easy to calculate because it requires only four local measurements on site l. While the one-site entropy is useful for characterizing first-order QPTs in some cases, it is typically not well-suited for determining higher-order QPTs because anomalies, e.g., kinks or jumps in the entropy profile, are often only discernible for large system sizes and are sometimes not present at all [29, 31]. In particular, changes in inter-site bond strength have no influence on the one-site entropy. Since the one-site entropy necessarily only depends on quantities that are localized on that one site (in fact, only on the average occupancy and on the average double occupancy), it cannot contain spatial information that is nonlocal.

4.1.2 Two-site entropy

It is therefore often useful to examine the Von Neumann entropy associated with a larger subsystem. One convenient choice of subsystem A is that of two sites p and q, i.e., the two-site entropy $S_{p,q}$. In Chapter 11 we will be particularly interested in characterizing a BOW phase, which, for open boundary conditions, will have a broken bond-centered spatial symmetry. Thus, in this case, we are principally interested in the behavior of the two-site entropy for different bonds, i.e., we take p and q to be pairs of nearest-neighbor sites. Therefore, the two-site entropy will typically be denoted as $S_p(2)$, meaning $S_{p,p+1}$.

The two-site entropy can be obtained by calculating and diagonalizing the reduced density matrix for the two sites. As for the one-site density matrix, its matrix elements in the occupation number basis can be expressed straightforwardly in terms of expectation values localized on the two sites by considering the projector of Eq. (4.6). However, the result is necessarily somewhat more complicated than for the one-site density matrix. Since spin and particle number are conserved quantum numbers in Hamiltonian (2.8), the resulting reduced density matrix is block diagonal (rather than diagonal as for the one-site case) and has 26 independent matrix elements; for details, see Ref. [30]. Hence, 26 independent measurements, followed by the appropriate matrix diagonalization and the summation of Eq. (4.2), must be performed for every two-site entropy calculated.

Note that calculating all $N(N-1)$ two-site entropies on an N site system would be prohibitively expensive for large system sizes. While considering only nearest-neighbor bonds reduces this to $N-1$, it is usually sufficient to calculate the entropy of the two pairs of innermost sites, $S_{N/2-1}(2)$ and $S_{N/2}(2)$, i.e., two bonds chosen to be in the middle of the system to minimize boundary effects.

4.1.3 Block entropy

The block entropy is also based on splitting the system into two subsystems A and B. However, subsystem A is now taken to contain the l contiguous sites 1 to l and subsystem B to contain the remainder, sites $l+1$ to N. (Other choices of sets of contiguous sites are also possible.) We then calculate the Von Neumann entropy $S(l)$ using Eq. (4.2) for $l \in 1, ..., N$. Note that calculating the projector $P_{i',i}$ of Eq. (4.6) would be prohibitively complicated and expensive. Here we instead calculate the density matrix directly from the wave function using Eq. (4.5). Fortunately, the wave function for all divisions of the system l is readily available in the appropriate finite-system step of the DMRG algorithm, and, in fact, the corresponding Von Neumann entropy is intimately related to the approximation made in the DMRG [32]. This will also be explained in detail in Sec. 6.

Unlike the two-site entropy, which has an finite upper bound ($\ln 16$ for Hubbard-like models), the block entropy generally grows as $\mathcal{O}(\ln N)$ for critical one-dimensional systems [33] (but scales to a finite value for non-critical systems). Although such a potential divergence would at first glance seem favorable for studying QPTs, the situation is actually more complicated: boundary effects from open boundary conditions should have a stronger influence on the block entropy than on a more locally defined quantity such as the one-site or two-site entropy. It is therefore not clear which of these entropies can more accurately detect QPTs, but it seems sensible to expect that fast-growing peaks are better detected by the block entropy, while non-diverging anomalies, such as discontinuities in derivatives, can be more precisely determined by the two-site entropy.

4.2 Spectral Function & Density of States

The single-particle spectral function provides us with direct information about the quasi-particle excitations of a system. It is therefore not only interesting from a theoretical point of view, but it is also interesting to compare to spectral functions measured directly in experiments [34].

The spectral function $A(k, \omega)$ and the density of states $\rho(\omega)$ can both be calculated from the retarded Green's function

$$G^{\text{ret}}_{A,B}(t) = -i\Theta(t) \left\langle [A(t), B(0)]_{\pm} \right\rangle , \tag{4.7}$$

where the commutator or anti-commutator is chosen depending on whether A and B are bosonic or fermionic operators, respectively.

Using this notation, the single particle spectral function for a fermionic model is given as

$$\begin{aligned} A(k,\omega) &= -\frac{1}{\pi}\Im\left(\int_{-\infty}^{\infty} e^{i\omega t}\, G^{\text{ret}}_{k,k}(t)\ \mathrm{d}t\right) && \text{(4.8a)} \\ &= \frac{1}{\pi}\Re\left(\int_{0}^{\infty} e^{i\omega t}\left\langle\psi\right|\left[c_k(t), c_k^{\dagger}(0)\right]_{+}\left|\psi\right\rangle\right), && \text{(4.8b)} \end{aligned}$$

where $c_k^{\dagger}(0)$ creates a fermion with momentum k at time 0 and $c_k(t)$ annihilates a fermion with momentum k at time t.

The density of states gives us information about how many states are accessible in an infinitesimal interval around a certain energy ω. It is therefore given as the integral over k of the spectral function,

$$\rho(\omega) = \int_0^{\pi} A(k,\omega)\ \mathrm{d}k. \tag{4.9}$$

Having an accurate description of the density of states, one can easily read off important information such as the band gap and the bandwidth of bands that are present.

4.2.1 Finite Systems

One problem that must be dealt with is that one calculates the retarded Green's function on a finite system but is actually interested in the spectral function of a macroscopic (infinite) system. In a finite system, the angle resolved spectral function is calculated from the dynamical correlation function as

$$\begin{aligned} A(k,\omega) &= \frac{1}{\pi}\Re\left(\int_{0}^{\infty} e^{i\omega t}\left\langle\psi\right|\left[c_k(t), c_k^{\dagger}(0)\right]\left|\psi\right\rangle\right) \\ &= \frac{1}{\pi}\Re\left(\int_{0}^{\infty} e^{i\omega t}\frac{2}{N+1}\sum_{j,l=1}^{N}\sin(kj)\sin(kl)\left\langle\psi\right|\left[c_j(t), c_l^{\dagger}(0)\right]\left|\psi\right\rangle\right), \end{aligned} \tag{4.10}$$

where the transformation of the creation and annihilation operators ($c^{\dagger}$ and c) is taken from the derivation in appendix A, and N is the number of sites in the system.

It is clear from Eq. (4.10) that, for certain values of k, the sites in the middle of the system $l \approx N/2$ contribute very little to the spectral functions. However, we can only use sites near the middle of the system for the position of the creation operator l because boundary effects would already be visible in the Green's function at very small times if we were to choose l to be close to the system boundaries. This leaves us somewhat in a pickle because we cannot calculate the dynamical correlation function for all j and l due to the above-mentioned boundary problems as well as due to computational constraints. The solution is to assume stationarity in the correlation function, i.e.,

$$\left\langle \psi \middle| c_j(t) c_l^\dagger(0) \middle| \psi \right\rangle = \left\langle \psi \middle| c_i(t) c_{i+r}^\dagger(0) \middle| \psi \right\rangle , \tag{4.11}$$

where $r = l - j$ and where the latter expression only depends on r and not on i. With this assumption, we can reformulate the expression for the spectral function in a way that eliminates this problem. For simplicity, we show this for only a part of equation (4.10):

$$\begin{aligned}
&\sum_{j,l=1}^{N} \sin(kl)\sin(kj) \left\langle c_l(t) c_j^\dagger(0) \right\rangle \\
&\overset{l=j+r}{=} \sum_{j=0}^{N} \sum_{r=1-j}^{N-j} \sin(kj)\sin(k(j+r)) \left\langle c_{j+r}(t) c_j^\dagger(0) \right\rangle \\
&= \sum_{j=0}^{N} \sum_{r=1-j}^{N-j} \sin(kj)\left(\sin(kj)\cos(kr) + \cos(kj)\sin(kr)\right) \left\langle c_{j+r}(t) c_j^\dagger(0) \right\rangle \\
&\approx \sum_{r=-\frac{N}{2}+1}^{\frac{N}{2}} \cos(kr) \left\langle c_{\frac{N}{2}+r}(t) c_{\frac{N}{2}}^\dagger(0) \right\rangle \underbrace{\sum_{j=0}^{N} \sin^2(kj)}_{\frac{L+1}{2}} \\
&+ \sum_{r=-\frac{N}{2}+1}^{\frac{N}{2}} \sin(kr) \left\langle c_{\frac{N}{2}+r}(t) c_{\frac{N}{2}}^\dagger(0) \right\rangle \underbrace{\sum_{j=0}^{N} \sin(kj)\cos(kj)}_{=0} \\
&= \sum_{r=-\frac{N}{2}+1}^{\frac{N}{2}} \cos(kr) \left\langle c_{\frac{N}{2}+r}(t) c_{\frac{N}{2}}^\dagger(0) \right\rangle \frac{L+1}{2} .
\end{aligned} \tag{4.12}$$

Here $\langle \cdot \rangle$ is used as an abbreviation for $\langle \psi | \cdot | \psi \rangle$.
Using this approximation, the spectral function can be written as

$$A(k,\omega) = -\frac{1}{\pi} \Re \left(\int_0^\infty e^{i\omega t} \sum_{r=-\frac{N}{2}+1}^{\frac{N}{2}} \cos(kr) \left\langle \psi \right| \left[c_{\frac{N}{2}+r}(t), c_{\frac{N}{2}}^\dagger(0) \right] \left| \psi \right\rangle \right) . \tag{4.13}$$

This allows us to calculate the dynamical correlation function only for a few sites in the middle of the system and then average over these sites, yielding results for a system in the thermodynamic limit. The size of the system only restricts the resolution in frequency. This will be explained in more detail in Sec. 9.3.2.

Part II

Methods and Implementation

In this part, we will introduce some of the numerical approaches used in condensed matter physics, especially those closely related to the DMRG. In particular, we will explain the analytical and numerical methods containing the basic ideas used within the DMRG framework as well as how the DMRG developed out of them. We will then give a detailed explanation of the DMRG as used in ground-state calculations and its two main algorithms. While discussing these two algorithms, we will also point out their shortcomings and give some insight as to why the standard DMRG algorithms have difficulties dealing with certain systems, e.g., two-dimensional systems or systems with periodic boundary conditions. We will then explain some recent developments that have yielded algorithms that are equivalent to the DMRG and that possess the potential to eliminate these problems. In discussing the advantages of these newly developed algorithms over the old ones, we will also enable the reader to gain a better and more intuitive understanding of the concepts behind the DMRG and its associated algorithms.

After elucidating the workings of the standard DMRG, we will explain how to carry out the time evolution of a quantum state within the DMRG framework. We will then explain how to use the capability of time evolving a quantum state to obtain angle-resolved spectral data as well as densities of states for most one-dimensional models that can be represented in second-quantized form. Finally, we will address the problem of obtaining data for a system in the thermodynamic limit by carrying out measurements on small finite systems.

Chapter 5

Evolution of the DMRG

As already discussed in Chapter 2, in condensed matter physics, one usually treats a system consisting of particles on a lattice, with a Hamiltonian that allows for hopping between the different sites as well as an interaction between the different particles. The Hilbert space $\mathcal{H}$ corresponding to such a system is the tensor product of the degrees of freedom $|s\rangle$ on each site of the lattice. Therefore, in an N-site system, the corresponding Hilbert space would have the form

$$\mathcal{H} = \mathcal{H}_1 \otimes \mathcal{H}_2 \otimes \cdots \otimes \mathcal{H}_N, \tag{5.1}$$

where $\mathcal{H}_i$ denotes the local Hilbert space on site i. Evidently, the dimension of the Hilbert space grows exponentially with the number of sites in the system. If we assume that every site i has the same number of degrees of freedom, then the entire Hilbert space has dimension

$$\dim\left(\mathcal{H}\right) = \dim\left(\mathcal{H}_i\right)^N . \tag{5.2}$$

5.1 Exact Diagonalization

Even though the dimension of the Hilbert space grows exponentially with the number of sites in the system, it is still possible to find particular states, e.g., the ground state, for small system sizes exactly, using certain optimized algorithms. This task can be accomplished by iterative exact diagonalization algorithms, two of which will be described in the following.

5.1.1 Lanczos Diagonalization

The Lanczos algorithm [35] is, first and foremost, an orthogonalization procedure on a vector-space basis. It can be thought of as containing two main steps. The first step is to start with a randomly chosen start vector $|\psi_0\rangle$ and then build up the corresponding Krylov space,

$$\left\{|\psi_0\rangle,\ H|\psi_0\rangle,\ H^2|\psi_0\rangle,\ H^3|\psi_0\rangle,\dots\right\}, \tag{5.3}$$

where H is the matrix we want to diagonalize. The second step is to orthogonalize the Krylov space with a regular Gram-Schmidt orthogonalization algorithm.

In the above steps, there is no gain in efficiency in comparison to a full diagonalization of the matrix. Fortunately the two steps outlined above can be combined into one, iterative, step, in which one starts with the random vector $|\psi_0\rangle$ and then generates a sequence of vectors using the recursion relation

$$\begin{aligned} |\psi_{n+1}\rangle &= H|\psi_n\rangle - a_n|\psi_n\rangle - b_n^2|\psi_{n-1}\rangle \\ \text{where } a_n &= \frac{\langle\psi_n|H|\psi_n\rangle}{\langle\psi_n|\psi_n\rangle} \\ \text{and } b_n^2 &= \frac{\langle\psi_n|\psi_n\rangle}{\langle\psi_{n-1}|\psi_{n-1}\rangle}, \end{aligned} \tag{5.4}$$

with $|\psi_{-1}\rangle = 0$ and $b_0 = 0$. Using this relation, in which the Lanczos vectors are not normalized, one can terminate the recursion when the new vector $|\psi_n\rangle$ is smaller then a predetermined stopping criterion for the norm $\sqrt{\langle\psi_n|\psi_n\rangle} < \epsilon$.

It can be shown [35] that our matrix H takes on a tridiagonal form,

$$\tilde{H}_n = \begin{pmatrix} a_0 & b_1 & & & 0 \\ b_1 & a_1 & b_2 & & \\ & b_2 & a_2 & \ddots & \\ & & \ddots & \ddots & b_n \\ 0 & & & b_n & a_n \end{pmatrix}, \tag{5.5}$$

in this new basis of normalized Lanczos vectors. The matrix $\tilde{H}$ can be diagonalized much faster because it is smaller (typically 100 × 100 at most) and because of its tridiagonal form. One should keep in mind that $\tilde{H}$ is not equal to H in the new basis but is instead only an approximation to H with an error of roughly ϵ.

Unfortunately, although the Lanczos basis is orthogonal, in principle, numerical roundoff errors cause the basis vectors to lose orthogonality fairly quickly in finite precision arithmetic, and spurious eigenvalues appear in the resulting tridiagonal matrix. To counter this effect, one usually calculates only the first 100 Lanczos vectors and then restarts the method with the current approximation for the target vector as the new starting vector.

5.1.2 Davidson Diagonalization

Davidson diagonalization [36, 37] is similar to Lanczos diagonalization in the sense that one starts with a random starting vector and then applies an iterative procedure to build up a subspace of the vector space in which the matrix H, which is to be diagonalized, is well approximated. The difference between Davidson diagonalization and Lanczos diagonalization lies in the iterative procedure that is used to build up the subspace. In the Lanczos procedure, the component of the approximated residual vector

$$|r_k\rangle = H|\tilde{\psi}_k\rangle - \tilde{\lambda}_k|\tilde{\psi}_k\rangle, \tag{5.6}$$

that is orthogonal to the already built-up part of the vector subspace is taken, where $|\tilde{\psi}_k\rangle$ is the approximation to the target vector $|\psi_k\rangle$ in the subspace, and $\tilde{\lambda}_k$ is the corresponding eigenvalue in that subspace. Davidson proposed the following alternate iterative scheme to build up the subspace. The correction vector to $|\tilde{\psi}_k\rangle$ is given by

$$|z\rangle = |\psi\rangle - |\tilde{\psi}_k\rangle. \tag{5.7}$$

Therefore,

$$\left(H - \lambda_k\right)|z\rangle = -\left(H - \lambda_k\right)|\tilde{\psi}_k\rangle. \tag{5.8}$$

Thus, the correct correction vector $|z\rangle$ can be determined exactly using

$$|z\rangle = -\left(H - \lambda_k\right)^{-1}|r_k\rangle. \tag{5.9}$$

Since finding the inverse of $(H - \lambda_k)$ involves the same amount of numerical effort as fully diagonalizing H, this does not yet lead to a gain in efficiency. Davidson's idea, was to approximate $|z\rangle$ as

$$|\tilde{z}\rangle = -\left(D - \tilde{\lambda}_k\right)^{-1}|r_k\rangle, \tag{5.10}$$

where D is a diagonal matrix containing diagonal elements of H. Therefore, the Davidson diagonalization works best if H is diagonally dominant and, even though one can find pathological cases where the Lanczos algorithm outperforms the Davidson algorithm, the Davidson algorithm has proven to converge faster and be more stable than the Lanczos algorithm in almost all cases in condensed matter physics.

In the following, we will briefly outline the steps of an iteration of the Davidson procedure [36].

1. To find the kth eigenvalue and eigenvector, start with l randomly chosen orthogonal vectors $|\psi_1\rangle, \ldots, |\psi_l\rangle$, where $l \geq k$.

2. Form and store the vectors $H|\psi_1\rangle, \ldots, H|\psi_l\rangle$ and build the matrix $\tilde{H}_{ij} = \langle\psi_i|H|\psi_j\rangle$.

3. Diagonalize $\tilde{H}$ using a standard dense matrix diagonalization method and select the kth eigenvalue $\lambda_k^{(l)}$ and the corresponding eigenvector $|\alpha_k^{(l)}\rangle$.

4. Form the residual vector

$$|q_l\rangle = \sum_{i=1}^{l} \left(|\alpha_k^{(l)}\rangle_i \, H|\psi_i\rangle - |\alpha_k^{(l)}\rangle_i \lambda_k^{(l)} |\psi_i\rangle \right).$$

   Here $|\alpha_k^{(l)}\rangle_i$ denotes the ith component of the vector $|\alpha_k^{(l)}\rangle$.

5. Calculate the norm of $|q_l\rangle$ and compare it to a preset maximum error criterion ϵ. If $\sqrt{\langle q_l|q_l\rangle} < \epsilon$, accept the last eigenvalue $\lambda_k^{(l)}$ and eigenvector $|\alpha_k^{(l)}\rangle$; otherwise, continue.

6. Form the correction vector

$$|c_l\rangle = \left(\lambda_k^{(l)} - D\right)^{-1} |q_l\rangle,$$

   where D contains the diagonal elements of H. Then form $|\psi_{l+1}\rangle$ by orthogonalizing $|c_l\rangle$ against all previous vectors $|\psi_i\rangle$, $i = 1, \ldots, l$ and then normalizing it.

7. Start again with step 2, but taking $l \to l + 1$.

In practice one usually performs a small number of Davidson steps (typically less than 20) and then restarts the procedure with

$$|\tilde{\psi}_i\rangle = \sum_{j=1}^{l} |\alpha_i\rangle_j |\psi_j\rangle.$$

Restarting the algorithm after a few steps helps to keep the memory used to a minimum, but can slightly increase computation time.

5.2 The Renormalization Group

The name “Renormalization Group” has its historical roots in the high energy physics of the 1960s. It stems from the fact that the Renormalization-Group idea was originally developed to describe the high energy behaviour of renormalized electrodynamics [38]. Unfortunately, the implications stemming from that name are very misleading, because the Renormalization Group has neither the underlying properties of a mathematical group nor does it use renormalization in the quantum field theoretic sense. In fact, ever since K. Wilson realized the potential of the Renormalization Group for describing the scaling behaviour of critical phenomena, it has been mostly used in that field of physics.

The general idea of the Renormalization Group is still the same, though. It is the scaling in a particular set of variables to obtain the degrees of freedom that are important for the description of the physics of the model at hand. This is most easily seen in the real-space renormalization of a lattice spin system, which we will use to outline this idea here.

Let us consider a two-dimensional square lattice. We assume that a spin is present on each lattice site and that nearest-neighbour spins interact with coupling constant J, e.g., as in the Ising model. Let us further assume that the physical behaviour that we are interested in, e.g., magnetic order, is described by a function $H(J,T)$, where T is the temperature and J the coupling constant.

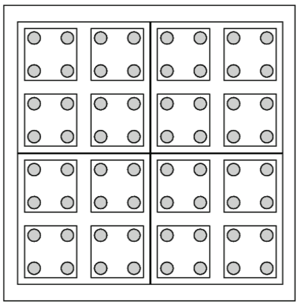

Figure 5.1: Block-spin transformation on a two-dimensional square lattice.

As depicted in Fig. 5.1, we divide the system into 2x2 blocks and then describe the system in terms of these new block variables, which are effective spins again. Let us now assume that the behaviour of this new system can again be described by a function of the same form as $H(T,J)$, but with renormalized variables T' and J'. We have thereby reduced the number of degrees of freedom in the system, but (hopefully) have still retained the important physics. This is called a scaling transformation.

For the Ising model, which is described by the Hamiltonian

$$H_{\text{Ising}} = \sum_{(i,j)}^{N} S_i^z S_j^z, \tag{5.11}$$

where the sum over i and j runs over nearest neighbours and S_i^z measures the spin in z-direction on site i, there are three fixed points for which the physics of the system does not change under such a scaling transformation.

1. $T \to 0$ and $J \to \infty$ $\Rightarrow$ complete magnetic order (ferromagnetism).
2. $T \to \infty$ and $J \to 0$ $\Rightarrow$ completely random order (paramagnetism).
3. Somewhere in between, at $T = T_c$ and $J = J_c$, there is a critical point at which the phase transition between the two above-mentioned phases occurs and at which the system is also invariant under the scaling transformation.

5.3 The Numerical Renormalization Group

Wilson originally invented the Numerical Renormalization Group (NRG) to treat impurity problems, specifically, the Kondo problem and the single-impurity Anderson model. We are only going to outline the basic algorithm of the NRG here and refer the reader to Refs. [39, 40] for further information.

The basic idea of the NRG is quickly stated. It is to represent a target state, that we want to calculate, not in the full basis of the Hilbert space but instead to only keep the ground state and a fixed number of low lying excited states and use those as a basis to represent it. Now, one could obviously argue that if we already knew the ground state and low lying excitations, we would have already solved the system, so what we actually use are the ground state and low lying excitations of an approximation to the system.

The method works as follows:

1. Begin with a system that is small enough to be diagonalized exactly.
2. Diagonalize the Hamiltonian H_L of the system of size L and find the ground state and the $m-1$ lowest-lying excited states. For this purpose, exact diagonalization routines are used.
3. Transform all operators of interest to the basis of the m lowest-energy eigenstates:
$$\tilde{A}_L = O_L^\dagger A_L O_L.$$

Here O_L contains in its columns the eigenvectors. One should note that the Hamiltonian takes a diagonal form after this transformation, but this is not necessarily the case for other operators.

4. Add a new site to the system and form new operators A_{L+1} on the new product basis created by this.
5. Start over at step 2 and replace H_L with H_{L+1}

In terms of the renormalization group framework, the rescaling is done here by adding additional sites to the system, whereas one identifies a fixed point when a set number of the lowest energies become independent of the length L of the system. Unfortunately, such behaviour is only to be expected from impurity problems but is, in general, not seen in more complicated tight-binding-like Hamiltonians. Even more problematic is the fact that the choice of the m eigenstates with the lowest energy of a system with size L are not necessarily a good basis for the ground state of a system with size $L+1$. This is even true for one of the simplest model in condensed matter physics, the tight binding model (2.2). As an example we can consider one particle on such a tight binding chain [41]. It can be seen directly that, if expressed in the real-space basis, the Hamiltonian of an L site system would read

$$H_L = \begin{pmatrix} 0 & -t & & & 0 \\ -t & 0 & -t & & \\ & -t & 0 & \ddots & \\ & & \ddots & \ddots & -t \\ 0 & & & -t & 0 \end{pmatrix}, \tag{5.12}$$

where t is the hopping element between the different sites. Furthermore, it can be easily verified that the wave functions for such a system take the form

$$\psi_L^n(l) = N \sin\left(\frac{n\pi l}{L+1}\right), \tag{5.13}$$

where N is a normalization constant, L is the size of the system, and n corresponds to the nth energy level.

Now if we construct a Hamiltonian for a system of twice the size it will simply be

$$H_{2L} = \begin{pmatrix} H_L & T \\ T^t & H_L \end{pmatrix}, \tag{5.14}$$

where

$$T = \begin{pmatrix} \vdots & & 0 \\ 0 & 0 & \\ -t & 0 & \dots \end{pmatrix}.$$

One could argue here that doubling the size of the system is unreasonable since only one site is typically added in a NRG step, but, because of the nature of the problem, adding one site in a interacting system amounts to the same increase in the number of degrees of freedom as doubling the system size in this problem. For this problem it is clear that what is shown in Fig. 5.2, namely that the lowest eigenstates for a system of size L are not a good basis for a system of size $2L$, since no small number of eigenstates of the system of size L can be used to express the ground-state of the system of size $2L$. This is also clearly visible from Table 5.1 which compares results from exact diagonalization with results from NRG [3].

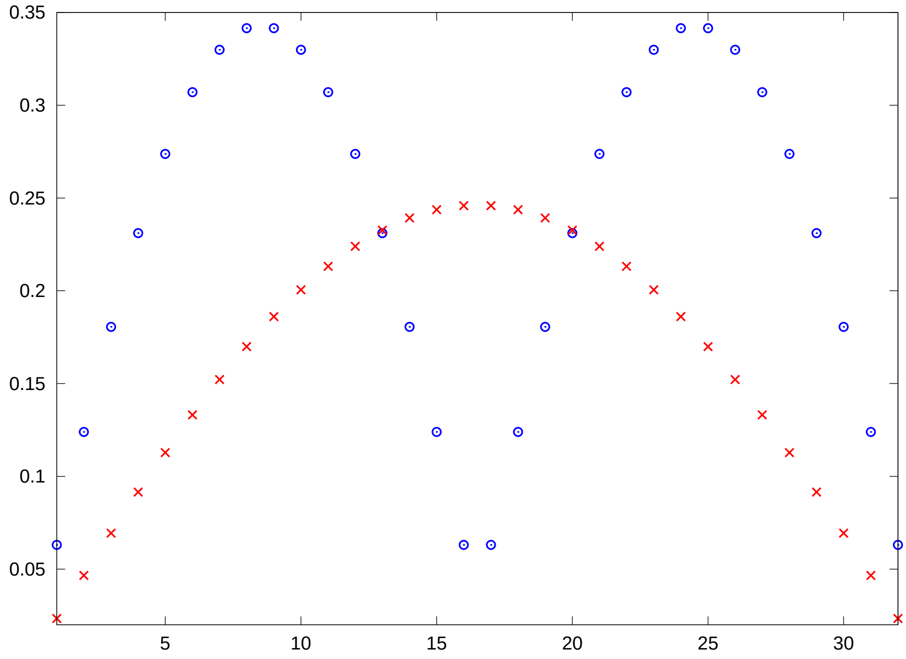

Figure 5.2: The ground-state wave function for a particle on a tight binding chain for two 16-site blocks and one 32-sites block.

	Exact	NRG
E_0	2.3508×10^{-6}	1.9207×10^{-2}
E_1	9.4032×10^{-6}	1.9209×10^{-2}
E_2	2.1157×10^{-5}	1.9214×10^{-2}
E_3	3.7613×10^{-5}	1.9217×10^{-2}

Table 5.1: Lowest energies after 10 block size increases for the single particle on a tight binding chain keeping the 8 lowest states as a basis [3].

Chapter 6

DMRG

The problems of the NRG we have discussed in Sec. 5.3 show us that forming a new reduced basis from the energetically lowest states for a system of size L is, in general, not a good choice if we want to represent a low energy state for a system of a different size. So the difficult question remains: Which degrees of freedom are most important to keep in order to find a good approximation for a given target state?

The answer that the DMRG gives us to this question, is that the important states we should retain are those states that *carry* most of the entanglement. This raises the question: What exactly is meant by entanglement quantitatively and how do we identify those states?

The answer to this question is given by the Schmidt decomposition, which has already been described in Sec. 4.1. The Schmidt decomposition tells us that if we consider a pure state $|\psi\rangle$ on an arbitrary system, and we divide this system into two parts, then the reduced density matrices of these two parts will have identical non-zero eigenvalues. These eigenvalues are the weights of the corresponding eigenvectors in that subsystem and can therefore be seen as a measure of the importance of these eigenvectors in describing the state of the entire system. Therefore, those eigenvectors which have a high eigenvalue in the reduced density matrix are the ones that we referred to earlier as *carrying* the most entanglement. Another way of saying the same thing in a more mathematical way is that the eigenstates which correspond to high eigenvalues are those that are most important for approximating the pure state $|\psi\rangle$ of the entire system. This can be seen by expressing a pure state on a bipartite system as

$$|\psi\rangle_{AB} = \sum_j \sqrt{p_j}|j\rangle_A|j'\rangle_B. \tag{6.1}$$

The best possible approximation $|\tilde{\psi}\rangle$ for $|\psi\rangle$, in a least square sense, with a fixed number of states m, is formed by keeping the eigenstates with the largest eigenvalues p_j. The error made in this approximation is

$$\begin{aligned}
\chi^2 &= \| |\psi\rangle - |\tilde{\psi}\rangle \|^2 && (6.2)\\
&= \left\| \sum_{j=1}^{N} \sqrt{p_j} |j\rangle_A |j'\rangle_B - \sum_{j=1}^{m} \sqrt{p_j} |j\rangle_A |j'\rangle_B \right\|^2 && (6.3)\\
&= \left\| \sum_{j=m+1}^{N} \sqrt{p_j} |j\rangle_A |j'\rangle_B \right\|^2 , && (6.4)
\end{aligned}$$

where $m \leq N = \min(\dim(A), \dim(B))$.

The states $|j\rangle$ and $|j'\rangle$ both form an orthonormal basis on their respective subsystems. All p_j's have to be positive and real because of the fact that the density matrix is hermitian and because of their interpretation as weights. Thus, we directly find that

$$\chi^2 = \| |\psi\rangle - |\tilde{\psi}\rangle \|^2 = \sum_{j=m+1}^{N} p_j. \tag{6.5}$$

This proves that the best possible approximation to $|\psi\rangle$ is formed by keeping the eigenstates corresponding to the m largest eigenvalues. It is also obvious from Eq. (6.5) that the error made in the approximation can be measured by the discarded weight χ^2.

6.1 Truncation Schemes

There are different schemes that one can employ for choosing the number of states m to be kept. Typically, there are three different methods used, two of which are very straightforward.

1. Keeping a **constant number of states** is the simplest possible scheme. It was extensively used historically. However, this is the worst truncation scheme from an efficiency point of view, since the calculation time is highly dependent on the number of states m kept. In fact, as we will point out later, for large m the computation time $T \propto m^3$. On the other hand, this truncation scheme is the simplest to implement.

2. Keeping the **discarded weight** fixed is also fairly straightforward and can greatly increase efficiency, especially when the target state can be represented accurately by a fairly small number of eigenstates. This

is sometimes not clear, *a priori*. Using this approach, one needs to be aware of a problem that can occur when, during the buildup of the system, too few states are used. In this case, there is the possibility that the algorithm is not able to converge to the true ground-state ultimately, i.e., that is gets stuck in a local energy minimum instead. Therefore, when using this method, one has to make an appropriate choice for the minimum number of states to be kept. This choice can vary depending on the model.

3. Keeping the **Von Neumann entropy** constant [42] is an approach which is not as straightforward, but which is, in fact, very similar to keeping the discarded weight constant, because the Von Neumann entropy (4.2) is very closely related to the weights of the reduced density matrix. This scheme is used mainly if one wants to make quantum entropy measurements, because in that case it is important to assure that changes in the quantum entropy are due to parameter dependent changes in the system and not due to the truncation scheme used.

It should also be mentioned that, regardless of the truncation scheme used, the entire approximation relies on the fact that the weights p_j in the reduced density matrix fall off quickly enough. Otherwise, we would either have a comparatively poor approximation to the true wave function or would need to keep an exceedingly large number of states, making the computation unfeasible for larger systems. It has become evident in the past [40] that these weights fall off especially slowly for periodic boundary conditions. An explanation for this fact will be given in Sec. 7.6. Also, the DMRG does not perform well in two dimensions, because the number of block states one needs to keep depends exponentially on the width of the system. We will elaborate on what causes both problems and present possible solutions in Chapter 7.

6.2 Quantum Numbers and Symmetries

One way to greatly improve performance and to reduce memory usage in DMRG runs is to make use of the symmetries present in a model. If, for example, the number operator,

$$\hat{N} = \sum_{i=1}^{N} \sum_{\sigma=\uparrow,\downarrow} n_{i,\sigma}, \tag{6.6}$$

or the operator for the z-component of the total spin,

$$S_z = \sum_{i=1}^{N} (n_{i,\uparrow} - n_{i,\downarrow}), \tag{6.7}$$

commutes with the Hamiltonian, i.e.,

$$[H, N] = 0 = [H, S_z], \tag{6.8}$$

then the matrix representation of the Hamiltonian H as well as the reduced density matrix ρ are block-diagonal. Each of these blocks corresponds to a particular set of quantum numbers (N, S_z). Since, in practice, we are usually interested in the properties of a target state with a certain particle number and overall spin, we can reduce the basis of the Hilbert space that we need to consider and, therefore, the size of all operators as well as the wave function greatly. This approach can, in general, be used for all Abelian symmetries present in a given model and could therefore also be used for some of the symmetries mentioned in Sec. 2.2. However, the two symmetries mentioned above are those most commonly used. This is especially the case because, typically, local symmetries are not as straight forward to implement and are easily broken in many models, e.g., through impurities.

6.3 DMRG Algorithms

In this section, the two DMRG Algorithms [4, 5], the infinite system and the finite system algorithm, and the different steps of these algorithms will be discussed in a systematic fashion.

6.3.1 The Infinite System Algorithm

The infinite system algorithm in its original form [4] was designed to built up a system to a size as large as possible and observe the behaviour of interesting observables $f(L)$ in connection to the increasing size of the system L. Unfortunately, the infinite system algorithm suffers from convergence problems, for many systems. We will elaborate on these problems later in this section. The infinite system algorithm, or variations thereof, is still indispensable, since a good starting point for the finite system algorithm cannot be easily guessed in the case of larger systems. Therefore, it is needed to build up a system of suitable size that can be used as a starting point for the finite system algorithm.

The infinite system algorithm works as follows:

1. Start with a superblock of size L that is small enough to be exactly diagonalized. This superblock contains a system block of size l and a environment block of size l' with $l + l' = L$.

2. Build the superblock Hamiltonian $\tilde{H}_L$:

    (a) Construct the Hamilton operator on the system block $\tilde{H}_{ii'} = \langle i|H|i'\rangle$, where $|i\rangle, |i'\rangle$ are the basis states on the system block. Save this matrix in blocks sorted according to quantum numbers, i.e., $\tilde{H}_{ii'}^{N_1^S N_2^S S_{z,1}^S S_{z,2}^S}$.

    (b) Build the Hamilton operator on the environment block $\tilde{H}_{jj'} = \langle j|H|j'\rangle$, where $|j\rangle, |j'\rangle$ are the basis states on the environment block. Save this matrix in blocks sorted according to quantum numbers, i.e., $\tilde{H}_{jj'}^{N_1^R N_2^R S_{z,1}^R S_{z,2}^R}$.

    (c) Build the operators describing the interaction between the blocks, $\tilde{I}_{ii'} = \langle i|\tilde{I}|i'\rangle$ and $\tilde{I}_{jj'} = \langle j|\tilde{I}|j'\rangle$ on each block and save them sorted according to quantum numbers: $\tilde{I}_{ii'}^{N_1^S N_2^S S_{z,1}^S S_{z,2}^S}$ and $\tilde{I}_{jj'}^{N_1^R N_2^R S_{z,1}^R S_{z,2}^R}$.

    It is important to note that N_1 and N_2 are the particle number before and after the operator is applied, while $S_{z,1}$ and $S_{z,2}$ refer to the spin in the z-direction before and after the application of the operator, respectively.

3. Diagonalize the superblock Hamiltonian H_L to find the ground state with the quantum numbers we are interested in. For the diagonalization, either a Lanczos or Davidson diagonalization algorithm can be used. These algorithms are described in detail in Sec. 5.1. The most time-consuming operation that has to be carried out in all exact diagonalization algorithms is the multiplication $H_L|\psi\rangle$. This is done as a sum over all Hamilton operator blocks multiplied with the correspond-

ing block in the wave function. Therefore,

$$\begin{aligned}\psi_{i'j'}^{N_2^S N_2^R S_{z,2}^S S_{z,2}^R} = &\sum_{\substack{ij\\ N_1^S N_1^R\\ S_{z,1}^S S_{z,1}^R}} \tilde{H}_{ii'}^{N_1^S N_2^S S_{z,1}^S S_{z,2}^S} \delta_{jj'} \psi_{ij}^{N_1^S N_1^R S_{z,1}^S S_{z,1}^R}\\ &+ \sum_{\substack{ij\\ N_1^S N_1^R\\ S_{z,1}^S S_{z,1}^R}} \delta_{ii'} \tilde{H}_{jj'}^{N_1^R N_2^R S_{z,1}^R S_{z,2}^R} \psi_{ij}^{N_1^S N_1^R S_{z,1}^S S_{z,1}^R}\\ &+ \sum_{\substack{ij\\ N_1^S N_1^R\\ S_{z,1}^S S_{z,1}^R}} \tilde{I}_{ii'}^{N_1^S N_2^S S_{z,1}^S S_{z,2}^S} (\pm 1)^{N_1^S} \tilde{I}_{jj'}^{N_1^R N_2^R S_{z,1}^R S_{z,2}^R} \psi_{ij}^{N_1^S N_1^R S_{z,1}^S S_{z,1}^R}.\end{aligned}$$

Several things are important to point out here:

First, the state $|\psi\rangle$ can be written as a matrix because it is expressed in the product basis of the two blocks, i.e.,

$$|\psi\rangle = \sum_{ij} \psi_{ij} |i\rangle \otimes |j\rangle.$$

Second, the $(pm1$ is negative for fermions and positive for bosons and is introduced to ensure that the (anti-)commutation relations between different operators remain valid.

Third, to get the full representation of a state with particular quantum numbers $|\psi\rangle^{N,S_z}$, it is necessary to iterate over all possible combinations of these quantum numbers on the different blocks, i.e., $N_2^S + N_2^R = N$ and $S_{z,2}^S + S_{z,2}^R = S_z$.

Fourth, it is noteworthy that, even though for the Hamiltonian $N_1 = N_2$ and $S_{z,1} = S_{z,2}$ a general notation has been used that allows for $N_1 \neq N_2$ and $S_{z,1} \neq S_{z,2}$ since this is, in principle, possible for general operators.

4. Form the reduced density matrix for the different quantum numbers on the system block as

$$\rho_{ii'}^{N^S S_z^S} = \sum_{j N^R S_z^R} \left(\psi_{ij}^{N^S N^R S_z^S S_z^R}\right)^* \psi_{i'j}^{N^S N^R S_z^S S_z^R}.$$

5. Diagonalize $\rho_{ii'}^{N^S S_z^S}$ for all quantum numbers to obtain the eigenvalues and the corresponding eigenvectors. Keep the m eigenvectors with the

largest eigenvalues and at least one eigenvector for each set of quantum numbers so that every set of quantum numbers can gain additional weight during the course of the calculation.

6. Save the chosen eigenvectors and use them to transform the Hamilton operator (and other operators, e.g., observables) in the system block to the new basis:

$$\bar{X}_l^{N_1^S N_2^S S_{z,1}^S S_{z,2}^S} = \left(O_l^{N_2^S S_{z,2}^S}\right)^\dagger X_l^{N_1^S N_2^S S_{z,1}^S S_{z,2}^S} O_l^{N_1^S S_{z,1}^S}. \tag{6.9}$$

   Here the $O_l^{N^S S_z^S}$ contain the chosen eigenvectors in their columns and would therefore be unitary transformations if $m = \dim(H)$.

7. If needed, save the transformed operators for later use in the finite system algorithm.

8. The part that takes the most effort to understand correctly as well as to implement in an efficient way is adding two blocks. In this step, we have to distinguish between three different cases. If we have two blocks, block A and block B, then an operator can act only on block A, only on block B, or on both blocks. To describe these three cases, we will only use the particle number as a quantum number, because this saves notation effort and the generalization to spins is straightforward as long as a clear particle order is used.

   (a) The operator X acts only on block A. This means

$$X_{A+B}^{N_1^A N_2^A N^B} = X_A^{N_1^A N_2^A} \otimes \mathbb{I}_B^{N^B}.$$

   Here $\mathbb{I}_B^{N_B}$ is the identity matrix on block B in the subspace with quantum number N_B. The new operators $X_{A+B}^{N_1^A N_2^A N^B}$ are expressed in the new basis of the extended system but, in general, several of these operators fulfill the relations $N_1^A + N^B = N_1$ and $N_2^A + N^B = N_2$. Therefore the new operator $X_{A+B}^{N_1 N_2}$ must be built up from all of the operators which fulfill this condition, i.e.,

$$X_{A+B}^{N_1 N_2} = \begin{array}{c|ccccc} & \langle 0, N_1| & \langle 1, N_1 - 1| & \ldots & \langle N_1, 0| \\ \hline |0, N_2\rangle & X_{A+B}^{0,0,N_1}\delta_{N_1,N_2} & X_{A+B}^{1,0,N_1-1}\delta_{N_1-1,N_2} & \ldots & \\ |1, N_2 - 1\rangle & X_{A+B}^{0,1,N_1}\delta_{N_1,N_2-1} & X_{A+B}^{1,1,N_1-1}\delta_{N_1-1,N_2-1} & \ldots & \\ \vdots & \vdots & \vdots & \ddots & \\ |N_2, 0\rangle & & & & X_{A+B}^{N_1,N_2,0} \end{array}.$$

(b) The operator Y acts only on block B. This means

$$Y_{A+B}^{N^A N_1^B N_2^B} = (\pm 1)^{N^A} \mathbb{I}_A^{N^A} \otimes Y_B^{N_1^B N_2^B}.$$

Here $\mathbb{I}_A^{N^A}$ is the identity matrix on block A in the subspace with quantum number N_A. The new operators $Y_{A+B}^{N^A N_1^B N_2^B}$ are expressed in the new basis of the extended system, but the same problem as for the operators on block A arises here, too. Several of the newly build operators could fulfill the relations $N^A + N_1^B = N_1$ and $N^A + N_2^B = N_2$ and therefore the new operator $Y_{A+B}^{N_1 N_2}$ must be build from all of the operators which fulfill this condition, i.e.,

$$Y_{A+B}^{N_1 N_2} = \begin{array}{c|cccc} & \langle 0, N_1| & \langle 1, N_1 - 1| & \dots & \langle N_1, 0| \\ \hline |0, N_2\rangle & Y_{A+B}^{0,N_1,N_2} & 0 & \dots & \\ |1, N_2 - 1\rangle & 0 & Y_{A+B}^{1,N_1-1,N_2-1} & \dots & \\ \vdots & \vdots & \vdots & \ddots & \\ |N_2, 0\rangle & & & & Y_{A+B}^{N_1,0,0}\delta_{N_1,N_2} \end{array}.$$

(c) The operator Z acts on both blocks. This means

$$Z_{A+B}^{N_1^A N_2^A N_1^B N_2^B} = (\pm 1)^{\min(N_1^A, N_2^A)} Z_A^{N_1^A N_2^A} \otimes Z_B^{N_1^B N_2^B}.$$

The new operators $Z_{A+B}^{N_1^A N_2^A N_1^B N_2^B}$ are expressed in the new basis of the extended system, but, as in the two previous cases, several of the newly built up operators could fulfill the relations $N_1^A + N_1^B = N_1$ and $N_2^A + N_2^B = N_2$ and therefore the new operator $Z_{A+B}^{N_1 N_2}$ must be built up from all of the operators which fulfill this condition, as

$$Z_{A+B}^{N_1 N_2} = \begin{array}{c|cccc} & \langle 0, N_1| & \langle 1, N_1 - 1| & \dots & \langle N_1, 0| \\ \hline |0, N_2\rangle & Z_{A+B}^{0,0,N_1,N_2} & Z_{A+B}^{1,0,N_1-1,N_2} & \dots & \\ |1, N_2 - 1\rangle & Z_{A+B}^{0,1,N_1,N_2-1} & Z_{A+B}^{1,1,N_1-1,N_2-1} & \dots & \\ \vdots & \vdots & \vdots & \ddots & \\ |N_2, 0\rangle & & & & Z_{A+B}^{N_1,N_2,0,0} \end{array}.$$

Build H_{L+2} by adding two full sites between the system and the environment block using the method outlined above starting from the representation of H_L on these blocks. With the new Hamiltonian on the system and environment block, start over at step 3 and repeat steps 3-8 until the desired system size is reached.

As mentioned in the beginning of this section, the infinite system algorithm was originally designed to observe the dependence of interesting observables on the system size L. In the best case the resulting function $f(L)$, that describes the measurements, would follow a previously expected functional form or become L-independent for sufficiently large system sizes. Unfortunately this does not always occur for all interesting observables. This is mainly due to two reasons:

1. Some observables converge very slowly, e.g., logarithmically with system size towards the thermodynamic limit. Therefore, if the exact functional form of this system-size dependence is not known, an extrapolation to the thermodynamic limit is very difficult.
2. Since the system size changes continuously, it is not assured that the selection of basis states that was made earlier in the algorithm is still a sufficiently good choice for the system which is now larger.

The second problem, at least, can be solved by using an algorithm that always treats a system of the same size and converges further towards the true target state. This is the idea of the finite system algorithm.

6.3.2 The Finite System Algorithm

The finite system algorithm picks up where the build-up process, i.e., the infinite system algorithm, leaves off [4]. It takes a system of a given, fixed size and reevaluates the choice for the degrees of freedom on each site to make a better choice. Hence, allowing for a better approximation of the target state.

For the finite system algorithm, one proceeds as follows:

1. Use H_l^A, which has been stored during the build-up phase, two single sites, and $H_{l'=L-(l+2)}^B$ to build a new superblock which is the same size L as in the previous step.
2. Repeat steps 3-6 from the build-up phase to optimize the basis of the new left block A, which now consists of the old block A plus a single site. Store the newly found basis for the left block and set $(l \rightarrow l+1)$.
3. Repeat steps 1-2 until the entire system from left to right $(l = L-3)$ is gone through.
4. Change direction and reverse the roles of A and B. This means to use the stored versions of H_{l-1}^A and add two sites in the middle. This builds

up block B, reduces block A, and still leaves the overall system size L constant.

5. Repeat steps 1-2 with the roles of A and B reversed and set $(l \to l-1)$ at the end of each step, until the entire system from right to left is gone through $(l = 1, l' = L - 3)$.

6. Change direction again and reverse the roles of A and B. Start over at step 3.

7. Repeat step 3-6 until sufficient convergence has been reached, e.g., the ground-state energy does not change significantly anymore from one step to the next.

A pictorial representation for the finite system algorithm is given in Fig. 6.1, where solid lines denote a full basis and dashed lines denote a reduced basis. Red lines indicate the system block, which basis is optimized in that particular step, whereas blue lines denote the environment block, which is only used to provide an environment.

6.4 The Wave Function Transformation

The most time-consuming part of a DMRG calculation is always finding the ground state with an exact iterative diagonalization procedure as described in Sec. 5.1. All iterative diagonalization procedures have the feature that the number of iterations needed strongly depends on how close the starting vector is to the true target state. For a general step in the finite system algorithm, a very good starting guess is available: the calculated target state from the previous step in the finite system algorithm. Unfortunately, this wave function cannot be used in a straightforward manner, because it is given in the basis of the previous step, and therefore needs to be transformed to its representation in the basis of the current step. This is where the wave function transformation comes into play [4, 43].

Let us consider the basis of the superblock at a step l during a finite system sweep, which can be written as

$$|\alpha_l\ s_{l+1}\ s_{l+2}\ \beta_{l+3}\rangle = |\alpha_l\rangle \otimes |s_{l+1}\rangle \otimes |s_{l+2}\rangle \otimes |\beta_{l+3}\rangle, \tag{6.10}$$

where $|\alpha_l\rangle$ is the basis of block A containing sites $1, \ldots, l$, $|s_{l+1}\rangle$ and $|s_{l+2}\rangle$ are the bases of the single sites at position $l+1$ and $l+2$, and $|\beta_{l+3}\rangle$ is the basis of block B containing sites $l+3, \ldots, L$. If the algorithm is in a left-to-right

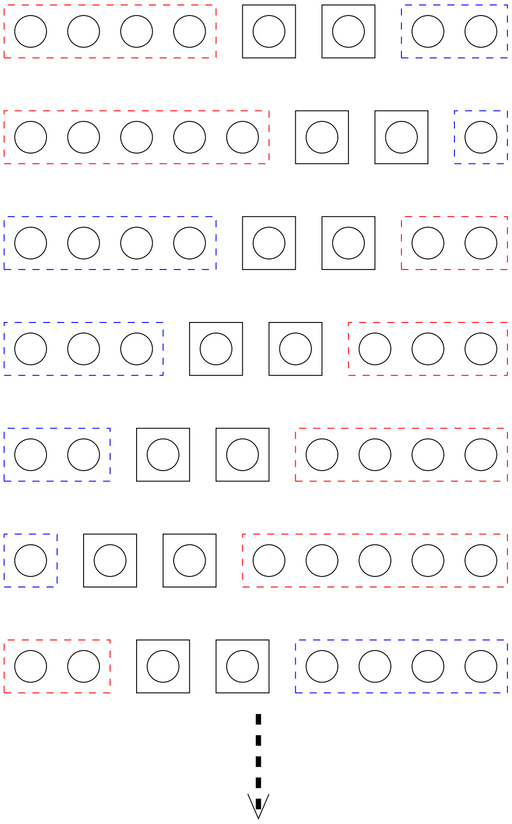

Figure 6.1: A pictorial representation of the finite system DMRG algorithm.

phase at this point, the basis in which the wave function would be needed in the next step is

$$|\alpha_{l+1}\ s_{l+2}\ s_{l+3}\ \beta_{l+4}\rangle. \tag{6.11}$$

Therefore, we need to transform the original product basis $|\alpha_l\rangle \otimes |s_{l+1}\rangle$ to the new basis $|\alpha_{l+1}\rangle$, the basis of the density matrix eigenvectors. Hence, we can write the transformation as

$$|\alpha_{l+1}\rangle = \sum_{\alpha_l, s_{l+1}} L^{l+1}_{\alpha_l, s_{l+1}, \alpha_{l+1}} |\alpha_l\rangle \otimes |s_{l+1}\rangle. \tag{6.12}$$

Here the transformation matrices $L^{l+1}_{\alpha_l, s_{l+1}, \alpha_{l+1}}$ can be viewed as $\dim(|s_{l+1}\rangle)$ different matrices, each of dimension $\dim(|a_{l+1}\rangle) \times \dim(|a_l\rangle)$.

As we have discussed in Sec. 6.3.1, the matrices that perform this function are the O matrices used in the basis transformation. They are therefore used in place of the L matrices. We also know that the right block was built up in a similar fashion, which is why we can write

$$|\beta_{l+3}\rangle = \sum_{s_{l+3}, \beta_{l+4}} R^{l+3}_{s_{l+3}, \beta_{l+4}, \beta_{l+3}} |s_{l+3}\rangle \otimes |\beta_{l+4}\rangle, \tag{6.13}$$

where $R^{l+3}_{s_{l+3}, \beta_{l+4}, \beta_{l+3}}$ is equal to the hermitian conjugate of the corresponding O matrices, that transformed the basis on that block to its current state in the first place. If we now write

$$|\psi\rangle = \sum_{\alpha_l, s_{l+1}, s_{l+2}, \beta_{l+3}} \psi\left(\alpha_l, s_{l+1}, s_{l+2}, \beta_{l+3}\right) |\alpha_l\ s_{l+1}\ s_{l+2}\ \beta_{l+3}\rangle, \tag{6.14}$$

we can easily find, by inserting $\sum_{\alpha_{l+1}} |\alpha_{l+1}\rangle\langle\alpha_{l+1}|$, that

$$\begin{aligned} &\psi\left(\alpha_{l+1}, s_{l+2}, s_{l+3}, \beta_{l+4}\right) \approx \\ &\quad \sum_{\alpha_l, s_{l+1}, \beta_{l+3}} L^{l+1}_{\alpha_l, s_{l+1}, \alpha_{l+1}}\ \psi\left(\alpha_l, s_{l+1}, s_{l+2}, \beta_{l+3}\right)\ R^{l+3}_{s_{l+3}, \beta_{l+4}, \beta_{l+3}}. \end{aligned} \tag{6.15}$$

This transformation is only approximate because the basis of the old right block $|\beta_{l+3}\rangle$ was truncated when it was built up. Therefore, the inverse transformation is not unitary in the new basis of the single site and the right block, $|s_{l+3}\rangle \otimes \beta_{l+4}\rangle$. Even though this is only an approximate transformation, it usually still leads to a considerable speed up (approximately a factor of 20-50) due to the fact that much fewer iterations are needed in the exact diagonalization algorithm. In addition, it also allows one to relax the convergence criterion in the exact diagonalization, because it is considerably less likely that the diagonalization routine converges to a local minimum; the starting vector is generally qualitatively correct and thus has a large overlap with the true target state.

The disadvantage of this transformation is, that, to be able to carry it out at every step in the finite system algorithm, one needs to store the transformation matrices (O matrices) at each step. Although storing such a large amount of data could potentially be very expensive in terms of memory, here, these matrices are only needed so rarely, that it is possible to save them on hard disk with almost no loss of efficiency. In addition, saving all of the transformation matrices allows one to transform all operators needed for measurements after convergence to the ground state has been achieved, which, in turn, saves memory during the DMRG run.

6.5 Measurements

So far we have discussed in detail how to find a good approximation ψ for a given target state within the DMRG, but it is clearly only of use if we can determine the value of observables afterwards. Hence we need to be able to calculate the matrix element

$$\langle\psi|A|\psi\rangle \tag{6.16}$$

for an arbitrary operator A.

In general, operators, which should be known to the best accuracy possible, are measured at the end of the DMRG run. Since, at this point, the superblock is in one particular state with a basis which is specifically chosen to optimally represent the target state, there is no simple relation between the original basis, which is just a tensor product of the bases on the different sites, and the now optimized basis. Therefore, before we are able to make a measurement, we must use the stored transformation matrices (O matrices, see Eq. (6.9)) to transform the relevant operators to the basis of the superblock. After this is done, Eq. (6.16) can be used directly to calculate the expectation value of the operator A.

In the special case of local operators, which act on two adjacent sites at most, it is possible to calculate the above matrix element at the step of the DMRG procedure at which that particular local operator acts on the two sites which have just been added to the system. If, for example, we want to measure an operator $A_{l,l+1}$, which acts on the sites l and $l+1$, we can calculate its expectation value when the superblock basis is given as

$$|\alpha_{l-1}\rangle \otimes |s_l\rangle \otimes |s_{l+1}\rangle \otimes |\beta_{l+2}\rangle,$$

because at that point the representation of this operator is directly known. The measurement can then be carried out directly after the diagonalization step. This does have the drawback though, that, since the measurements for local operators are done at different times during the DMRG sweeps, the operators that are measured early during the sweep are measured using a less converged wave function, than the operators measured during the end of the sweep. For this reason local operators, which are measured at different points during a sweep, are not suitable for comparison with each other.

Summary

In this chapter, we have described the basic idea of the DMRG algorithm, its different truncation schemes, and the details of the algorithm including using Abelian quantum numbers. We have also discussed the most important optimizations as well as how to measure observables with a converged target state.

A better intuition as to why the DMRG algorithm described here performs especially well on one-dimensional systems with open boundary conditions and why the convergence is significantly worse for periodic boundary conditions and for two-dimensional system will be build in the next chapter. We will also discuss recent developments which partially overcome these problems, such as matrix product states [43, 44] and projected entangled pair states [45, 46].

Chapter 7

DMRG using Tensor Networks

While the DMRG has proven to be extremely useful in the past two decades for one-dimensional quantum systems with open boundary conditions, it has great difficulties treating two-dimensional systems or even large one-dimensional systems with periodic boundary conditions. Recently, it has been shown that DMRG can also be described as a variational method over the class of matrix product states (MPS) [43, 47]. The MPS have a natural extension to higher dimensions or one-dimensional lattices with periodic boundary conditions. In the following, we will describe the DMRG algorithm as a variational optimization of a MPS in terms of tensor networks.

7.1 Tensors

What is a tensor? Unfortunately, the term is somewhat ambiguous, and this can sometimes lead to misunderstandings. The basic problem is that there are different default meanings for the word tensor in mathematics and in physics. In physics, the word "tensor" is often used to describe what mathematicians would call a tensor field. A tensor field associates a different mathematical tensor with each point in a geometric space, i.e., a tensor field varies continuously with position. An example is the stress tensor. Furthermore, even in mathematics there are two different notions of what a tensor is. The basic definition is, though, that a tensor is an element of a tensor product.

Let V and W be vector spaces over a common field K. Then the *tensor product*

$$V \otimes W \tag{7.1}$$

is also a vector space. Let $E = \{e_i | i \in I\}$ be a basis of V and $F = \{f_j | j \in J\}$

be a basis of W. Their Cartesian product,

$$E \times F = \left\{ \left(\vec{e_i}, \vec{f_j} \right) | i \in I,\, j \in J \right\}, \tag{7.2}$$

is then isomorphic to a basis for $V \otimes W$.

The first of the two notions mentioned above is that a tensor of rank (m, n), typically denoted τ^m_n, on a vector space V is an element in

$$\tau \in T^m_n(V) = \underbrace{V \otimes \cdots \otimes V}_{m} \otimes \underbrace{\hat{V} \otimes \cdots \otimes \hat{V}}_{n}, \tag{7.3}$$

where $\hat{V}$ denotes the dual space over V containing the linear functionals

$$f\ :\ V \longrightarrow K. \tag{7.4}$$

This notation of a tensor is, for example, typically used in the mathematical description of general relativity.

The other notion of a tensor is that if we have s distinct vector spaces, $V_1, \ldots, V_s$, then a tensor τ is an element of

$$\tau \in V_1 \otimes \cdots \otimes V_s. \tag{7.5}$$

This last notion of a tensor is used in the following and it should be clear that, given finite bases $B_1, \ldots, B_s$ on $V_1, \ldots, V_s$, an element $\tau \in V_1 \otimes \cdots \otimes V_s$ can always be expressed as a multi-indexed-array

$$A_{i_1, \ldots, i_s}$$

in these bases. For these multi-indexed-array representations of a tensor, we also introduce a graphical representation, shown in Fig. 7.1.

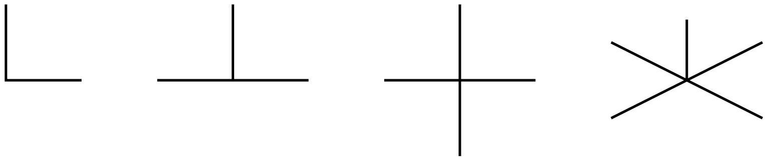

Figure 7.1: From left to right: A two-legged, three-legged, four-legged and five-legged tensor.

Here we have depicted two-legged, three-legged, four-legged, and five-legged tensors, where each leg that comes out of a vertex is the graphical representation for an array index. That the use of this graphical representation is immensely useful will become clear in the following.

7.2 Matrix Product States

A matrix product state [43, 44, 47] is a way to describe a quantum state $|\psi\rangle$ approximately or exactly as a product of matrices. If we consider a lattice of n sites, each of which contains d_s degrees of freedom, then the appropriate MPS would be

$$|\psi\rangle = \sum_{\{s_i\}=1}^{d_s} \mathrm{Tr}\left(A^{(1)}[s_1]A^{(2)}[s_2]\dots A^{(n)}[s_n]\right)|s_1\ s_2\dots s_n\rangle, \tag{7.6}$$

where the matrices $A[s_i]$ are typically square matrices, one for each degree of freedom s_i on each site. If we assume that each matrix has dimension $m \times m$ then this state cannot describe an arbitrary state in the full Hilbert space when

$$m < \sqrt{\frac{(d_s)^{n-1}}{n}}.$$

An equivalent formulation of a matrix product state that makes it easier to see the connection it has to tensors and their graphical representation, is

$$|\psi\rangle = \sum_{\{s_i\}=1}^{d_s} \sum_{i_1,i_2,i_3,\dots} A^{(1)}_{i_1,s_1}A^{(2)}_{i_1,i_2,s_2}A^{(3)}_{i_2,i_3,s_3}\dots A^{(n)}_{i_{n-1},s_n}|s_1\ s_2\ s_3\dots s_n\rangle. \tag{7.7}$$

Here there is an array with two indices at the beginning and the end of the matrix product and all other arrays have three indices. That is why we can represent this equation in terms of a tensor diagram such as that shown in Fig. 7.2. Here an index i_k between two tensors indicates that the legs left and right of it are both named i_k. If we would now contract all the connecting links (links with the same name) in the diagram, which would be equivalent to summing over all $i_1, \dots, i_{n-1}$ in (7.7), we would get, as a result, a tensor of size dim $(\mathcal{H})$, where $\mathcal{H}$ denotes the entire Hilbert space. Therefore, the size of $i_1, \dots, i_{n-1}$ determines the extent of the approximation that is made by writing a quantum state $|\psi\rangle$ as a MPS.

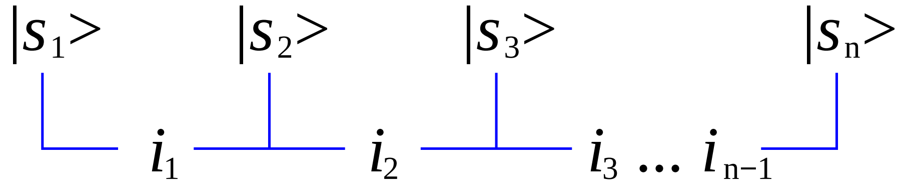

Figure 7.2: A matrix product state represented in terms of tensor diagrams.

7.3 Matrix Product Operators

Matrix product operators (MPO) [48] are a natural extension of matrix product states in which the operators are expressed as a matrix product and, hence, can be expressed via tensors and tensor diagrams as well. A typical Hamiltonian can then be written as

$$H = \sum_{s_1,\ldots,s_n,s'_1,\ldots,s'_n} \sum_{i_1,i_2,\ldots,i_{n-1}} H^{(1)}_{s_1,s'_1,i_1} H^{(2)}_{i_1,s_2,s'_2,i_2} \cdots H^{(n)}_{i_{n-1},s_n,s'_n}, \tag{7.8}$$

where $H^{(k)}_{i_{k-1},s_k,s'_k,i_k}$ contains the terms of the Hamiltonian acting on site k, s_k are the degrees of freedom on site k which the operator projects from, and s'_k are the degrees of freedom on site k which the operator projects to. The tensor diagram for a typical MPO can be seen in Fig. 7.3.

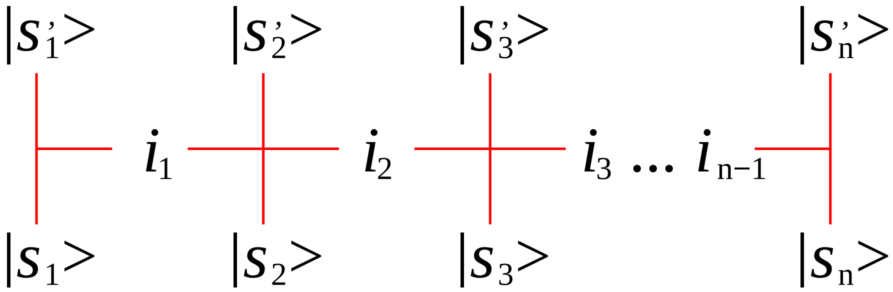

Figure 7.3: A matrix product operator represented as a tensor diagram.

As a typical example for a term in such an MPO, a term from a Heisenberg Hamiltonian,

$$H_{\text{Heis}} = \sum_{j+1}^{N-1} \left(J_x S^x_j S^x_{j+1} + J_y S^y_j S^y_{j+1} + J_z S^z_j S^z_{j+1} \right) + \sum_{j=1}^{N} \mu S^z_j, \tag{7.9}$$

is given:

$$H^k_{i_{k-1},i_k} = \begin{pmatrix} 1 & & & & \\ S^+_k & & & & \\ S^-_k & & 0 & & \\ S^z_k & & & & \\ \mu_k S^z_k & J_1 S^-_k & J_2 S^+_k & J_z S^z_i & 1 \end{pmatrix}, \tag{7.10}$$

where $S^+ = S^x + iS^y$ and $S^- = S^x - iS^y$ are the spin raising and spin lowering operators respectively, S^x, S^y, and S^z are the operators which measure the spin in x, y and z direction, μ is the local magnetization in z direction, $J_1 = J_x - J_y$, and $J_2 = J_x + J_y$. It is also noteworthy that each of the elements in the matrix (7.10) is again a matrix. This explains the notation of these terms in the tensors diagram as having four indices.

If we now let the MPO seen in Fig. 7.3 act on the MPS seen in Fig. 7.2, and then contract all the links that appear twice, we see that we, again, get a MPS. This is, of course, to be expected since letting an operator act on a state should result in a state again.

7.4 Singular Value Decomposition

To understand DMRG in terms of tensor networks it is essential to also understand the Singular Value Decomposition (SVD) [49, 50] and its use within the DMRG framework. Let us consider a four legged tensor as depicted in Fig. 7.4, which we would get by contracting the tensors corresponding to two sites, and thereby making all the degrees of freedom on these two sites available. Let us now assume that we have optimized the state represented by these two tensors and want to disjoin them, while only keeping m states between them. To achieve that and still having an optimal approximation to the original state is exactly what we need the SVD for.

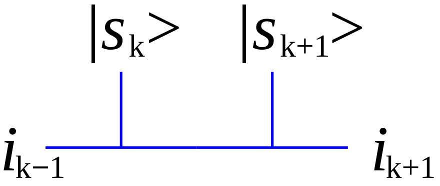

Figure 7.4: A contracted pair of tensors corresponding to two sites.

Unfortunately, the SVD acts on matrices. Therefore, we need to find a way to map our four legged tensor onto a matrix. This is done by combining the two leftmost indices, i_{k-1} and s_k, into an index m and the two rightmost indices, s_{k+1} and i_{k+1}, into an index n, as depicted in Fig. 7.5. It is obviously necessary for the mapping function to be bijective. After the indices are combined, we can view the tensor as a matrix A with the indices m and n. Now the SVD decomposes the matrix A into two other matrices as

$$A = U\Sigma V^{\dagger}, \tag{7.11}$$

where U is an $\dim(m) \times \dim(m)$ matrix containing the left singular vectors in its columns, V is a $\dim(n) \times \dim(n)$ matrix containing the right singular

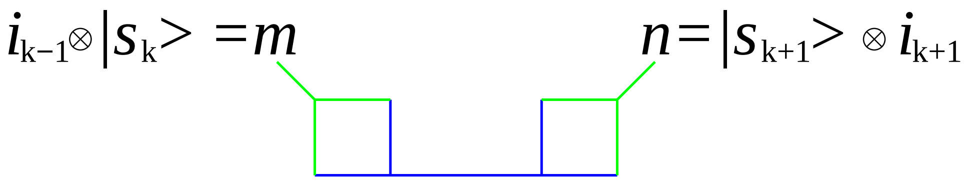

Figure 7.5: A four legged tensor with the indices combined to form a matrix.

vectors in its columns, and Σ is a $\dim(m) \times \dim(n)$ matrix which holds the singular values in its diagonal elements. If we now make the identification $B = U$ and $C = \Sigma V^\dagger$ we can write

$$A_{m,n} = \sum_{i_k} B_{m,i_k} C_{i_k,n}. \tag{7.12}$$

This allows us to draw the tensor diagram as shown in Fig. 7.6 where we have reverted the mapping of the two left and two right indices onto m and n.

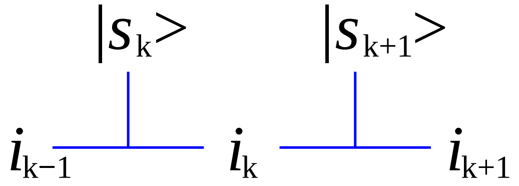

Figure 7.6: The two tensors from Fig. 7.4 now disjoint.

We can see here, that, just like in Chapter 6, we get the best approximation to the original matrix/tensor if we keep the m left and right singular vectors that correspond to the highest singular values. This allows for the same truncation schemes as described in Sec. 6.1.

7.5 The DMRG Algorithm

For the sake of simplicity and brevity, we will discuss only the finite system algorithm here, since a good grasp of the finite size algorithm should enable anybody to understand the idea of the infinite system algorithm as well, because it has a similar structure and is based on the same principles.

In a matrix-product formulation the finite system algorithm proceeds as follows.

1. Choose a subspace of two sites to optimize.
2. Contract all links in this subspace that can be contracted (see Fig. 7.4).
3. Use an iterative exact diagonalization routine (see Sec. 5.1) to find the target state on the chosen subspace. It is important to note that, to achieve this, the Hamiltonian must only act on that subspace and nowhere else. A tensor diagram for such a Hamiltonian is shown in Fig. 7.7.
4. Use the SVD to disjoin the tensors in the chosen subspace and truncate to the desired number of states.
5. Start over at step 1.

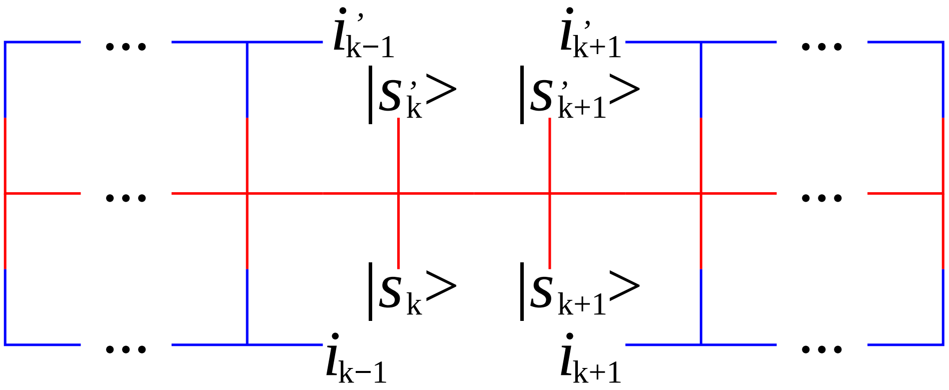

Figure 7.7: Tensor network diagram of a Hamiltonian which only acts on two sites.

It should now be clear that using MPS greatly simplifies the DMRG algorithm. In particular, one should note that two of the most difficult steps in the DMRG, the basis transformation described in Sec. 6.3.1 and the wave function transformation described in Sec. 6.4, are done completely implicitly and do not put any strain on the programmer. The other advantages of MPS, such as better convergence for periodic boundary conditions and two-dimensional systems, will be described in the following.

7.6 Periodic Boundary Conditions

The fact that periodic boundary conditions are hard to treat using the DMRG can be described in two different ways. It is an empirical fact that the eigenvalues of the reduced density matrix fall off more slowly for periodic boundary conditions, than they do for open boundary conditions. Therefore, we need to keep a higher number of states m to get the same accuracy for systems of the same size. Hence, we are restricted to treating smaller systems if we require the same accuracy as for open boundary conditions.

Another way of explaining the same fact in a more intuitive but also more hand-waving way is to say that the interactions between the first and the last site have to be encoded into the entire system because there is no direct *connection* between those two sites in the representation of the target state. This additional information, which is encoded in the system, increases the entanglement between the two blocks, independent of where the superblock is cut, and therefore the number of states m that must be kept to reach a given accuracy in the approximation increases.

The evident way to approach this is to use a representation that contains such a *connection* between the first and the last site. Then, the necessary information about the interactions between these two sites can be encoded there directly and therefore does not increase the entanglement within the system as much. Using MPS, such a representation naturally has the form of a ring state. An example of such a state is shown in 7.8.

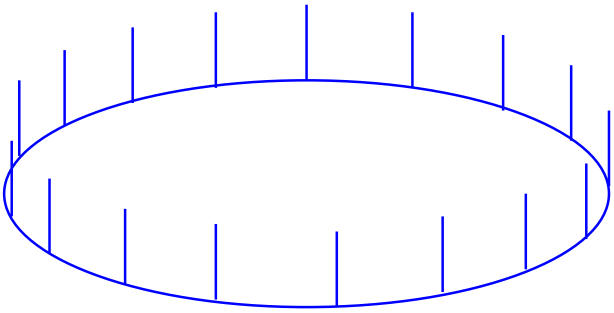

Figure 7.8: An MPS ring state, used to better represent a target state with periodic boundary conditions.

7.7 Two-Dimensional Systems

The poor performance of the DMRG algorithm for two dimensions is mainly due to the fact that two-dimensional systems have to be mapped onto one-dimensional systems in order to apply the DMRG algorithm. For this purpose, a path through the system must be chosen. The DMRG algorithm is then performed along this path. A typical example of such a mapping is shown in Fig. 7.9, where the red dashed line denotes the system block, the blue dashed line denotes the restblock, and the two solid blocks are the two single sites, which are reintroduced into the system in that particular step. The dotted line shows the path the algorithm takes through the system. In such a system, the number of states one needs to keep to reach a certain accuracy rises exponentially with the system width [51, 52]. Therefore, calculations are only possible for small system width and can only poorly approximate real two-dimensional materials.

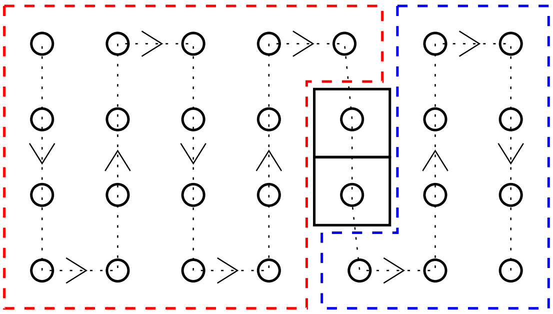

Figure 7.9: A superblock in a two-dimensional system. The system block has a red and the restblock a blue outline. Dashed lines stand for truncated, solid lines for full bases.

The root of the problem is the same as for periodic boundary conditions. If we consider, for example, the first and the eighth site in Fig. 7.9, we can immediately see that, since these two sites are direct neighbours, they will interact strongly, but the mapping onto a one-dimensional chain places them seven sites apart. Therefore, the information coming from the interaction between these two sites has to be encoded into all the intermediate links. This fact is true for all sites in the system and obviously greatly increases the entanglement between the system block and the rest block at any given step of the algorithm, forcing us to keep many more states to reach a desired accuracy.

As in the case of periodic boundary conditions, MPS can be naturally extended to accommodate the additional needs of two-dimensional systems. These extended states are called projected entangled pair states.

7.7.1 Projected Entangled Pair States

Projected entangled pair states (PEPS) [45, 46] use higher dimensional tensors, e.g., five-dimensional tensors for two-dimensional systems on a square lattice, to encode all the information between two sites directly. A representation of such a state in the form of tensor diagrams is depicted in Fig. 7.10. Here the links between the different sites encode the interaction between them and, the links sticking out upwards represent the degrees of freedom on that particular site. It can be shown that the computational complexity of simulating a PEPS grows only polynomially with its size [53], and, for the DMRG, algorithms have been devised that grow with m^{10} in computational complexity, where m is the number of states kept in the links between sites.

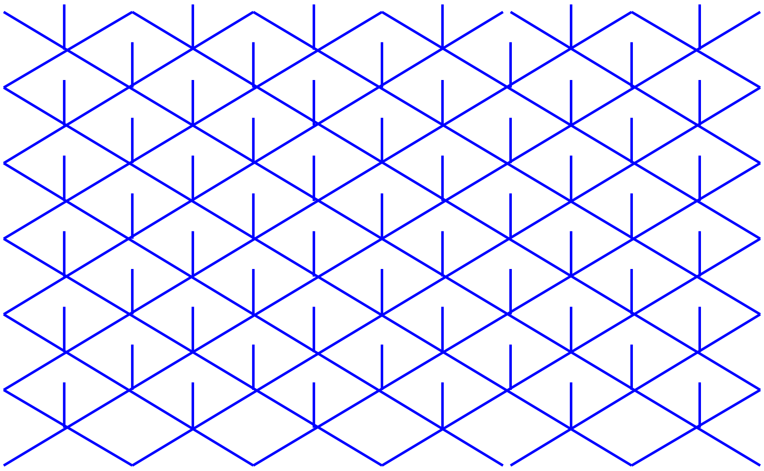

Figure 7.10: A PEPS state for a two-dimensional system.

Summary

In this chapter we have described the DMRG algorithm in terms of tensor networks. For this purpose we introduced matrix product states and explained how they can be used to approximate arbitrary quantum states. We then introduced matrix product operators, which represent regular linear operators on a Hilbert space as a product of matrices. To simplify notations and alleviate the problems of understanding the DMRG algorithm we introduced a diagram representation for matrix product states and matrix product operators. Using these diagrams we then explained the original DMRG algorithm in a step-by-step fashion. Lastly we explained extensions to the DMRG algorithm, namely ring states and projected entangled pair states, that allow for a faster and more precise treatment of system with periodic boundary conditions and two-dimensional systems.

Chapter 8

Time Evolution

In quantum mechanics, the time evolution of a system is governed by the time-dependent Schroedinger equation

$$i\frac{\partial}{\partial t}|\psi\rangle = H|\psi\rangle. \tag{8.1}$$

When the Hamiltonian H is time-independent, Eq. (8.1) has the formal solution

$$|\psi(t)\rangle = e^{-iHt}|\psi(0)\rangle. \tag{8.2}$$

Hence, to calculate the exact time evolution operator e^{-iHt} one would have to know all of the eigenvalues of H as well as the according eigenvectors. Since the DMRG and the exact diagonalization algorithms are both based on finding extremal eigenstates in a reduced Hilbert space, solving H completely to obtain all eigenvalues would render the whole exercise moot. Therefore, one is left with two options [54]:

1. Iteratively solve Eq. (8.1) using a differential equation solver.
2. Find a suitable approximation for e^{-iHt} and then use Eq. (8.2).

For the first method, various differential equation solvers have been devised in the past, e.g., Runge-Kutta. Therefore, we will discuss two possibilities in the following, that utilize the second method.

8.1 Time Evolution Using Exact Diagonalization

One way of approximating e^{-iHt} is to approximate H using an iterative exact diagonalization procedure as discussed in Sec. 5.1. Afterwards, $\tilde{H}$ is diagonalized and the resulting diagonal matrix can be exponentiated. After this is done, one has to transform the exponentiated diagonal matrix back to the original basis of H. As an example, we will discuss this in more detail using a Lanczos diagonalization algorithm.

Let us consider a given Hamilton matrix H for which we want to find the exponential e^{-iHt}. We build the tridiagonal approximation $\tilde{H}$ to H and store the corresponding Lanczos vectors in the columns of a matrix V. Since $\tilde{H}$ is considerably smaller than H, it can be fully diagonalized, yielding all of its eigenvalues and eigenvectors:

$$\tilde{H} = O \Sigma O^\dagger.$$

Here Σ is the diagonal matrix containing the eigenvalues of $\tilde{H}$, and O contains the eigenvectors of $\tilde{H}$ in its columns. Thus, the exponential $e^{-i\Sigma t}$ is a diagonal matrix with

$$\left(e^{-i\Sigma t}\right)_{ii} = e^{-i(\Sigma)_{ii} t}.$$

This yields

$$|\psi(t)\rangle = e^{-iHt}\,|\psi(0)\rangle \approx V\,O\,e^{-i\Sigma t}\,O^\dagger\,V^\dagger\,|\psi(0)\rangle. \tag{8.3}$$

The error made in this approximation can be shown to have an upper bound [55] given by

$$\begin{aligned} \epsilon &= \|\, |\psi(t)\rangle - |\psi(t)\rangle_{\text{approx}} \,\| && (8.4)\\ &\leq 12 \exp\left(-\frac{(\rho t)^2}{16n}\right)\left(\frac{e\rho t}{4n}\right)^n, && (8.5)\\ \text{with} \quad n &\geq \frac{1}{2}\rho t, && (8.6) \end{aligned}$$

where $\rho = \mathrm{E}_{\max} - \mathrm{E}_{\min}$ is the width of the spectrum of H, n is the number of Lanczos vectors used, and e is the Euler number. To keep the overall error small, one usually splits a desired time interval T up into many short time steps dt and performs the time evolution stepwise.

8.2 Time Evolution Using Trotter Decomposition

The DMRG algorithm can be conveniently used with a second-order Trotter decomposition [56],

$$e^{-iHdt} \approx e^{-iH_{\text{odd}}dt/2} e^{-iH_{\text{even}}dt} e^{-iH_{\text{odd}}dt/2}. \tag{8.7}$$

Here we have grouped the Hamiltonian into local Hamiltonians on odd and even bonds. For this grouping to be possible, the Hamiltonian cannot have more then nearest-neighbor interaction terms. The "≈" sign indicates that this decomposition is not exact but that the error ϵ is, in fact, $\mathcal{O}(dt^2)$. At any given step in the DMRG algorithm, the two central sites in the superblock are represented in a full basis. Therefore, the term in the Hamiltonian that acts on that bond can be applied exactly. A drawback of the Trotter decomposition is that, to complete a time step of size dt, one has to carry out at least three sweeps through the system, one sweep each for applying $e^{-iH_{\text{odd}}dt/2}$ twice, separated by one sweep for applying $e^{-iH_{\text{even}}dt}$. Therefore, depending on the model, either the Lanczos expansion of e^{-iHt} or the Trotter decomposition could be more efficient.

8.3 Basis Adaptation

One problem that has not yet been discussed is how well a time-evolved vector can be represented in a basis that is optimized to represent a specific target vector. The answer is, plain and simple, worse and worse with increasing time if the vector is not an eigenvector of the Hamiltonian H. The obvious solution to this problem is that the new vector should be mixed into the density matrix after each time step to ensure that it is represented sufficiently well within the chosen subspace of the Hilbert space. The problem with this answer is that an increasing number of other states must get mixed into the density matrix. Since we already know that many of the degrees of freedom for time-evolved states do not overlap with the original target state (otherwise a basis adaption wouldn't even be necessary), it is not surprising that the number of states that one needs to keep would increase extremely fast if this were done. The idea that is usually used to circumvent this problem, at least to some degree, is to adapt the basis during each time step only to the states at the beginning and at the end of the time step. Thus, for the step

$$|\psi\,(t+dt)\rangle = e^{-iH\,dt}|\psi(t)\rangle, \tag{8.8}$$

we would only adapt the basis to $|\psi(t+dt)\rangle$ and $|\psi(t)\rangle$ thereby discarding all the other degrees of freedom from previous time steps. This is fortunately not a problem since these degrees of freedom are not needed anymore. Different basis adaption schemes are typically used when a Trotter decomposition time evolution scheme is used. In that case usually not only the first and the last step in the time evolution but also all intermediate steps are mixed into the density matrix. Similar ideas have also been used for time evolution algorithms that iteratively solve the Schroedinger equation (8.1), e.g., Runge-Kutta, but as long as the degrees of freedom which are important for states that are needed in a time evolution step are present the basis adaption works similarly well for all kinds of time evolution schemes.

In general, making a sudden change in the Hamiltonian of a system which is in the ground-state, throws the system into an initial state that is higher in energy, and therefore makes the target state we want to evolve in time a superposition of many excited states. That is why the basis adaption still does not rid us completely of the problem of having to keep more states for an accurate representation of our time evolved target state $|\psi(t)\rangle$ than we needed to represent the ground-state. It does significantly raises the accuracy in comparison to not adapting the basis, though.

Chapter 9

Dynamics

The prediction of dynamical correlation functions is a very important task for theoretical physics because such quantities are typically measured by scattering experiments. Therefore, predictions for dynamical correlation functions are among the quantities that are comparably easy to verify experimentally. Unfortunately, the prediction of dynamical correlation functions is, especially in condensed matter physics, a very challenging task and is possible analytically only to a very limited extend.

The zero-temperature dynamical response of a system is fully determined by its retarded Green's function (4.7) and is given by the Fourier transform of the time-ordered Greens function with a small imaginary part, added to achieve convergence,

$$G_{A,A^\dagger}(\omega) = G^U_{A,A^\dagger}(\omega) + G^L_{A^\dagger,A}(\omega) \tag{9.1}$$

$$G^U_{A,A^\dagger}(\omega) = \lim_{\eta\to 0^+} \left\langle \psi \left| A \, \frac{1}{E_0 + \omega + i\eta - H} \, A^\dagger \right| \psi \right\rangle \tag{9.2}$$

$$G^L_{A^\dagger,A}(\omega) = \lim_{\eta\to 0^+} \left\langle \psi \left| A^\dagger \, \frac{1}{H + \omega + i\eta - E_0} \, A \right| \psi \right\rangle . \tag{9.3}$$

Here $G^U_{A,A^\dagger}(\omega)$ denotes the part of the Green's function corresponding to excitations which are higher in energy, and $G^L_{A^\dagger,A}(\omega)$ denotes excitations lower in energy. What is measured in scattering experiments is the spectral function, which is the imaginary part of the dynamical correlation function

$$I^U_{A,A^\dagger}(\omega) = \Im\left(G^U_{A,A^\dagger}(\omega)\right) \tag{9.4}$$

$$= \sum_n \left|\left\langle \psi_n \left| A^\dagger \right| \psi \right\rangle\right|^2 \delta\left(\omega + E_0 - E_n\right). \tag{9.5}$$

A short derivation of the above two formulae can be found in appendix B. In the following, we will introduce three numerical methods based on the

DMRG which all are suitable to predict dynamical correlation functions and which take different approaches to calculate Eq. (9.5).

9.1 Continued Fraction Method

A fairly straightforward way of calculating (9.3) is to use the Lanczos method. If we choose

$$|u_0\rangle = \frac{1}{\sqrt{\langle\psi|AA^\dagger|\psi\rangle}} A^\dagger|\psi\rangle \tag{9.6}$$

as our starting vector and then build up the corresponding Krylov space as

$$\{|u_0\rangle, H|u_0\rangle, H^2|u_0\rangle, H^3|u_0\rangle, \dots\}, \tag{9.7}$$

we are not only tridiagonalizing H, but also the resolvent operator

$$\frac{1}{E_0+\omega+i\eta-H}. \tag{9.8}$$

In this basis, the dynamical correlation function is directly given as [57]

$$G_{A,A^\dagger}(z=\omega+i\eta) = \cfrac{\langle\psi|AA^\dagger|\psi\rangle}{z-a_0-\cfrac{b_1^2}{z-a_1-\cfrac{b_2^2}{z-a_2-\dots}}}. \tag{9.9}$$

This expression is derived in Appendix D.

The method has some drawbacks, though. As pointed out in Sec. 5.1, the Lanczos diagonalization algorithm usually loses orthogonality after a fairly small number of steps. Therefore, the continued fraction expansion cannot necessarily be carried out long enough to find all important poles. It only works if the weights of the poles decrease sufficiently fast. Also, the resulting spectral function will consist of delta peaks which have to be convolved with a broadening function, e.g., a Lorentzian, to give a smooth spectrum. This makes it very difficult to determine boundaries in the density of states and, therefore, for example, gaps precisely. In addition, if the operator A is momentum dependent, e.g., $c_k^\dagger$, then the calculation has to be repeated for each k.

9.2 Dynamical DMRG

The dynamical DMRG (DDMRG) determines the dynamical correlation function via a variational principle [58]. We will follow [59, 60] for its description.

It is evident from Eq. (9.3) that if we know the correction vector, defined as

$$|\psi_A(\omega + i\eta)\rangle = \frac{1}{E_0 + \omega + i\eta - H} A|\psi\rangle, \tag{9.10}$$

we can easily calculate the dynamical correlation function. The correction vector can be split up into its real and its imaginary parts,

$$|\psi_A(\omega + i\eta)\rangle = |X_A(\omega + i\eta)\rangle + i|Y_A(\omega + i\eta)\rangle, \tag{9.11}$$

which are related to one another by

$$|X_A(\omega + i\eta)\rangle = \frac{H - E_0 - \omega}{\eta} |Y_A(\omega + i\eta)\rangle \tag{9.12}$$

due to the properties of the underlying Green's function. Knowing this, the problem of calculating Eq. (9.3) can be expressed as an inhomogeneous linear equation

$$\left[(E_0 + \omega - H)^2 + \eta^2\right] |\phi\rangle = -\eta\, A|\psi\rangle, \tag{9.13}$$

which has the unique solution

$$|\phi\rangle = |Y_A(\omega + i\eta)\rangle, \tag{9.14}$$

because

$$\Im\left(G_{A^\dagger,A}(\omega + i\eta)\right) = \frac{1}{\pi} \left\langle \psi \middle| A^\dagger \frac{\eta}{(E_0 + \omega - H)^2 + \eta^2} A \middle| \psi \right\rangle. \tag{9.15}$$

Solving Eq. (9.13) can be accomplished by using iterative algorithms such as these described in Sec. 5.1. Such algorithms yield approximate results containing at least a numerical error on the order of the stopping criterion ϵ. Since

$$\Im\left(G_{A^\dagger,A}(\omega + i\eta)\right) = -\frac{1}{\pi}\langle\psi|A^\dagger|Y_A(\omega + i\eta)\rangle, \tag{9.16}$$

the error in the spectrum would then be proportional to ϵ. Instead, one can formulate the problem as a minimization problem in which one treats the functional

$$W_{A,\eta}(\omega, \phi) = \langle\phi|(E_0 + \omega - H)^2 + \eta^2|\phi\rangle + \eta\langle\psi|A^\dagger|\phi\rangle + \eta\langle\phi|A|\psi\rangle. \tag{9.17}$$

This functional has a well-defined and non-degenerate minimum given by

$$|\phi_{\text{min}}\rangle = |Y_A(\omega + i\eta)\rangle. \tag{9.18}$$

for any $\eta \neq 0$ at any fixed frequency ω. This yields

$$W_{A,\eta}(\omega, \phi) = -\pi\, \eta\, I_{A^\dagger,A}(\omega + i\eta). \tag{9.19}$$

The DDMRG algorithm, which is based on these considerations now proceeds as follows:

1. Find the ground state $|\psi\rangle$ and the ground-state energy E_0 on a given superblock.
2. Calculate $A|\psi\rangle$.
3. Minimize the functional $W_{A,\eta}(\omega,\phi)$ using a minimization method, e.g., a conjugate gradient method, yielding $|Y_A(\omega+i\eta)\rangle$.
4. Calculate $|X_A(\omega+i\eta)\rangle$ using (9.12).
5. Include $|\psi\rangle$, $A|\psi\rangle$, $|Y_A(\omega+i\eta)\rangle$ and $|X_A(\omega+i\eta)\rangle$ in the density matrix as target states and build a new system block.
6. Start over with step 1 until the ground state as well as the functional $W_{A,\eta}(\omega,\phi)$ are converged to their respective minima.

Using this method, very precise results for a given ω can be obtained. Unfortunately, the calculation optimizes the reduced basis of the Hilbert space for a certain ω and, the calculation therefore has to be repeated for every ω. There are certain optimizations possible such as picking a "smart" starting vector or including states with different ω in the density matrix and interpolating, but these optimization won't be discussed here. The reader is referred to Refs. [59] and [60] and references therein for further reading.

9.3 Time Evolution and Fourier Transformation

The final DMRG method for calculating dynamical correlation functions that we will discuss here makes use of the time-evolution capability of the DMRG [54] described in Chapter 8. It calculates the retarded Green's function (4.7) directly as

$$\begin{aligned} G^{\mathrm{ret}}_{A,A^\dagger}(t) &= -i\Theta(t)\left\langle \left[A(t),A^\dagger(0)\right]_\pm \right\rangle \\ &= -i\Theta(t)\left(e^{iE_0t}\langle\psi|A|\chi(t)\rangle \pm e^{-iE_0t}\langle\chi(-t)|A|\psi\rangle\right), \end{aligned} \tag{9.20}$$

with $|\chi(t)\rangle := e^{-iHt}A^\dagger|\psi\rangle$.

We can see here that, if we time-evolve $A^\dagger|\psi\rangle$, we only need to multiply $|\psi\rangle$ by e^{iE_0t} to obtain all the necessary ingredients to form the retarded Green's function. A few issues must nevertheless be addressed. If one wants to measure the matrix element $\langle\psi|A|\chi(t)\rangle$ for different operators A, for example, these A either must be adapted to the correct basis before a measurement can be made, or, if they are local operators, the matrix element must be measured when the sites A acts on are the two exactly treated sites in the DMRG algorithm (see Sec. 6.3.1). Also, to avoid strong boundary effects in the behavior of the retarded Green's function, one should take into account the speed with which the perturbation, caused by $A^\dagger$, travels through the system and choose the length of the time interval for the time evolution T to be short enough so that the perturbation is not reflected from the end of the system. This effectively limits the resolution in ω for the spectral function. This issue will be discussed in more detail later.

9.3.1 Extrapolation in Time

One way to counter this effect is to carry out a time evolution for a certain time T and then extrapolate to larger times either using some *a priori* knowledge of the model and the corresponding Green's function or, if nothing is known about the model, using linear prediction [61]. The idea of linear prediction is to use the last p points in a data series to predict the value of the next point. The value of the predicted point is given by

$$\tilde{x}(n) = -\sum_{i=1}^{p} a_i x(n-i). \tag{9.21}$$

The parameters a_i must be chosen using an appropriate method. The most common method uses a root-mean-square or autocorrelation criterion. Using the root-mean-square method, we minimize

$$\chi = \sum_n \left(x(n) - \tilde{x}(n)\right)^2 \tag{9.22}$$

for the data points we already know. This yields the equations

$$\sum_{i=1}^{p} a_i R(i-j) = -R(j), \qquad j = 1, \ldots, p, \tag{9.23}$$

where $R(i)$ is the autocorrelation, defined as

$$R(i) = \frac{E\left\{(x(n)-\mu_x)(x(n-i)-\mu_x)\right\}}{\sigma_x^2}, \tag{9.24}$$

where μ_x denotes the arithmetic mean of the data series x, and σ_x is its standard deviation.

Eq. (9.23) can also be written in matrix form as

$$R\,a = -r, \tag{9.25}$$

where R is the autocorrelation or Toeplitz matrix with $(R)_{i,j} = R(i-j)$, and r is the autocorrelation vector with $r_j = R(j)$. From this it is clear that a is given by

$$a = -R^{-1}r, \tag{9.26}$$

where R^{-1} always exists because the Toeplitz matrix is symmetric. It should be noted that this kind of prediction only works well if the extrapolated signal is stationary, meaning that $R(i)$ is independent of the contiguous subset of the data we choose to calculate it from, or, in other words, if the signal has no strong non linear effects.

9.3.2 Discrete Fourier Transform

To transform the raw data for the retarded Green's function (4.7) that we obtain from the time evolution to the spectral function (9.5) we desire, we must carry out a Fourier transform. Unfortunately, we only have a finite set of data points, and they have a discrete spacing and a limited range. Therefore, we are limited to performing a discrete Fourier transform (DFT), which imposes limits on the frequency resolution and on the maximum value of the energy domain.

$$\Delta\omega = \frac{2\pi}{T}, \tag{9.27}$$

$$\Omega = \frac{\pi}{\Delta t}, \tag{9.28}$$

where Ω and T are the maximum energy and time, and $\Delta\omega$ and Δt are the intervals between points in energy and time respectively. It should now be clear, that the maximum time T for time evolution is limited on small systems, due to boundary effects, in turn, limiting the resolution $\Delta\omega$ in energy. Therefore, to achieve a high resolution in energy, a large numerical effort is necessary because the calculation time scales linearly with the system size and with the length of the time evolution. In addition, more states m must be kept as the system size or length in time is increased, and the numerical effort scales as m^3. In total, the computation time therefore scales as $\mathcal{O}(\frac{1}{(\Delta\omega)^5})$.

A big advantage of this method is that a different operator A can be measured at every step in the DMRG algorithm. We can, for example, make measurements for each wave number k in one run for the case $A^\dagger = c_k^\dagger$. This speeds up calculations tremendously.

Spurious Values in the Spectral Function

A problem that one encounters when using time evolution to calculate the retarded Green's function is that, on the one hand, there is a limit as to how far one can go in time due to accuracy constraints and due to boundary effects. On the other hand, when one calculates the retarded Green's function up to a certain point in time, one can never be sure all oscillations in the system that are important have been resolved. In fact, for any finite system, there is a recurrence time after which a perturbed system returns to its original state. This recurrence time grows extremely fast with system size and is therefore virtually impossible to reach with numerical time-evolution schemes. In the following, we will discuss the effect of taking the Fourier transform of a Green's function that is only calculated up to a limited point in time as well as how it can be compensated to some extent.

For this purpose, we have artificially created a signal which is similar but not identical to the Fourier transformation of the retarded Green's function of the tight binding model (2.2). This signal is shown in Fig. 9.1. If we now take the inverse Fourier transformation of this signal, we get a signal that corresponds to the actual retarded Green's function that we would *measure* with our program if the underlying model had a density of states as depicted in the lower picture in Fig. 9.1. The real part of this signal is shown in Fig. 9.2. The imaginary part is very similar to the real part and is therefore not shown.

Now we cut off the signal shown in Fig. 9.2 at the red vertical line and Fourier transform back to the frequency domain. As can be seen, the Fourier transform of the truncated signal in Fig. 9.3 shows some values which are smaller than zero and are thus clearly spurious at approximately $x = 40$ (blue line). This "overshooting" is due to the truncation of the time signal at a certain point in time and can, to some extent, be compensated by multiplying the signal with a filter function, e.g., a Kaiser window [62], before Fourier transforming (green line). While this reduces the magnitude of the spurious negative values, it does not compensate them completely. It should also be pointed out that these kinds of errors do not shift the positions of the peaks nor do they significantly change the height of the peaks, as long as a good filter function is used.

Such spurious values will appear again in the results shown in Chapter 12, but one should keep in mind that they are artifacts that are solely due to the discrete Fourier transformation and due to the calculation of the retarded Green's function over a finite time range. They are therefore unavoidable and do not stem from problems in the algorithm or the data analysis.

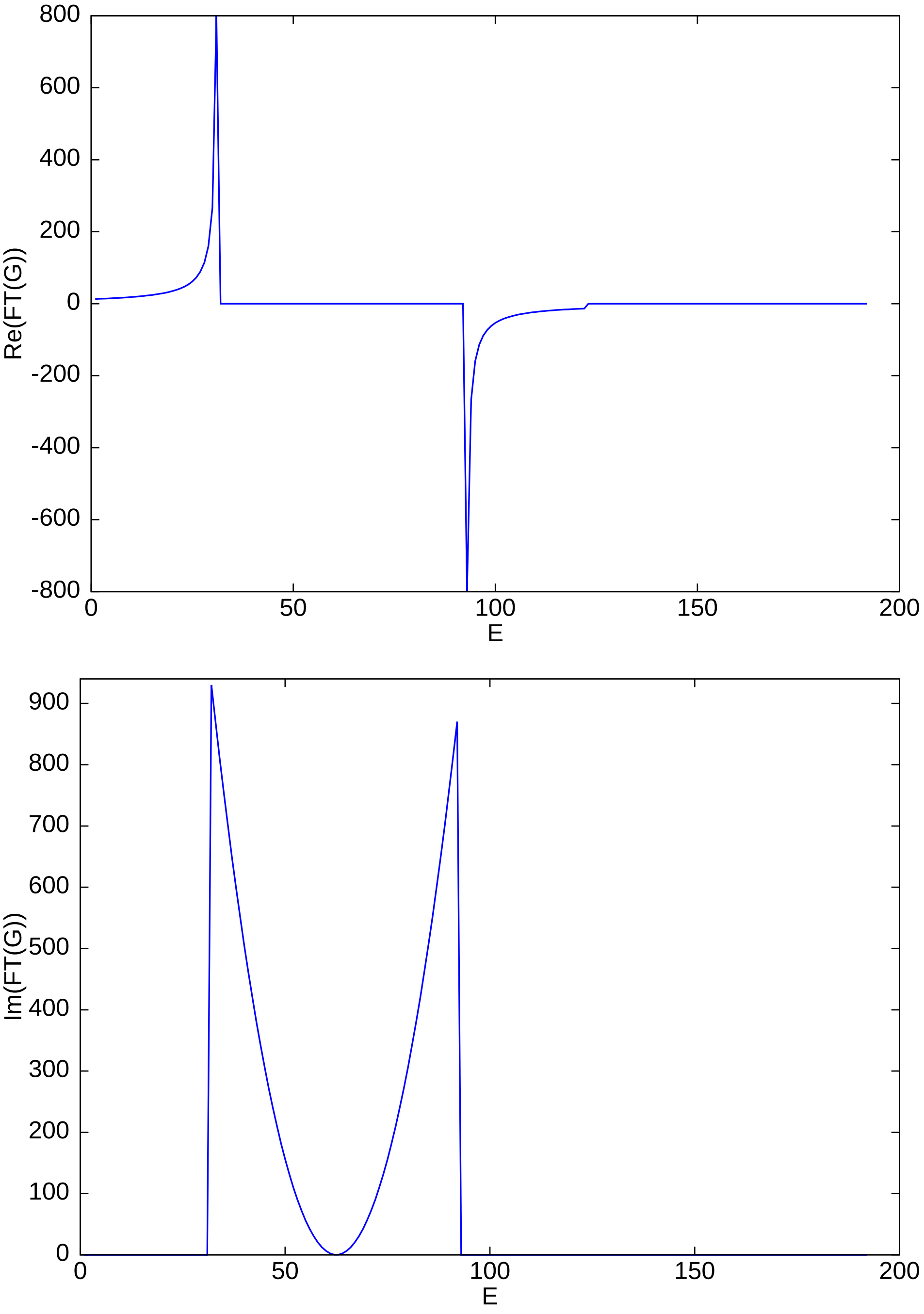

Figure 9.1: Real and imaginary part of the example signal.

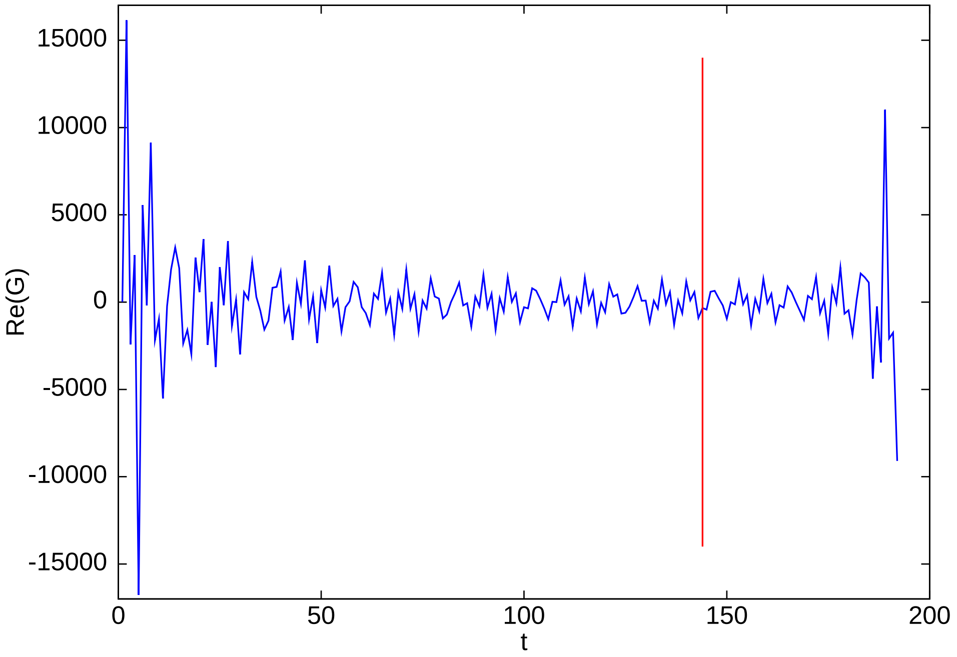

Figure 9.2: Real part of the inverse Fourier transform of the signal in Fig. 9.1. The red line denotes the artificial cut-off.

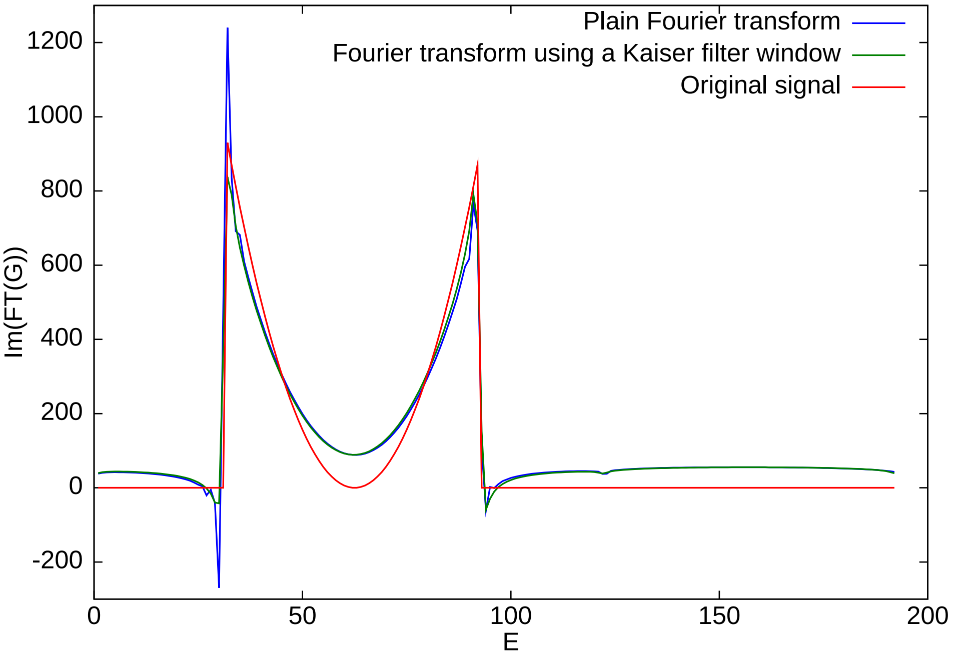

Figure 9.3: Fourier transform of signal shown in Fig. 9.2. The Fourier transform of the full signal, the truncated signal and the truncated signal multiplied with a Kaiser filter function are as indicated in the legend.

9.4 Implementation Issues

It should also be noted that all the methods described above need to be able to handle operators that change quantum numbers. While this is obviously no problem from an analytical point of view, it leads to technical complications in the DMRG. As we have already pointed out in Chapter 6, to keep the size of the Hilbert space we are dealing with as small as possible we have restricted our Hilbert space to a certain set of quantum numbers. If we now were to apply an operator that changes quantum numbers to a state within this Hilbert space, the resulting state would not be within that set of quantum numbers any more. Therefore, before being able to apply such an operator one has to build a new superblock with a new basis suitable to represent states with this new set of quantum numbers. While this is somewhat difficult from a programming point of view, it contains no notable pitfalls from a physical point of view and will therefore not be discussed here any further.

Part III

Results

In modern physics, there exists a wide variety of materials that are quasi-one-dimensional in first approximation and therefore exhibit features that can only be explained by treating them as such. Some more widely known examples of such materials are metal atoms that are aligned in a chain [63], carbon-based systems, typically referred to as carbon nanotubes and carbon nanowires [64], charged crystalline compounds that consist of differently charged chains separating one from another (e.g., K_2PtS_2 or $CaNiN$) [65] as well as organic charge transfer salts (e.g., $TTF - TCNQ$) [66]. All of these materials have in common that they behave as one-dimensional systems up to certain excitation energies. However, most of them exhibit properties that cannot be completely described within the framework of a Luttinger-liquid (see Sec. 3.1). Instead, one also needs to take the full interactions in the system into account. Therefore, the Hubbard model and its extensions described in chapter 2 are comparatively good models for describing these quasi-one-dimensional materials and already exhibit most of the properties stemming from the full electron-electron interaction.

In this part of the thesis, we will apply the majority of the methods that have been described in Part II and that have partially been implemented as part of this thesis, to the Hubbard (2.4) and to the extended Hubbard model (2.8). First, we will consider a test case for which the phase diagram and the spectral function have been calculated previously using a different method [1] to demonstrate that the methods proposed here yield correct results. In the next chapter, we will use the different measures of quantum entropy described in Sec. 4.1 to establish a consistent picture of the different phases and of the order of the phase transitions in the extended Hubbard model. We will also point out why some other measures fail at the same task. Finally, we will use time evolution and subsequent Fourier transformation, as described in Chapter 8 and 9, to calculate the spectral function and the density of states for the extended Hubbard model starting from previously known results and exploring the changes in the aforementioned functions over a broad spectrum of parameters and encompassing various phase transitions. The calculation of spectral functions is especially important because it is possible to measure them via angle-resolved photoemission spectroscopy (ARPES) [67], thereby enabling comparison between theory and experiment.

Chapter 10

Tests

In 2007, E. Jeckelmann and H. Benthien published results for the spectral function of the half-filled Hubbard and for the extended Hubbard model in the limit $V \ll U$ using the DDMRG method [1] described in Sec. 9.2. Since the DDMRG is a method based on an entirely different algorithm than the time evolution algorithm used in this thesis, it is well suited for a comparison. As part of the above mentioned article, the angle-resolved spectral function of the Hubbard model (2.4) at $U/t = 7.74$ was calculated. In the following, we will compare these calculations with our own in oder to investigate the validity of the newly developed method. We will only conduct a qualitative comparison because a quantitative comparison would not be able to clarify if the measured error stems from the DDMRG calculations or from the calculations conducted in this thesis. A direct comparison with analytical results is not possible here, because such results only exist for the cases $U = 0$ and $U \to \infty$. Neither of these cases can be calculated within the DMRG for numerical reasons.

In Fig. 10.1 we show a density plot of the spectral function for the Hubbard model at $U/t = 7.74$ obtained in Ref. [1] and the same plot obtained by the time evolution method described in Chapter 9. It can be seen that all the important features are clearly visible. Most of the weight is in the spinon and in the first holon branch, denoted S and H, respectively, in the upper image of Fig. 10.1; the other two holon branches H' and H'' are also clearly visible in the lower image. The discrepancy in the energy axis is due

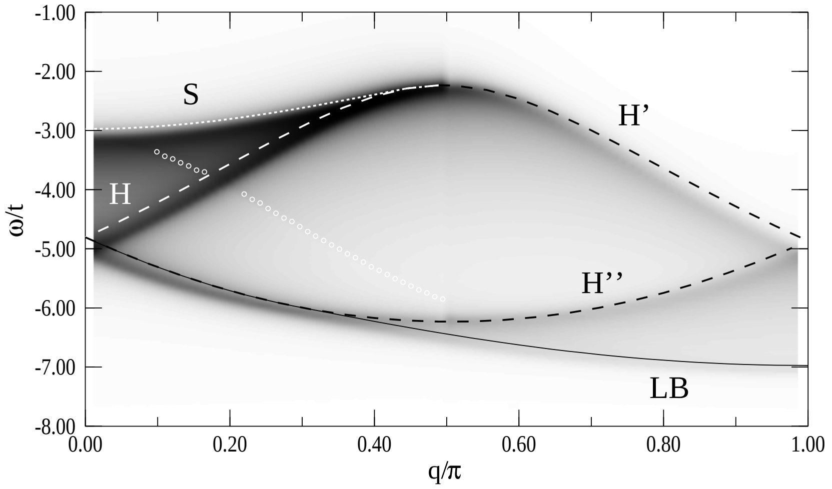

(a)

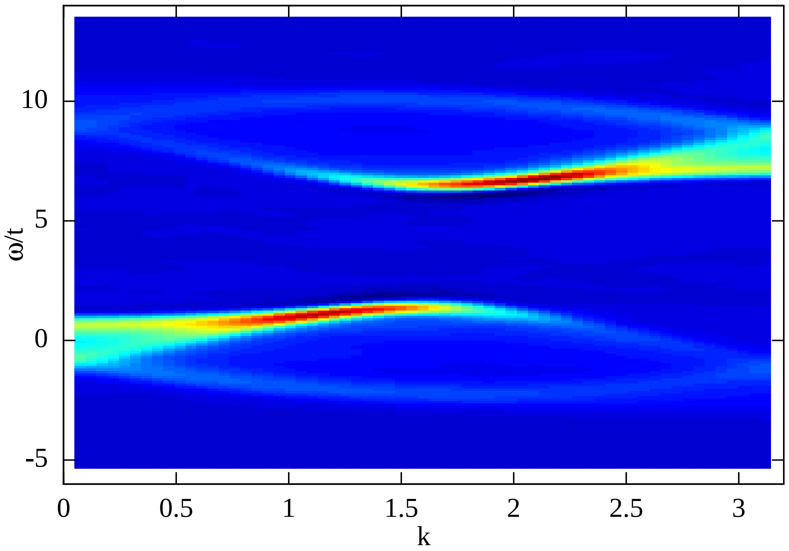

(b)

Figure 10.1: Angle-resolved spectral function of the Hubbard model for $U/t = 7.74$. (a) Results from Jeckelmann et al. [1] and (b) results obtained in this thesis.

to the different formulations of the Hamiltonian. In Jeckelmann's article [1]

$$\begin{aligned} H_{\mathrm{Hub}} = -t \sum_{i=1}^{N-1} \sum_{\sigma=\uparrow,\downarrow} \left(c^\dagger_{i+1,\sigma} c_{i,\sigma} + c^\dagger_{i,\sigma} c_{i+1,\sigma} \right) \\ +U \sum_{i=1}^{N-1} \left(n_{i,\uparrow} - \frac{1}{2} \right) \left(n_{i,\downarrow} - \frac{1}{2} \right) , \end{aligned} \tag{10.1}$$

whereas in our calculation (2.4) was used as the Hamiltonian, thereby shifting the energy spectrum up by $U/2$.

Both the upper and the lower Hubbard band are shown in the lower image in Fig. 10.1. This leads to another consistency check as follows. We have shown in Sec. 2.2 that the half-filled Hubbard model (2.4) is particle-hole symmetric. Therefore, we know that the density of states must be symmetric around $U/2t = 3.87$. That this is actually the case can be seen in Fig. 10.2. In fact, the main source of asymmetries in this figure are discretization effects.

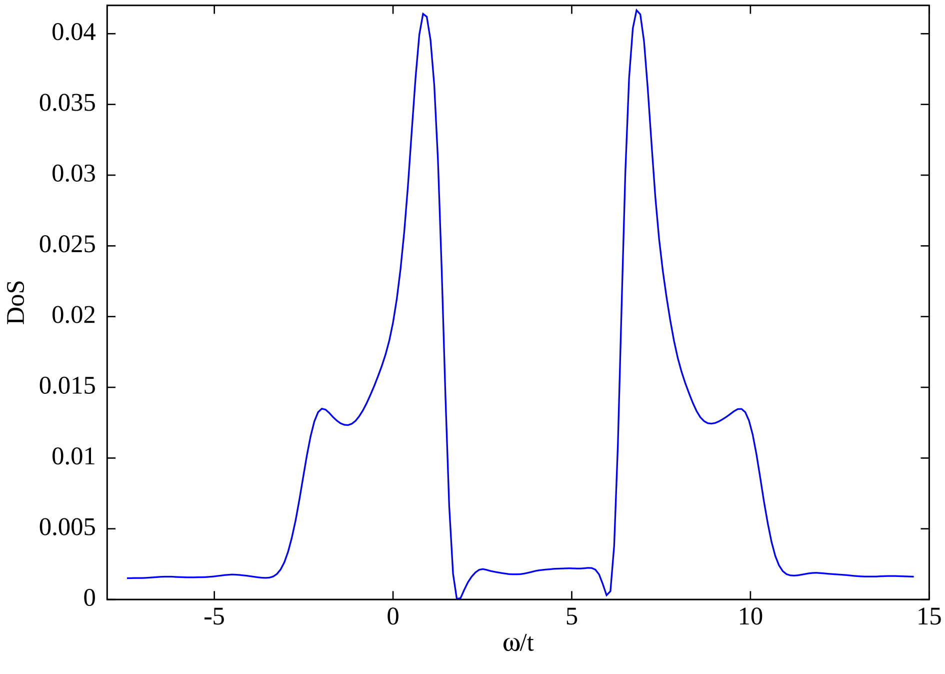

Figure 10.2: The density of states for the half-filled Hubbard model with $U/t = 7.74$.

Chapter 11

Phases in the Extended Hubbard Model

In this chapter, we present results for the phase diagram of the extended Hubbard model, which has been the subject of a few recent studies [14, 2, 16, 68]. These results have been obtained using quantum entropy measurements, which have been described in Sec. 4.1. With the help of these measurements, we are able to determine the phase boundaries as well as, to some degree, the order of the phase transitions. We first consider the behavior of the two-site and block entropies. In order to map out the phase boundaries, we sweep over a grid of different values for U and V in the extended Hubbard Hamiltonian (2.8). Since the phase transitions are expected to lie around $U = 2V$, we choose to sweep V from $V/t = 2$ to $V/t = 5.5$ in steps of 0.5 for a number of values of U/t to pass through the phase transition lines in a direction which is closer to perpendicular.

11.1 Computational Details

The DMRG calculations used to obtain the following results have been carried out using the finite-system algorithm [4, 5, 3] on systems with open boundary conditions with the number of lattice sites N ranging from $N = 32$ to $N = 512$. Open rather than periodic boundary conditions have been used for two reasons: First, as we already pointed out in Chapter 6, the DMRG is substantially more accurate for open boundary conditions for a given computational effort. Second, since open boundary conditions explicitly break the translational invariance, a corresponding spontaneously broken symmetry of the ground state, which, strictly speaking, can only occur in the thermodynamic limit, appears in the entropy profiles of finite-sized systems [69, 70].

This is, for example, the case for the BOW phase.

Since only ground-state properties are required to calculate the Von Neumann entropies, we need only calculate the ground-state wave function and the appropriate observables for the half-filled system. We have used dynamic block-state selection (DBSS), which chooses the size of the Hilbert space retained in each truncation by keeping the block entropy of the discarded density-matrix eigenstates constant [71]. It is important to do this because the accuracy of the Von Neumann entropy as calculated using the approximate DMRG wave function in Eq. (4.5) is directly related to the entropy threshold used. In our calculations we have used a threshold for the quantum information loss of $\chi < 10^{-10}$, which yields extremely precise results and requires a maximum of approximately $m = 3000$ block states to be retained. In general, we estimate that the errors due to the truncation in the DMRG calculations are negligible in comparison to the uncertainties arising from the finite-size scaling.

11.2 Entropy Profiles

For all sweeps, we find that two peaks develop in both the two-site entropy, Fig. 11.1, and in the block entropy, Fig. 11.2, for sufficiently large systems. Note that the second peak in the block entropy can only be seen at system sizes of $N = 96$ and larger. This slow size dependence might be the reason why this phase was not seen by Deng *et. al.* [16].

We interpret the peak at lower U as marking the CDW-BOW phase transition at the corresponding system size, and the peak at larger U as indicating the BOW-SDW phase transition. The differing shapes of the two peaks are consistent with the picture that the CDW-BOW transition is first order in this parameter regime [2], while the BOW-SDW transition shows characteristics of an infinite-order transition.

The interpretation that the intervening phase is a BOW phase is supported by the behavior of the two-site entropy for two adjacent sites (odd and even bonds) in the center of the lattice, plotted for the largest system size, $N = 512$, in Fig. 11.1. The dimerization entropy is given by $D_s = S_{N/2+1}(2) - S_{N/2}(2)$, which is the difference between the two $N = 512$ curves. It is clear that this difference reaches a marked maximum between the two peaks associated with the phase transitions. Finite-size extrapolation (not shown) indicates that D_s remains finite in the thermodynamic limit in the intermediate phase.

The positions of the two peaks in the two-site or block entropy can then be extrapolated to the thermodynamic limit. While the functional form

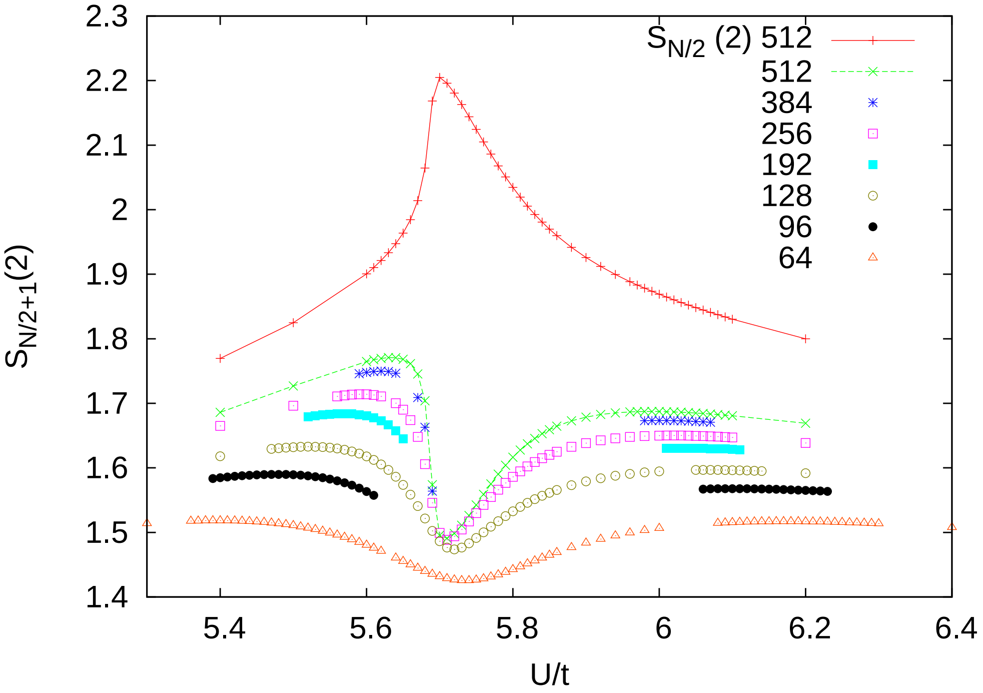

Figure 11.1: Two-site entropy $S_{N/2+1}(2)$ for $V/t = 3$, plotted as a function of U/t. System sizes range from $N = 64$ to $N = 512$ sites.

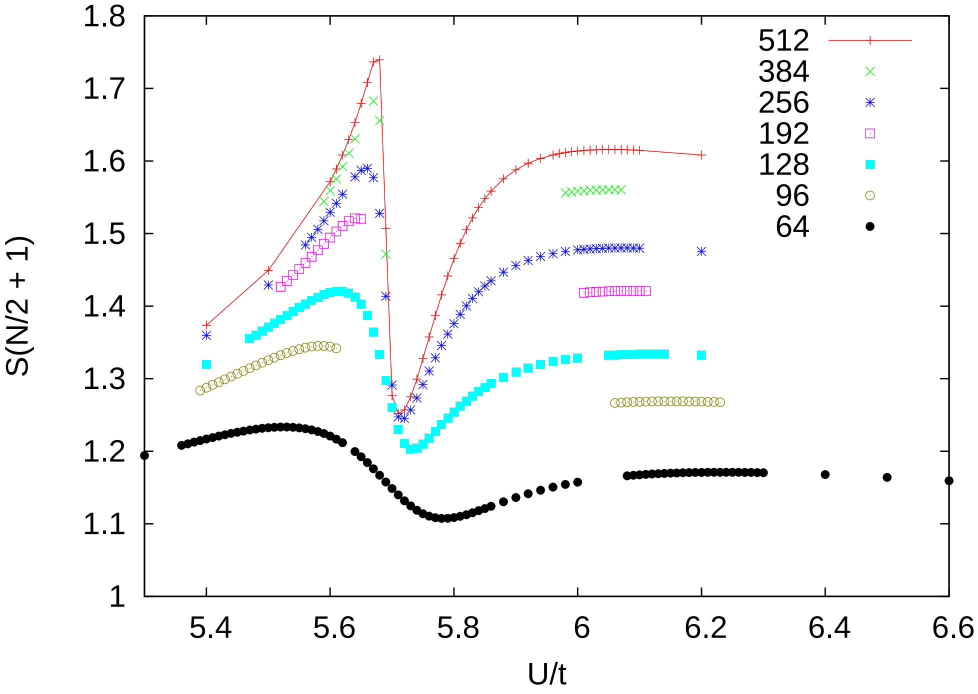

Figure 11.2: Block entropy at the center of the chain $S(N/2+1)$ for $V/t = 3$ and system sizes from $N = 64$ to $N = 512$ sites.

of this extrapolation is not exactly known, using a fourth-order polynomial yields stable results, with a rapid falloff in coefficient size for higher orders. Therefore, the behavior is predominantly linear. This can be seen in Fig. 11.3.

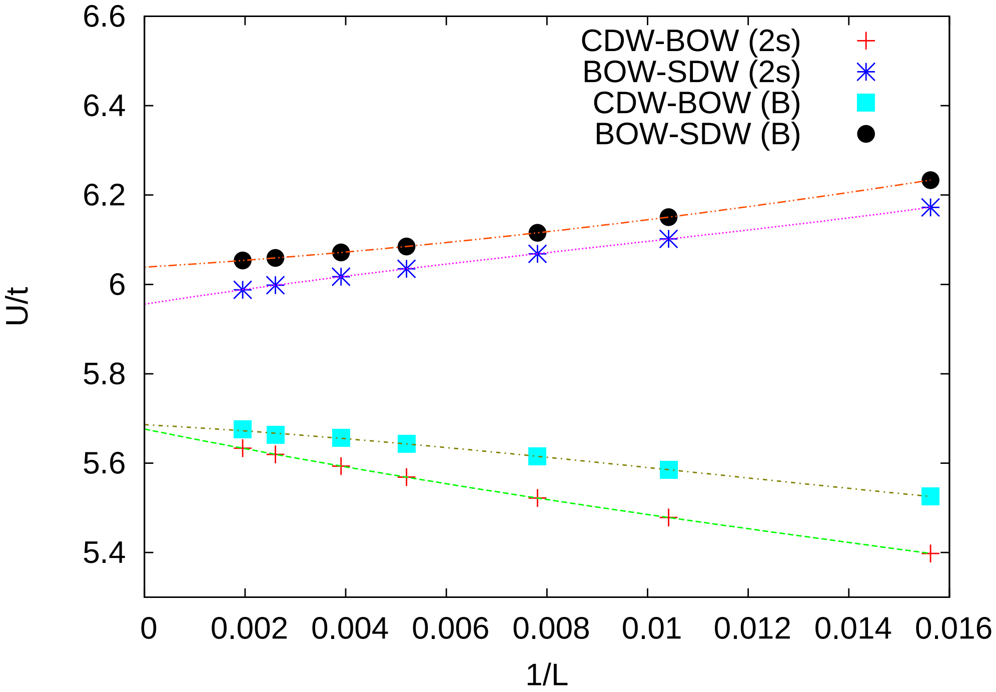

Figure 11.3: Finite-size extrapolation of the peaks in Figs. 11.1 and 11.2 to the thermodynamic limit, $1/L \to 0$, using fourth order polynomials in $1/L$. "2s" labels the two-site entropy and "B" the block entropy.

11.3 The CDW-BOW Transition

A comparison of Figs. 11.1 and 11.2 clearly shows that the peaks in the block entropy at lower U are sharper and higher than those in the two-site entropy. In addition, the position of the peaks in the block entropy match the jump in the one-site entropy (see Fig. 11.4) better than the position of the peak in the two-site entropy. Therefore, we conclude that the block entropy is, in general, a better indicator for the position of the CDW-BOW transition than the two-site entropy. As can be seen in Fig. 11.3, the fits to the two-site and the block entropies (the two lower curves) match almost exactly in the thermodynamic limit, so that this issue is virtually irrelevant here.

A more difficult issue is to determine where nature of the CDW-BOW transition changes from first-order to continuous. This can best be investigated using the finite-size extrapolation of the one-site entropy. In Fig. 11.4, we show the one-site entropy extrapolated to the thermodynamic limit using a polynomial of cubic order. It is apparent that the entropy has a jump at the transition point when $V/t \geq 4$, a clear indication of a first-order transition. At approximately $V/t = 3$, the transition is close to becoming continuous in that a jump is no longer present. For smaller values of V/t (not shown), it is clearly continuous. Therefore, we conclude that the first-order-to-continuous bi-critical point must occur somewhere near, but below $V/t = 3$. Note that it is difficult to determine the location of this point with more accuracy because one would have to determine whether or not an increasingly small jump is present in the finite-size extrapolated data as the bi-critical point is approached on a sufficiently finite grid.

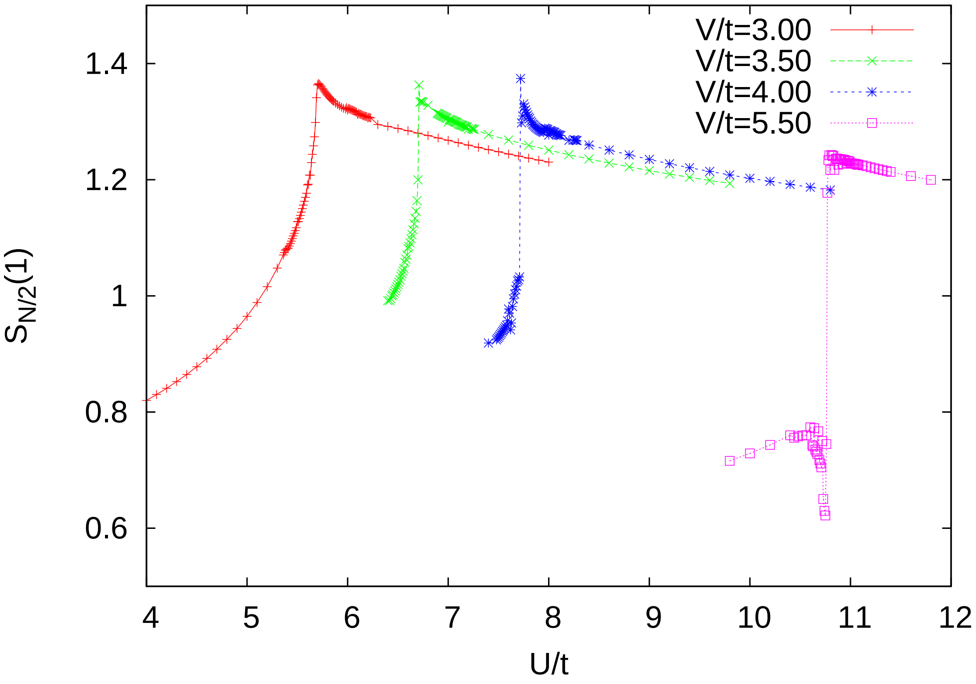

Figure 11.4: Extrapolated one-site entropy $S_{N/2}(1)$ plotted as a function of U/t for various values of V/t.

11.4 The BOW-SDW Transition

The BOW-SDW transition is believed to be infinite-order [21] and is therefore much harder to characterize. While we were able to obtain a fairly good estimate for the position of the CDW-BOW transition just by examining the bond order parameter, this is not possible for the BOW-SDW transition, as will be discussed in Sec. 11.5. It can be seen in Figs. 11.1 and 11.2 that the maxima corresponding to the BOW-SDW transition (the peaks at higher U/t) are much broader. Therefore, small errors in the numerical calculations would have a bigger influence on the result than for the case of the CDW-BOW transition.

Results for the phase boundaries are shown in Fig. 11.5, plotted in the tilted V-U phase, i.e., with axes $2V/U$ and U, so that the transition region is discernible. Included are data from Ref. [2] in which the phase boundaries were determined from the spin and charge exponents calculated using QMC methods. There is generally very good agreement for the location of the CDW-BOW transition, with some deviation of the results from the two-site entropy at smaller U/t values. As we have argued above, the block entropy is a better indicator of the position of this transition because the peak is better developed and grows more rapidly with system size.

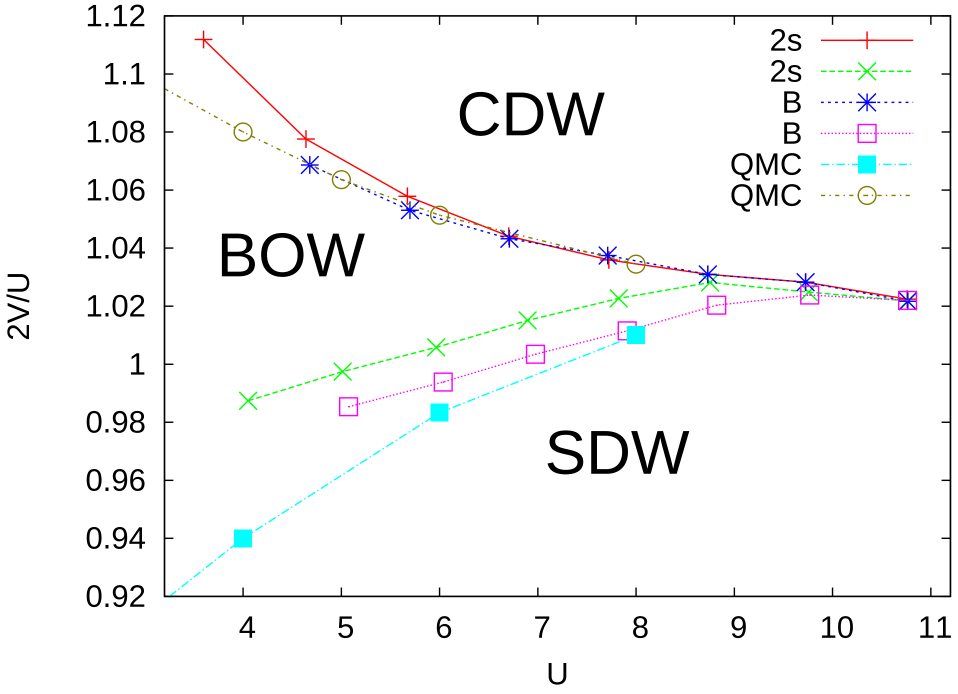

Figure 11.5: The phase diagram in the tilted U-V-plane, showing phase boundaries determined using the two-site entropy (2s), the block entropy (B), and including results from Ref. [2], determined from QMC calculations.

For the BOW-SDW transition, the two-site and the block entropies coincide perfectly upon scaling for higher U and V values, where only a first-order transition is present, as can be seen in Fig. 11.5. However, there is a discrepancy in the position of the peaks in the infinite-system extrapolations of the two-site and the block entropies (see Fig. 11.3) for smaller values of U and V. This occurs for the entire range of parameter values in which a BOW phase and, therefore, an infinite-order transition is present. This is probably partially due to uncertainty in localizing the broad peak in the entropies corresponding to the BOW-SDW transition. In addition, due to the strong increase of the block entropy with system size below $U/t \approx 4$, we cannot treat systems of more than a few hundred lattice sites for fixed $\chi = 10^{-10}$, leading to increased uncertainty in the finite-size extrapolation. For $U/t < 3$, the second peak in the entropy functions develop only for $N \geq 96$, quite severely limiting the extrapolation to infinite system size. We therefore display the phase diagram only for $U/t > 3$ in Fig. 11.5

11.5 Bond-Order-Parameter Results

One could argue that using the bond order parameter (2.12) to determine the extent of the bond-ordered phase would be the most straightforward way and should be used. Whether the bond order parameter is finite or vanishing in the thermodynamic limit would determine whether a given point in parameter space is bond ordered or not, and a grid of such points can be used to determine the phase boundaries. Unfortunately, there are two major problems with this strategy. First, the transition between the BOW and SDW phases is expected to be infinite-order, and we indeed find behavior characteristic of an infinite-order transition. This means that the extrapolated bond order parameter tends to zero exponentially as the BOW-to-SDW transition is approached. Second, while it is know that the bond order parameter is linear in $1/N$ in the CDW phase and proportional to $1/\sqrt{N}$ in the SDW phase, the analytic form of the finite-size scaling in the BOW phase is not known and changes nature as the transition is approached.

To investigate whether the bond order parameter is a suitable measure for determining the extension of the BOW, we have carried out calculations to very high precision. The resulting data is sufficiently accurate so that it can be regarded as essentially exact for a particular system size for fitting purposes. We have carried out the extrapolation to the infinite-system limit by fitting to three different functions: a polynomial in $1/N$, a polynomial in $1/\sqrt{N}$, and a power law of the form $1/N^{\alpha}$. The extrapolated data is shown in Fig. 11.6. In the CDW phase, to the left of the transition indicated by vertical lines, the fit to a polynomial in $1/N$ gives the best result, yielding the expected value, zero, to the best accuracy. In the SDW phase, for $U/t \gtrsim 8$, the polynomial fit in $1/\sqrt{N}$ and the fit to a power law work better, yielding the expected value of zero to within reasonable accuracy. This is indicative of a scaling whose dominant term falls off more slowly than $1/N$. In the intermediate region, i.e., in the BOW phase, the results differ significantly, with both the fit to powers of $1/\sqrt{N}$ and the power-law fit extrapolating to spurious negative values. In addition, the power-law fit is clearly unstable in the BOW region. While the fit to a polynomial in $1/N$ seems to be more stable, it clearly overestimates the bond order parameter significantly in both the SDW phase and in most of the BOW region. Therefore, we conclude

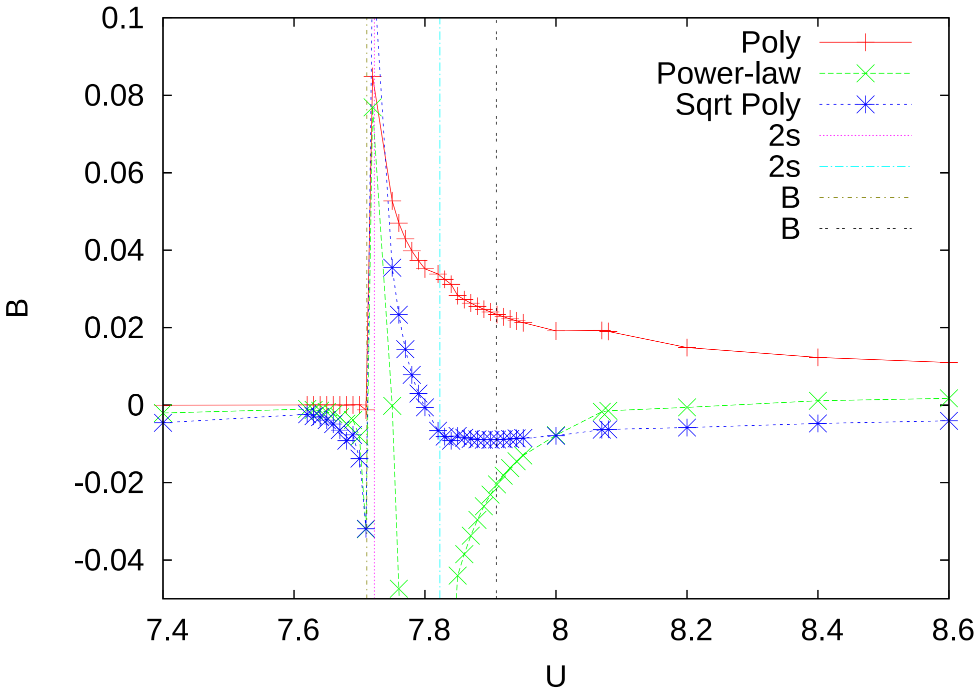

Figure 11.6: Bond order parameter B extrapolated to the thermodynamic limit using fits to three different functions: fit to a third-order polynomial in $1/N$ (Poly), fit to a third-order polynomial in $1/\sqrt{N}$ (Sqrt Poly), and fit to a power law $1/N^{\alpha}$ (Power-law) with α a fitting parameter, plotted as a function of U/t. The vertical lines indicate the transition point determined using the two-site entropy (2s) and the block entropy (B).

that the behavior of the bond order parameter can be used to confirm the position of the CDW-BOW phase transition but is notoriously unreliable for determining the location of the BOW-SDW phase transition. [14, 2]

11.6 Phase Diagram and Discussion

We now summarize the current state of knowledge of the phase diagram of the half-filled extended Hubbard model and discuss open issues and uncertainties. The overall phase diagram is relatively well understood; our results are depicted in Fig. 11.7. The presence of the SDW phase at $2V \ll U$ and the CDW phase at $2V \gg U$ have been long understood, as well as the fact that the transition occurs at $2V \approx U$. The picture of there being a single first-order transition line at strong U and V [72] is also well-established. Our work lends support to a picture in which an intermediate BOW phase is present between the CDW and SDW phases for intermediate to small U and V; our results indicate that this phase is present for $V/t \lesssim 5$. At this point, we find that the first-order CDW-SDW transition line bifurcates into a first-order CDW-BOW transition line and an infinite-order BOW-SDW transition line. The CDW-BOW transition line remains first-order at a bi-critical point at somewhat smaller V/t, below which it becomes continuous, presumably second-order. These results are in reasonable agreement with the results of Refs. [2] and [14]. We therefore regard these features of the phase diagram as being well-established.

We now discuss details of the phase transition more quantitatively. As we have seen in Fig. 11.5, there is not much uncertainty in the position of the CDW-BOW phase transition. The remaining interesting question for this transition is the location of the bi-critical point, i.e., exactly where the phase-transition line goes from being first-order to being continuous (presumably second-order). However, as we have pointed out in Sec. 11.3, entropy measurements can only roughly determine that this point occurs at around $V/t = 3$ and are not an ideal measurement to locate it more accurately. While other authors have obtained putatively more accurate values for the location of this bi-critical point [14, 2], we point out that the inaccuracies in the method used here reflect intrinsic limitations of the numerical methods, which stem both from the DMRG truncation error as well as from the limitations of working with finite systems.

The exact position of the BOW-SDW phase-transition line is also somewhat uncertain. There is a small but significant discrepancy in our calculations between the values obtained from the two-site-entropy and those obtained from the block-entropy; however, both of these extrapolated values seem to converge smoothly to the same line at the tri-critical point. The most likely explanation for the discrepancy in the extrapolations lies in the finite-size extrapolation, i.e., more precise results could be obtained if larger system sizes could be treated. The deviations between the two values for the transition line can be taken as a rough estimate of the uncertainty in the position of the line. In addition, both of these values deviate from those of Ref. [2] (see Fig. 11.5), a deviation to larger values of V, i.e., to a narrower BOW phase, in both cases.

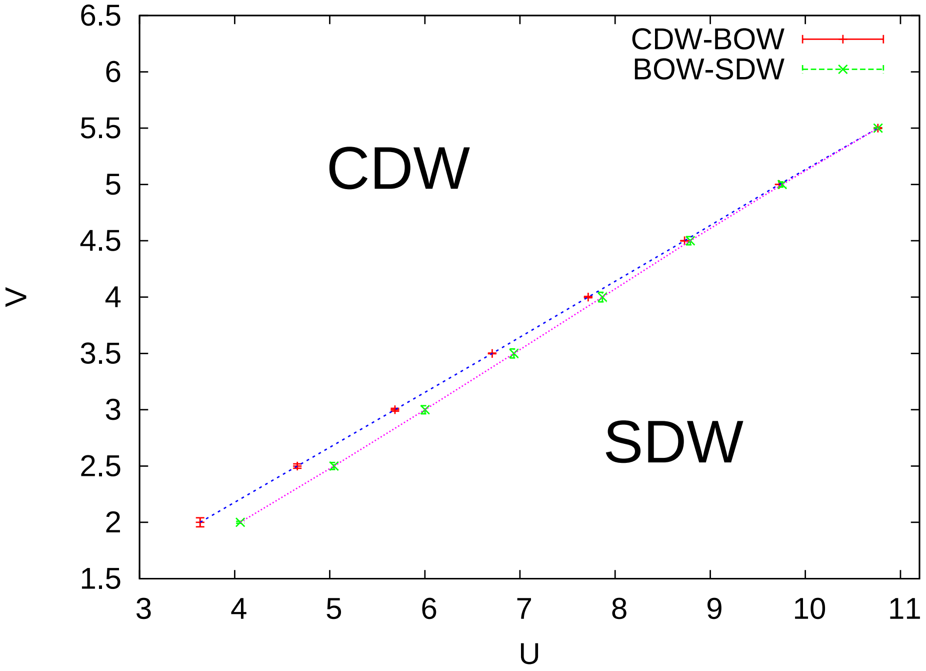

Figure 11.7: The phase diagram in the U-V-Plane obtained from our calculations. On this scale, uncertainties in the position of the transition lines are smaller or about the size of the symbols. The phase in the narrow region between the two transition lines is BOW.

In summary, the DMRG method, coupled with the use of single-site, two-site, and block entropies, is a powerful, relatively unbiased method to determine subtle properties of phase diagrams such as that of the extended Hubbard model at half filling. However, the limitations of the numerical results reflect the intrinsic limitations of the method and the problem studied. In particular, three aspects of the phase diagram studied here remain difficult to pin down numerically: the exact position at which the CDW-SDW line bifurcates into CDW-BOW and BOW-SDW transition lines, the position of the bi-critical point at which the CDW-BOW transition goes from first to second order, and the exact position of the infinite-order BOW-SDW transition. In addition, our calculations make clear that quantitative determination of the transition lines become very difficult in the region of small U and V, at least for real space DMRG. In the parameter regions with $U, V \ll t$ momentum space DMRG could be used successfully.

Chapter 12

Spectral Functions and Density of States

In this chapter, we will present one-particle spectral functions and densities of states calculated for the extended Hubbard model (2.8) at different values of U/t and V/t. We will examine the typical features of these spectral functions and densities of states within the SDW and CDW phase and will also give an intuitive explanation for the most important features. We will also closely examine the transition region between the two phases, which exhibits a BOW phase.

The theoretical calculation of angle resolved spectral functions is especially important since it makes a strong connection to the experimental side of physics. That is, because spectral functions are measured fairly directly in angle resolved photoemission spectroscopy (ARPES) [73, 74], in comparison, for example, to measuring spin-spin correlation functions directly, which is virtually impossible.

12.1 Computational Details

The results in this chapter have been calculated using the finite system algorithm of the DMRG [4, 5, 3] on a 64 site system with open boundary conditions to calculate the ground-state wave function. The time evolution algorithm described in Sec. 8.1 was then applied to calculate the retarded Green's function of the system. Comparably small system sizes and open boundary conditions were used because the time evolution is extremely expensive computationally and therefore treating larger system sizes and/or periodic boundary conditions would not have been feasible. Using smaller systems, on the other hand, would have limited the resolution in energy and momentum significantly. The system sizes were therefore chosen to be as large as possible while still keeping the computational cost reasonable.

The dynamic block state selection (DBSS) scheme, described in chapter 6, was used to carry out the truncation of density-matrix eigenstates. A discarded weight- or entropy-based truncation algorithm is especially advantageous here because it allows for a dynamic increase of block states during the time evolution. This is usually necessary because a perturbation traveling through the system typically increases the correlations between different system parts and, therefore, also increases the number of block states one needs to maintain a given level of accuracy in the calculation. Here a maximum number of $m = 800$ block states were kept during the calculation, limiting the accuracy to roughly $\epsilon = 10^{-5}$ during the time evolution. The time evolution itself was performed in a series of 200 time steps, each of which had a duration of $\Delta t = 0.15$, yielding a total evolution time of $T = 30$. A longer time could not have been chosen, because extending the time evolution to longer times would have introduced strong boundary effects into the results, which would have been undesirable. To approximate $e^{-iH\,\Delta t}$ in every step of the time evolution, 10 Lanczos vectors were used, keeping the error in the time evolution itself of the order of the truncation error or below.

The above mentioned values for the time evolution yield a maximum resolvable energy of $\Omega = \frac{\pi}{\Delta t} \approx 20.94$. This value is large enough to treat the model and the parameter values chosen. The energy resolution obtained is $\Delta\omega = \frac{2\pi}{T} \approx 0.21$. Obviously, a better resolution in energy is always preferable, but as we have already pointed out in Sec. 9.3.2, an increase in energy resolution also increases the computation time tremendously (computation time $\propto \mathcal{O}(\frac{1}{(\Delta\omega)^5})$. Therefore, a reasonable trade-off between computational effort and energy resolution was made.

It also needs to be noted that the following results do not stem from calculations for a perturbation on a single site. Instead, calculations were performed for the four middle sites of the system for each set of parameters and the results were then averaged over these sites, yielding a significant increase in precision, especially for system with a dimerized or otherwise periodic, e.g., incommensurate, ground state.

12.2 The Spin-Density-Wave Phase

The SDW phase shows a periodic modulation in the expectation value of a spin component, e.g., $\langle S_z \rangle$. In the case of the half-filled Hubbard and extended Hubbard model with open boundary conditions the SDW phase is typically commensurate with a periodicity of $2a$, where a is the lattice constant. A simplified depiction of a SDW can be seen in Fig. 12.1.

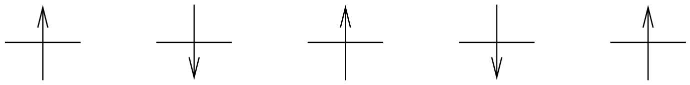

Figure 12.1: A simplified depiction of a SDW.

Within a SDW phase the important features of the spectral function, such as shape and distribution of the energy bands, do not change. This can be seen by a comparison of Fig. 10.1(b) and Fig. 12.2(a). It is important to note, though, that while Fig. 10.1(b) depicts the spectral function of the Hubbard model (2.4) at $U/t = 7.74$, Fig. 12.2(a) shows the spectral function of the extended Hubbard model (2.8) at $U/t = 8$ and $V/t = 0.5$. We can therefore see that a perturbation of the Hubbard model ground state with a small V, i.e., a weak nearest-neighbour repulsion, does not cause a significant change in the features of the spectral function.

The biggest discernible difference is that the upper and the lower band are both shifted upwards in energy due to the additional V term. It is also notable that, even though the additional V term formally breaks the particle-hole symmetry in the system, the density of states remains in a mostly symmetric shape as long as the system is in a SDW phase, as can be seen in Figs. 12.6-12.9. Only for larger values of V, close to the phase transition, are asymmetries clearly distinguishable, as seen in Fig. 12.9(b). Figs. 12.2-12.5 also clearly show that most of the excitation weight is clustered in the spinon branch and the first holon branch starting at $k = 0$ and extending up to $k = \frac{\pi}{2} = k_F$ in the lower band, whereas most of the excitation weight is between k_F and π in the upper band. This tendency dramatically increases for larger values of V until the two other holon branches, H' and H'', completely disappear close to the phase transition. It can also be seen that the gap shrinks continuously with increasing V until it eventually vanishes right on the transition line to the CDW phase (not shown). This is even clearer in Figs. 12.6-12.9 were the outer peaks, clearly visible in Fig. 12.6, showing the weight in H'' slowly disappear and the charge gap shrinks under $U/t = 3$ in Fig. 12.9(b). These findings are also consistent with the behavior of the charge gap in Ref. [2].

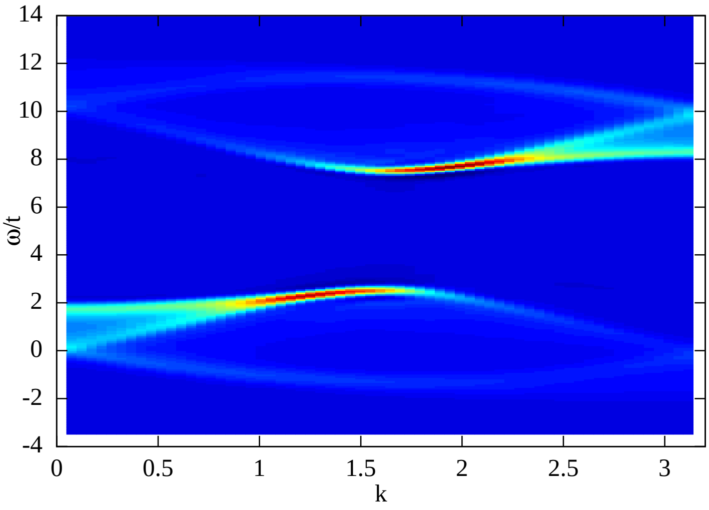

(a) $V = 0.5$

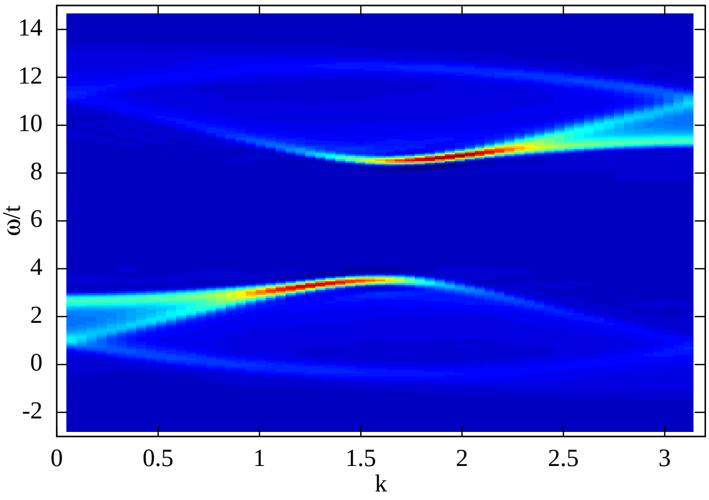

(b) $V/t = 1.0$

Figure 12.2: Angle-resolved spectral function $A(k, \omega)$ of the half-filled extended Hubbard model at $U/t = 8$ and V/t from 0.5 to 1.

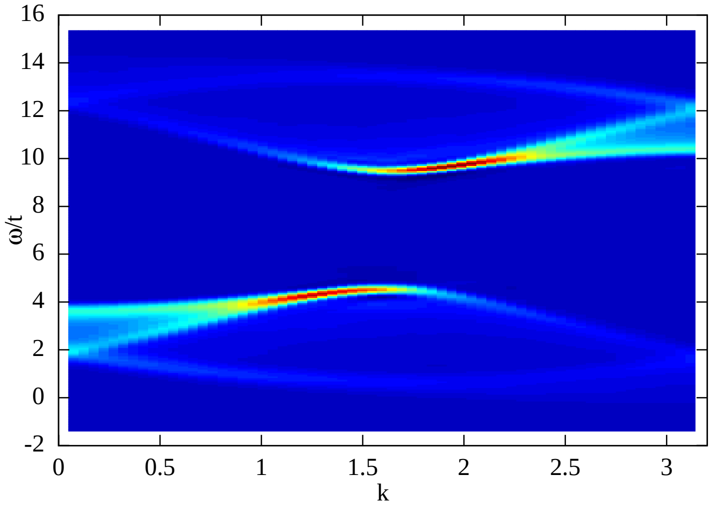

(a) $V/t = 1.5$

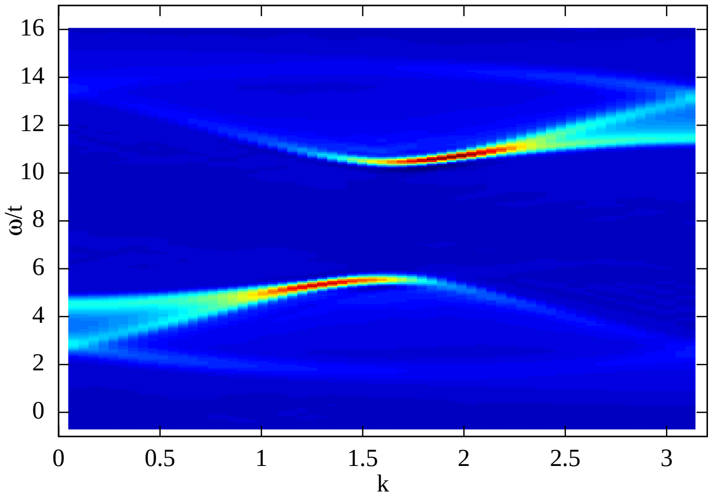

(b) $V/t = 2.0$

Figure 12.3: Angle-resolved spectral function $A(k, \omega)$ of the half-filled extended Hubbard model at $U/t = 8$ and V/t from 1.5 to 2.

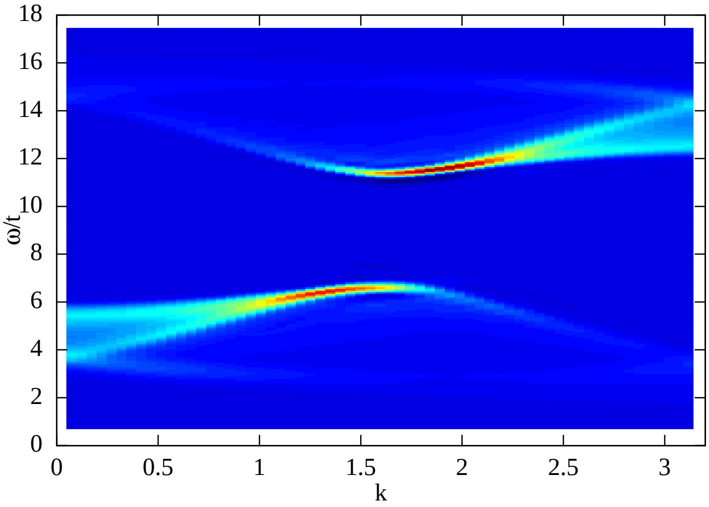

(a) $V/t = 2.5$

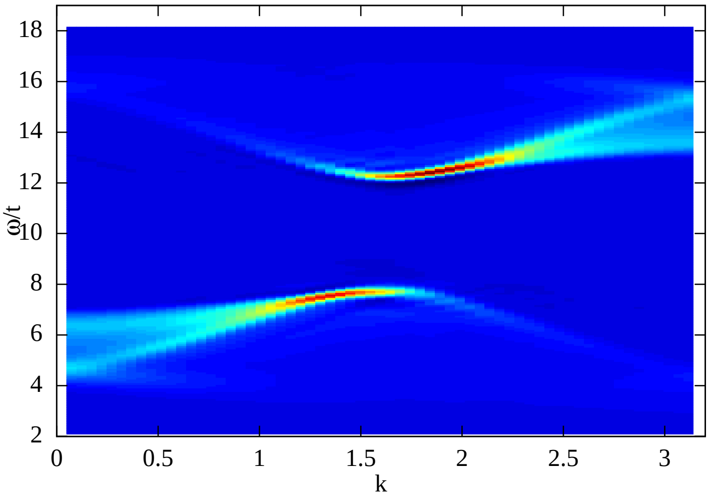

(b) $V/t = 3.0$

Figure 12.4: Angle-resolved spectral function $A(k, \omega)$ of the half-filled extended Hubbard model at $U/t = 8$ and V/t from 2.5 to 3.

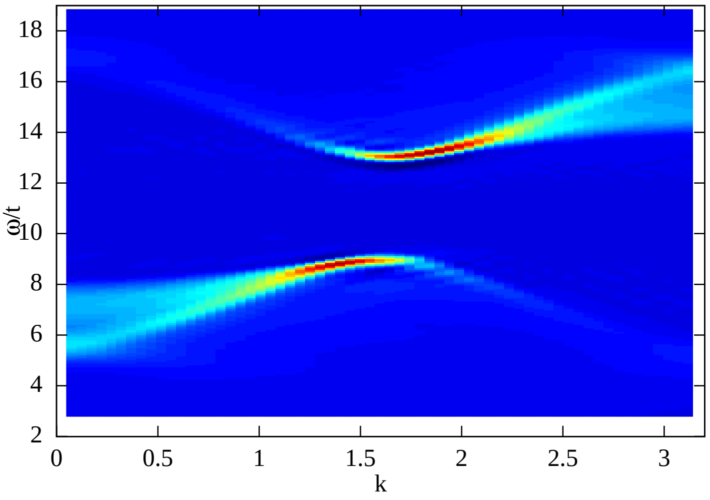

(a) $V/t = 3.5$

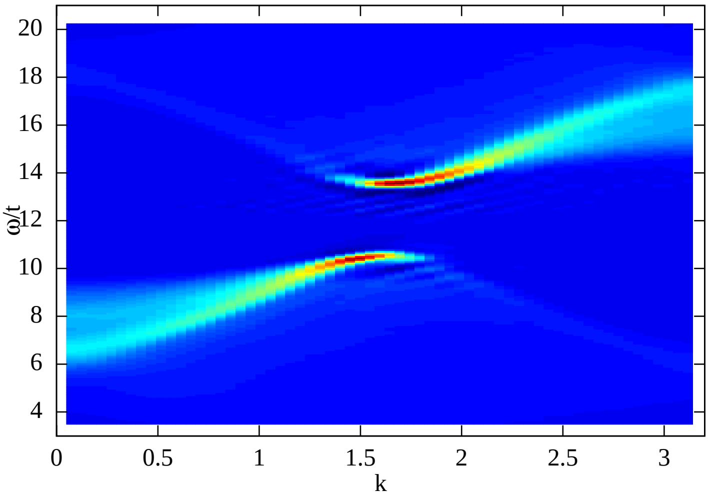

(b) $V/t = 4.0$

Figure 12.5: Angle-resolved spectral function $A(k, \omega)$ of the half-filled extended Hubbard model at $U/t = 8$ and V/t from 3.5 to 4.

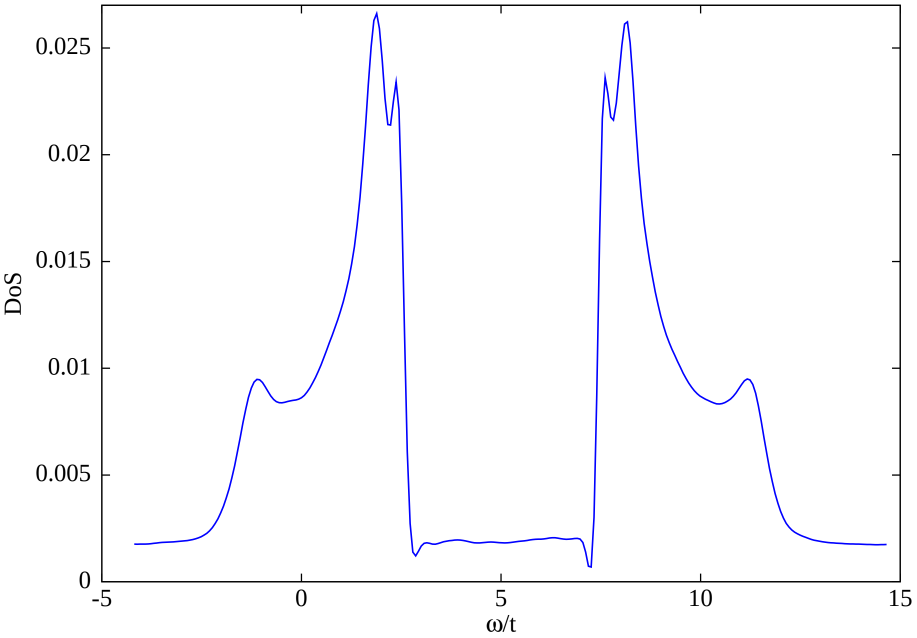

(a) $V = 0.5$

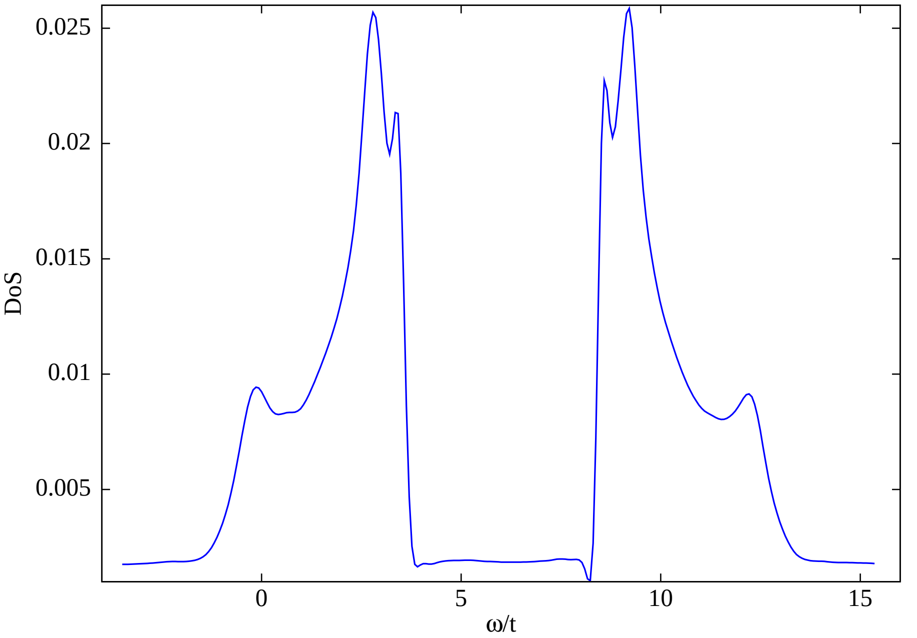

(b) $V/t = 1.0$

Figure 12.6: Density of states $N(\omega)$ of the half-filled extended Hubbard model at $U/t = 8$ and V/t from 0.5 to 1.

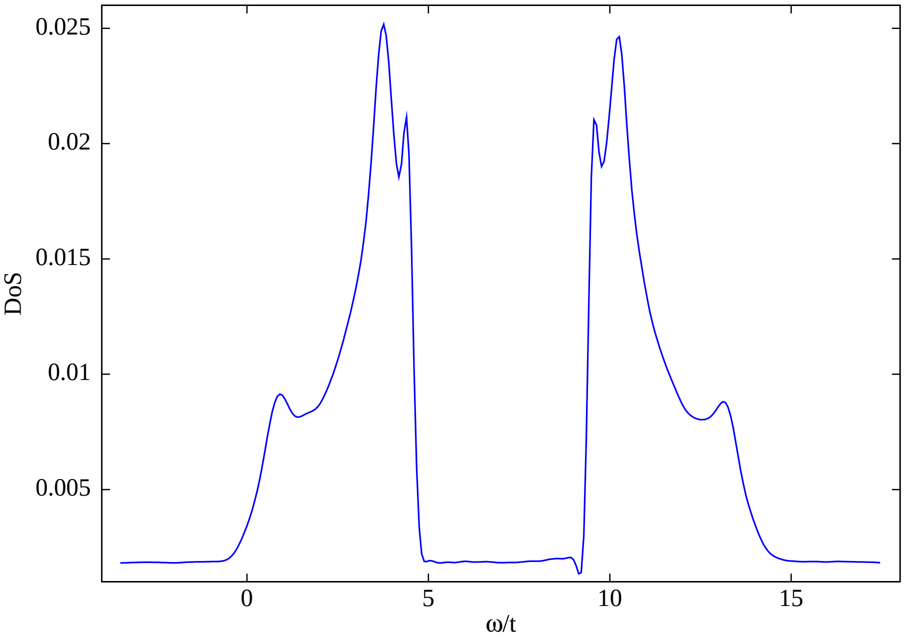

(a) $V/t = 1.5$

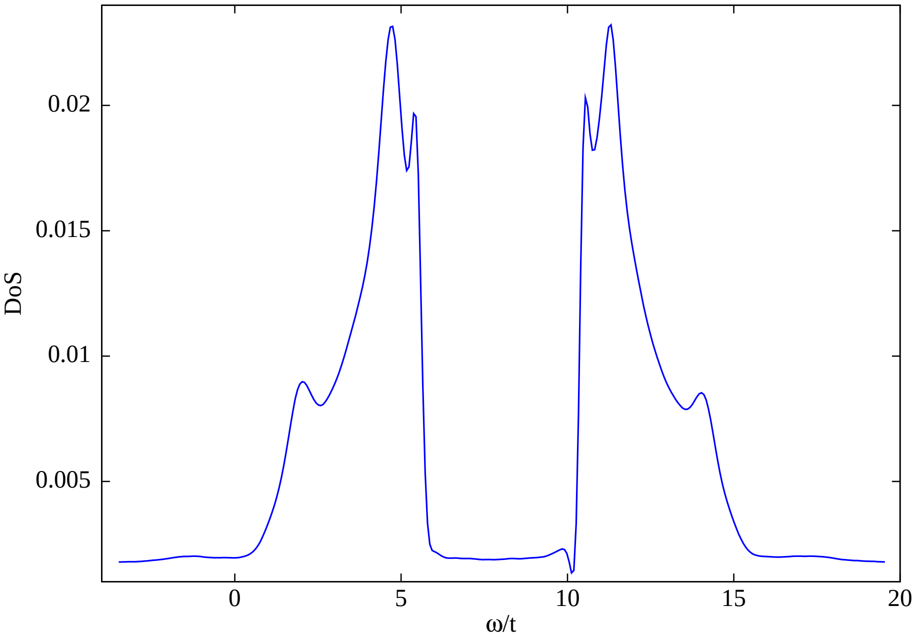

(b) $V/t = 2.0$

Figure 12.7: Density of states $N(\omega)$ of the half-filled extended Hubbard model at $U/t = 8$ and V/t from 1.5 to 2.

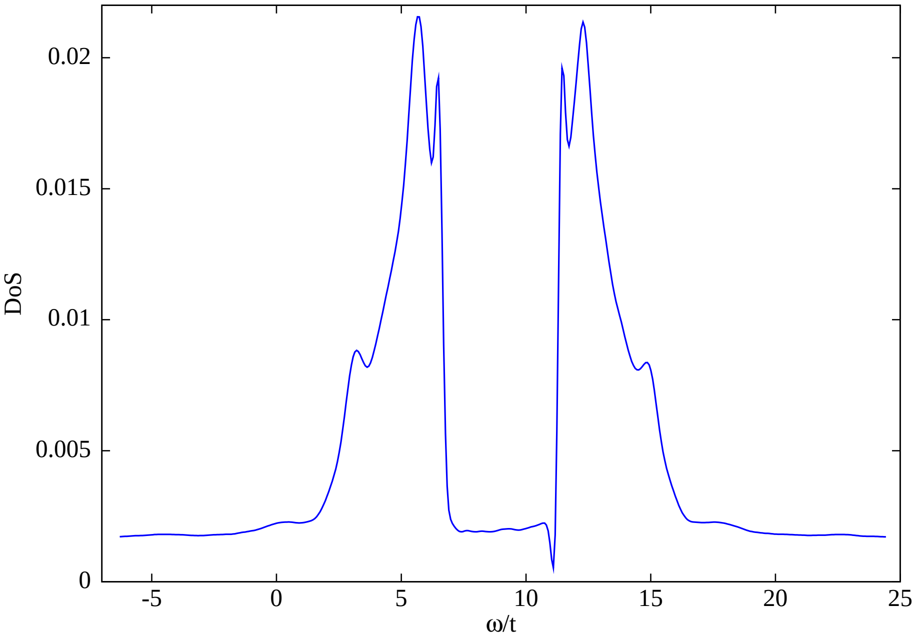

(a) $V/t = 2.5$

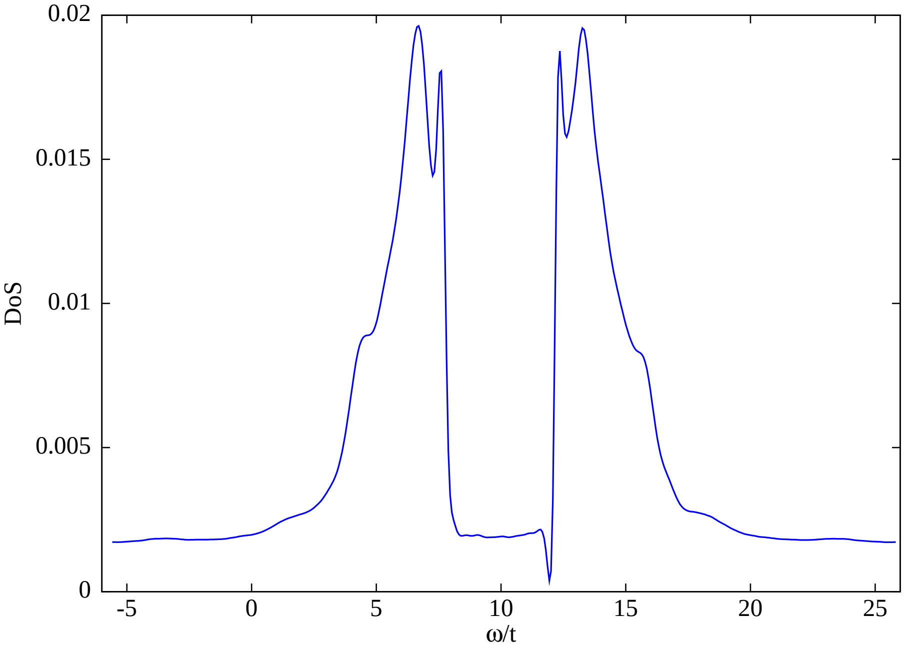

(b) $V/t = 3.0$

Figure 12.8: Density of states $N(\omega)$ of the half-filled extended Hubbard model at $U/t = 8$ and V/t from 2.5 to 3.

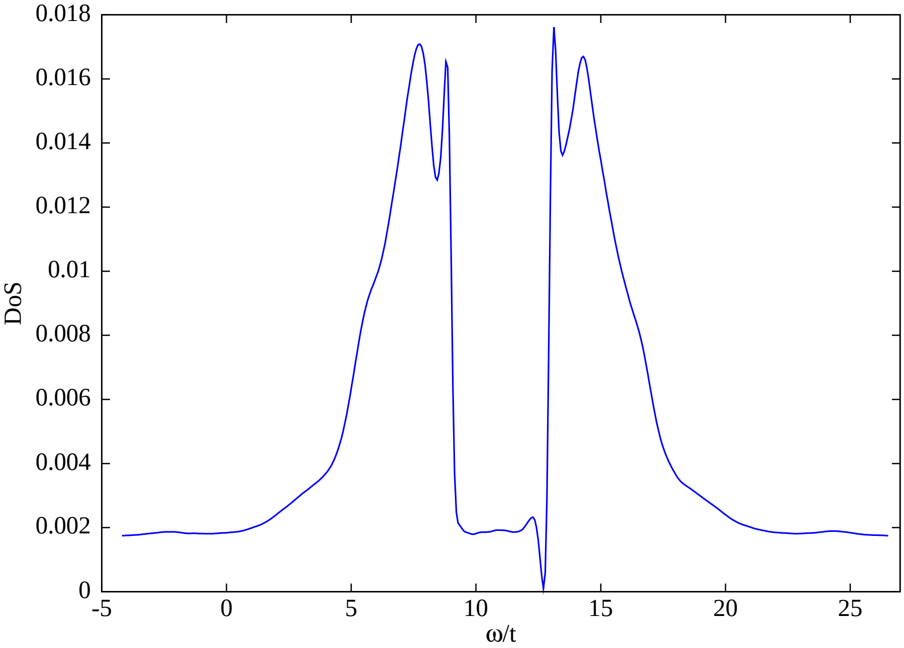

(a) $V/t = 3.5$

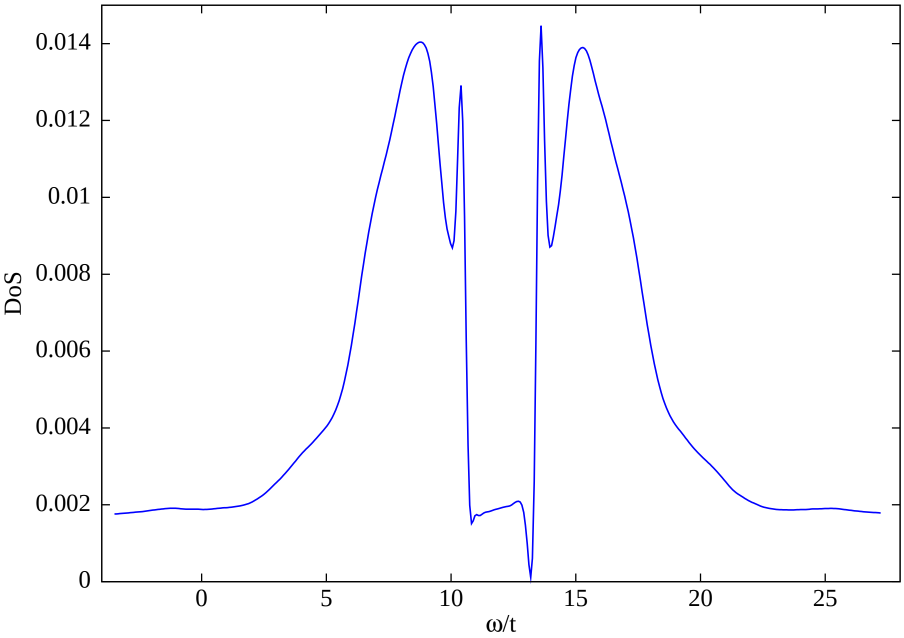

(b) $V/t = 4.0$

Figure 12.9: Density of states $N(\omega)$ of the half-filled extended Hubbard model at $U/t = 8$ and V/t from 3.5 to 4.

12.3 The Charge-Density-Wave Phase

A CDW phase exhibits a modulated pattern in charge density as described in Sec. 2.3.1. In a half-filled extended Hubbard model, the typical modulation frequency is $\frac{1}{2a}$ leading to a wavelength of $2a$, just as in the SDW phase. Fig. 12.10 shows a graphical representation of a typical CDW phase.

In the CDW phase, the spectral function and the density of states are completely different from those in the SDW phase. As can be seen in Figs. 12.14-12.16, there is clearly no sign of symmetry between the upper band and the lower band anymore, and the spectral functions shown in Figs. 12.11-12.13 have a completely different structure. They are dominated by a band of lower excitations that is found at a frequency of roughly U and a band of upper excitations that is centered around a frequency of $4V$. Both of these bands show only a very small dispersion in k. These excitation bands can be easily understood if we consider the atomic limit. If we assume that a CDW phase, as depicted in Fig. 12.10, is present and we insert a particle at one of the empty sites, we have to pay an energy of V for every particle on an adjacent site, hence $4V$. Whereas if we assume that we remove a particle from the state shown in Fig. 12.10, wait for some time, and then force it back onto the same position, we have to pay an amount of energy approximately equal to U. And, in fact, the lower excitation band is the Fourier transform of $G^L_{A^\dagger,A}(\omega)$, see Eq. (9.3), and the upper excitation band is the Fourier transform of $G^U_{A,A^\dagger}(\omega)$, see Eq. (9.2). More interesting are the excitations that appear at frequencies of about $2V$ and $3V$ for $k = \pi/2$ and have a dispersion in such a form that the two bands of excitations meet at $k = \pi$. It would be a very interesting question to investigate if these excitations which seem to be of excitonic nature are due to the finite system size or if they also appear in experimental studies. For other parameter regions, the existence of excitons has already been predicted [75, 76]. Unfortunately, much larger system sizes are not feasible for spectral function calculations with the DMRG because, as we already pointed out in Sec. 9.3.2, the computational cost for spectral functions grows approximately as the fifth power of the time evolution length and, even if the time evolution length is not increased with the system size, the computational cost still grows with the fourth power of the length of

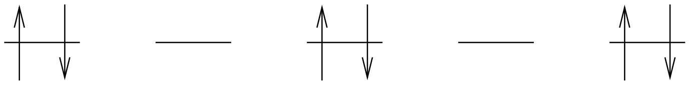

Figure 12.10: Simplified depiction of a CDW phase.

the system because the algorithm for fixed m is linear in the system size, and the required number of states kept m scales approximately with system size. One should also keep in mind that this should in principle not be an issue, because a perturbation of a finite system should approximately have the same effect as on an infinite system as long as the perturbation does not reach the system boundaries in the process of the time evolution. We can also see that, the majority of the weight of the lower band at a frequency of U is between 0 and $k_F = \frac{\pi}{2}$, whereas most of the weight of the bands at $2V$, $3V$ and $4V$ is between k_F and π. It is noteworthy that secondary bands appear above and right below the upper band and also below the lower band for larger values of U. Unfortunately, we have not been able to find a simple explanation for those bands. This would make it even more interesting to know if these bands can be found in experimental studies as well.

In Figs. 12.15 and 12.16, one can see that the excitations around $2V$ and $3V$ gain weight for larger U. This makes sense because the strong on-site interaction U causes a deviation from the clear CDW pattern depicted in Fig. 12.10 and therefore leads to more sites which are not strictly doubly occupied. Thus, less energy needs to be paid if one wants to add a particle on an adjacent site. It is also noteworthy that the spectral function becomes more and more symmetric about $k = \pi/2$ for smaller values of U. This is explained by the fact that the system would be in a fully dimerized state at $U = 0$ and, therefore, the excitation spectrum would then be completely reflection symmetric about $k = \pi/2 = k_F$.

These findings for the spectral function in the CDW phase agree with the findings of Aichhorn et al. [77] but are more detailed. The lack of detail in Ref. [77] is due to the fact that a variational cluster approach that is based on dynamical mean field theory (DMFT), is used. This method is only exact in the limit of infinite dimensions and the calculation is restricted to a cluster size of $N = 12$.

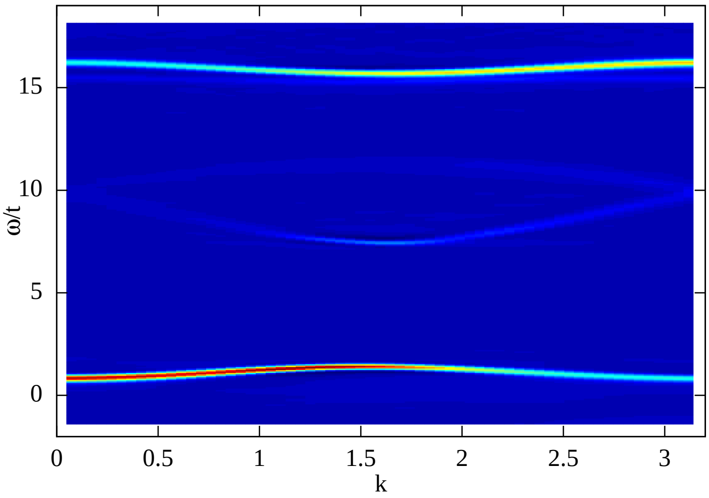

(a) $U/t = 1$

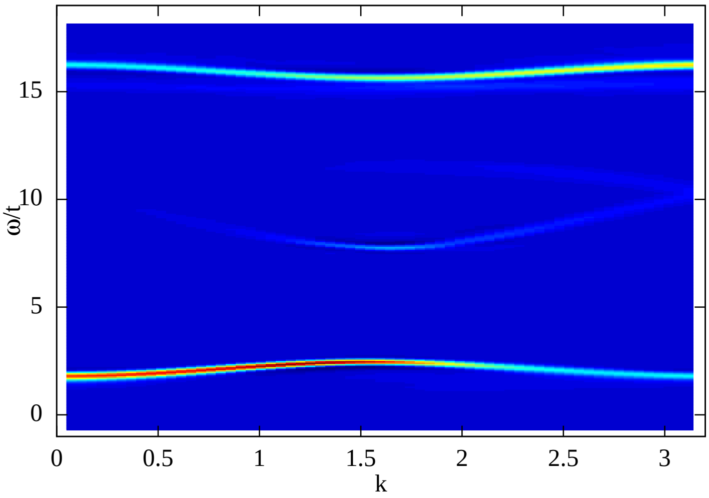

(b) $U/t = 2$

Figure 12.11: Angle-resolved spectral function $A(k, \omega)$ of the half-filled extended Hubbard model for $V/t = 4$ and U/t from 1 to 2.

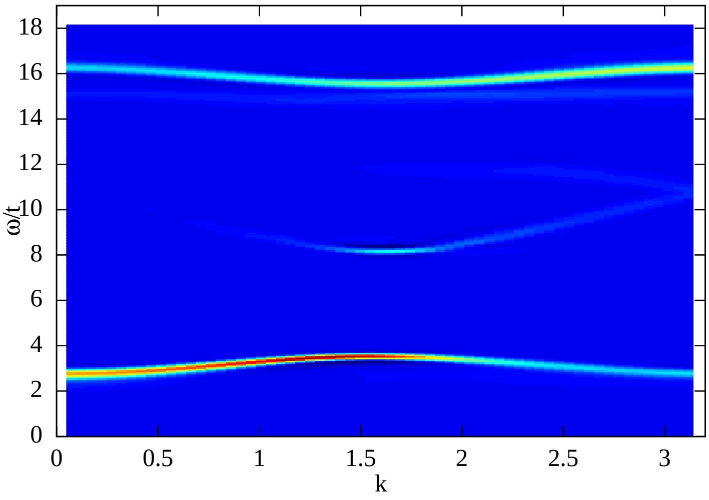

(a) $U/t = 3$

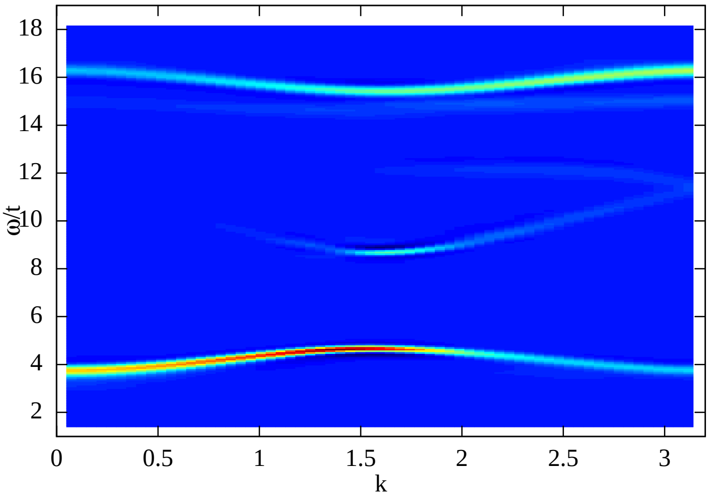

(b) $U/t = 4$

Figure 12.12: Angle-resolved spectral function $A(k, \omega)$ of the half-filled extended Hubbard model for $V/t = 4$ and U/t from 3 to 4.

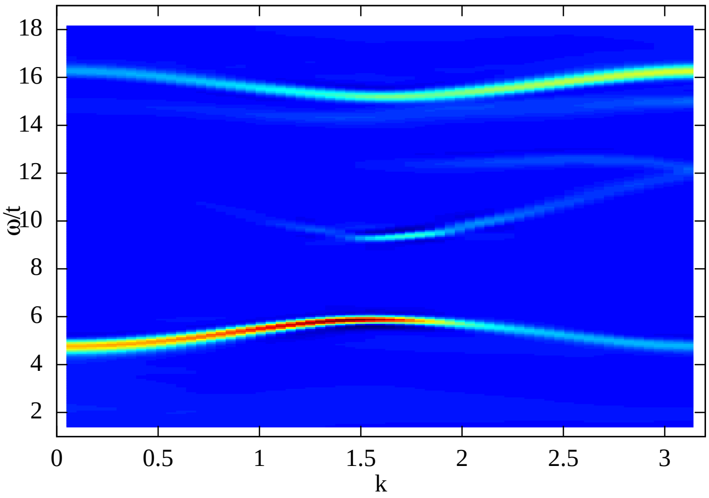

(a) $U/t = 5$

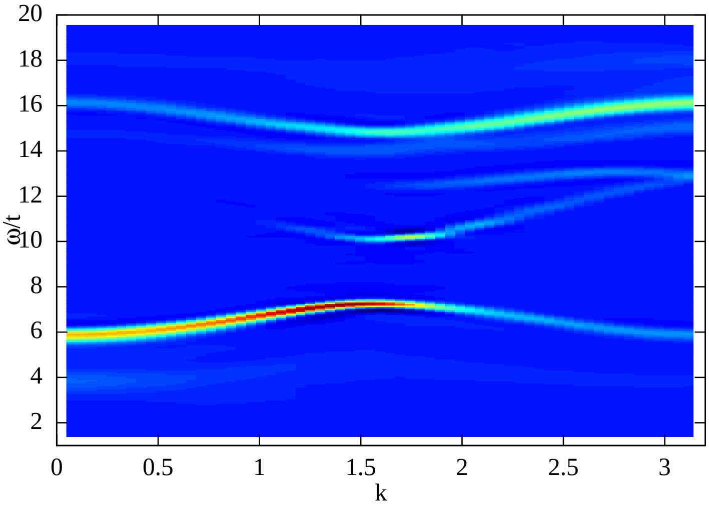

(b) $U/t = 6$

Figure 12.13: Angle-resolved spectral function $A(k, \omega)$ of the half-filled extended Hubbard model for $V/t = 4$ and U/t from 5 to 6.

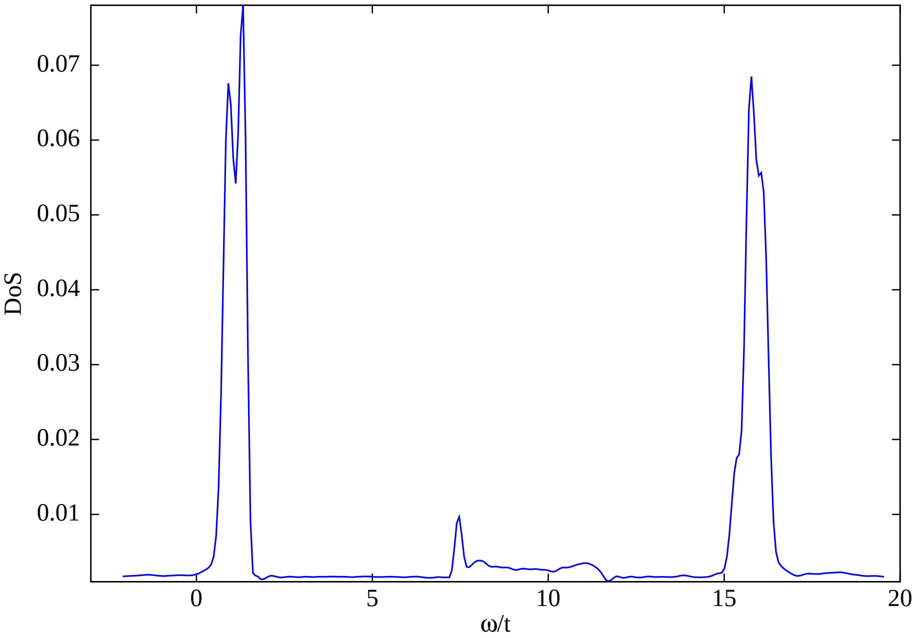

(a) $U/t = 1$

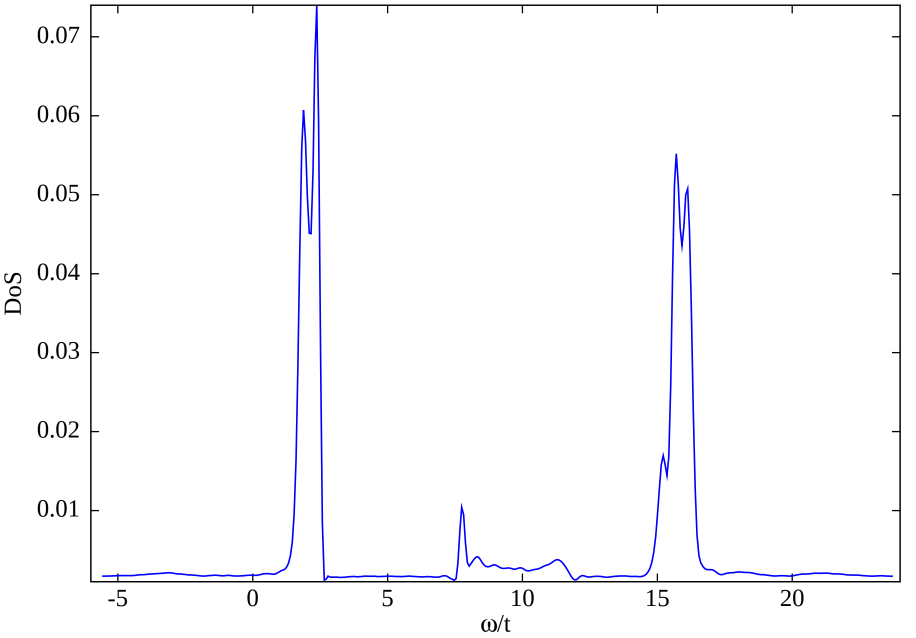

(b) $U/t = 2$

Figure 12.14: Density of states $N(\omega)$ of the half-filled extended Hubbard model for $V/t = 4$ and U/t from 1 to 2.

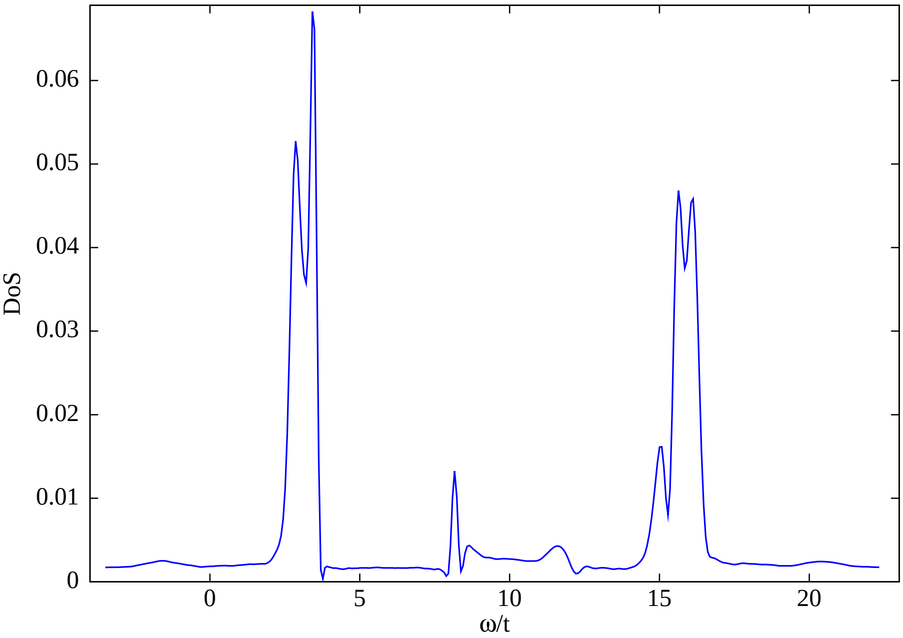

(a) $U/t = 3$

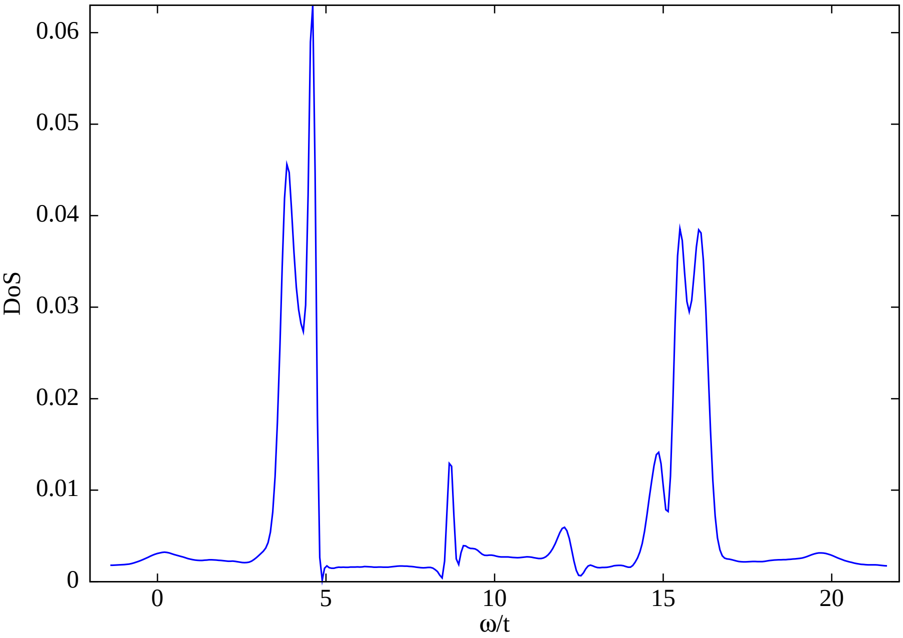

(b) $U/t = 4$

Figure 12.15: Density of states $N(\omega)$ of the half-filled extended Hubbard model for $V/t = 4$ and U/t from 3 to 4.

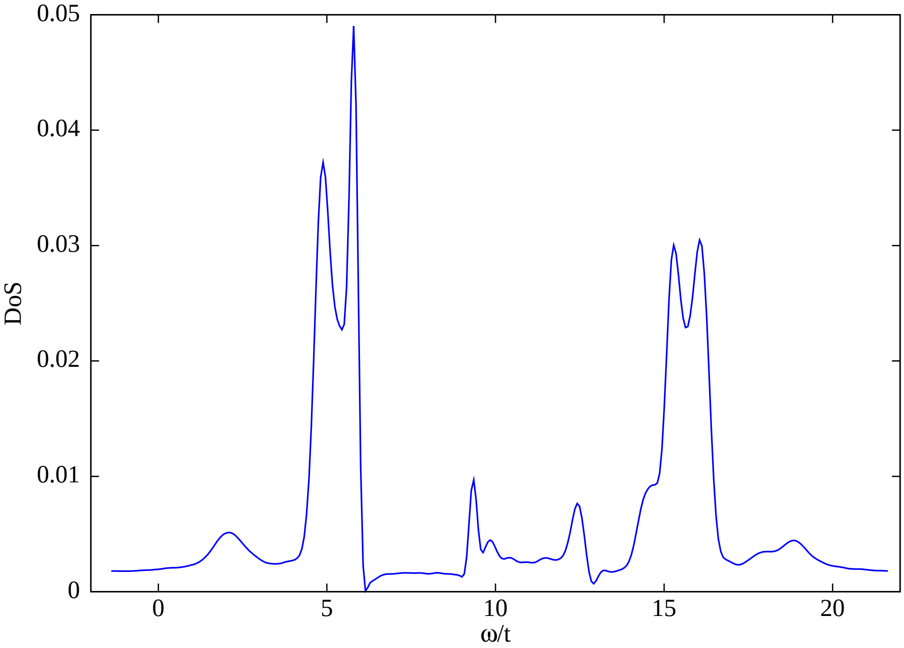

(a) $U/t = 5$

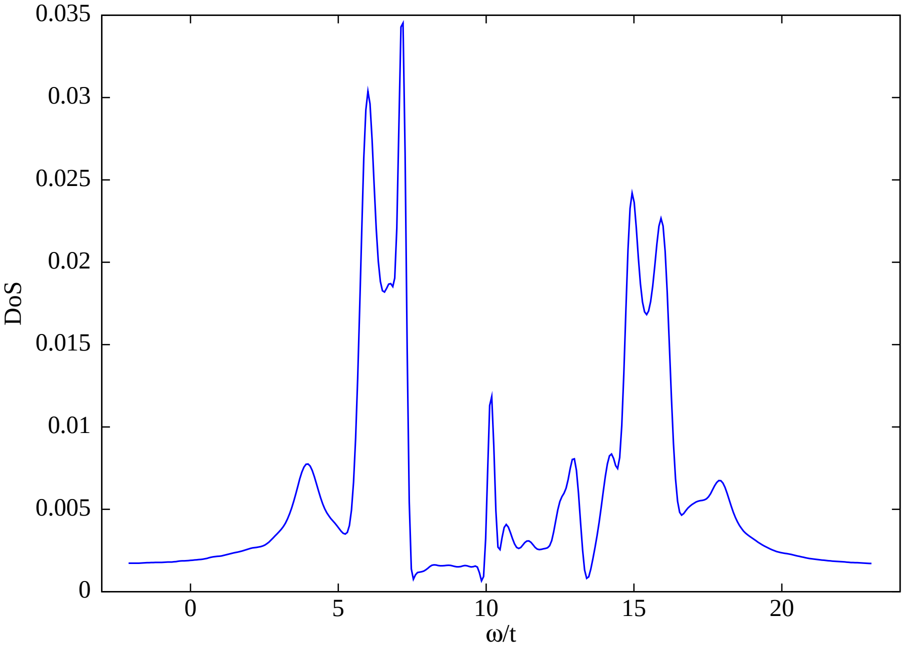

(b) $U/t = 6$

Figure 12.16: Density of states $N(\omega)$ of the half-filled extended Hubbard model for $V/t = 4$ and U/t from 5 to 6.

12.4 The Transition Region

The features in the transition region are especially interesting because analytical calculations are virtually impossible in this parameter regime; as far as we know no other numerical data for the angle-resolved spectral function is available.

We can see that the separation of the spectral weight into the different branches disappears as the transition point is approached either coming from the SDW or from the CDW phase. One can observe that the system passes through a state that has a spectral function very similar to the spectral function of a small-U Hubbard model. This can be seen by comparing Figs. 12.18(b), 12.19(a), 12.23(b) and 12.24(a) with Fig. 12.25. This similarity is due to the fact that the effects of the repulsive on-site interaction U and the repulsive nearest-neighbor interaction V compensate each other at half filling around $U \approx 2V$, leaving the system in a state that exhibits properties which are very similar to the ground state of the Hubbard model at small U. While the similarities between the Hubbard model at small U and the extended Hubbard model are striking, the spectral functions are not identical. In comparison to the spectral function of the small-U Hubbard model (Fig. 12.25), we see that in the extended Hubbard model (Figs. 12.18(b), 12.19(a), 12.23(b), and 12.24(a)) the spectral weight of the excitation bands is significantly more smeared out as $k \rightarrow 0$ and $k \rightarrow \pi$.

We can conclude, though, that many features of the angle-resolved spectral function of the half-filled extended Hubbard model are still not well understood. This is especially true in the phase transition region. Further investigations as well as verification by experiments would be sensible.

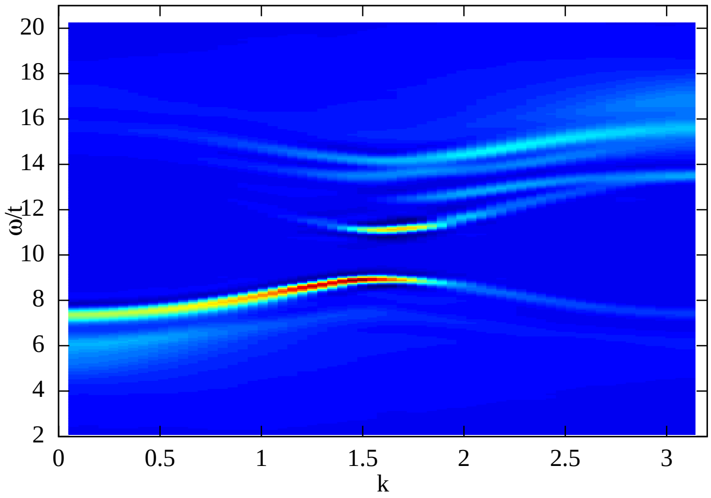

(a) $U/t = 7$

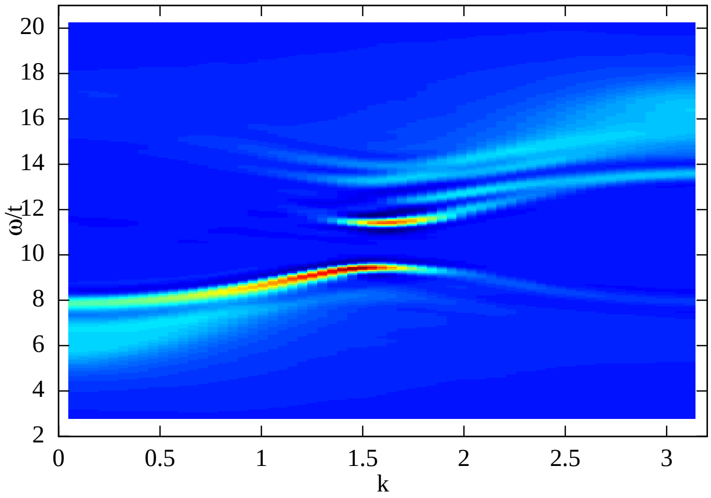

(b) $U/t = 7.25$

Figure 12.17: Angle-resolved spectral function $A(k, \omega)$ of the half-filled extended Hubbard model for $V/t = 4$ and U/t from 7 to 7.25.

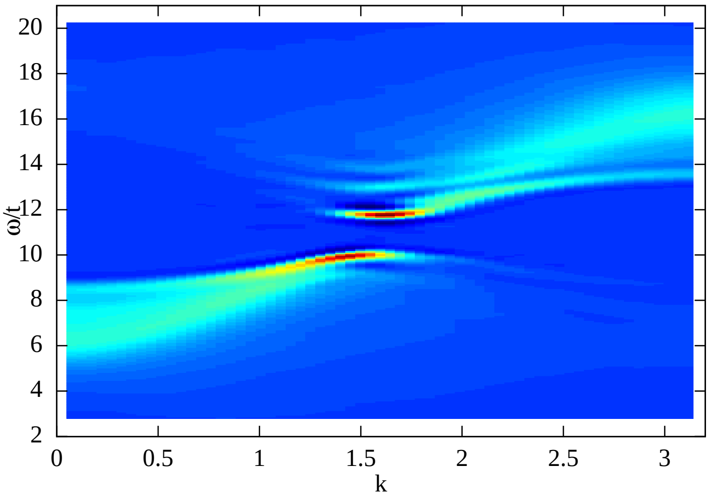

(a) $U/t = 7.5$

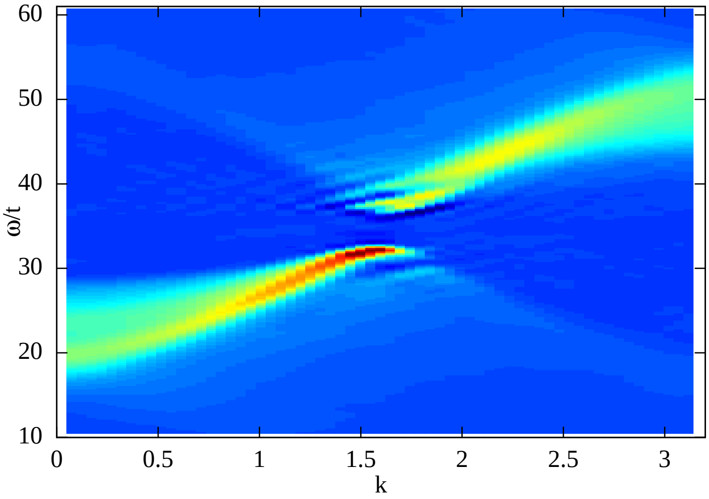

(b) $U/t = 7.77$

Figure 12.18: Angle-resolved spectral function $A(k,\omega)$ of the half-filled extended Hubbard model for $V/t = 4$ and U/t from 7.5 to 7.77.

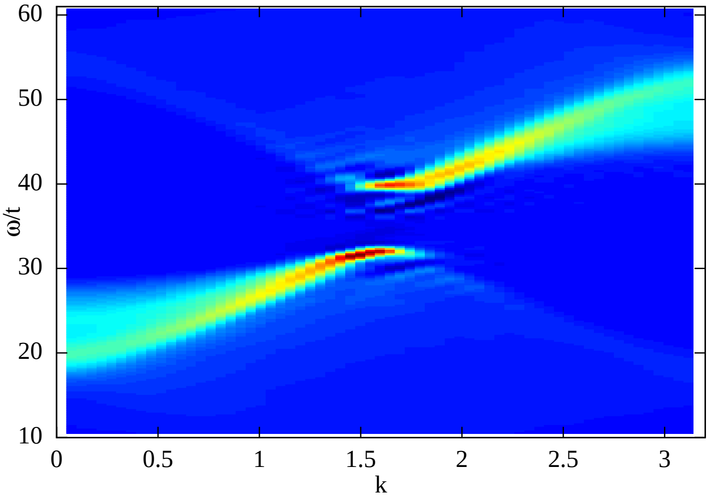

(a) $U/t = 7.86$

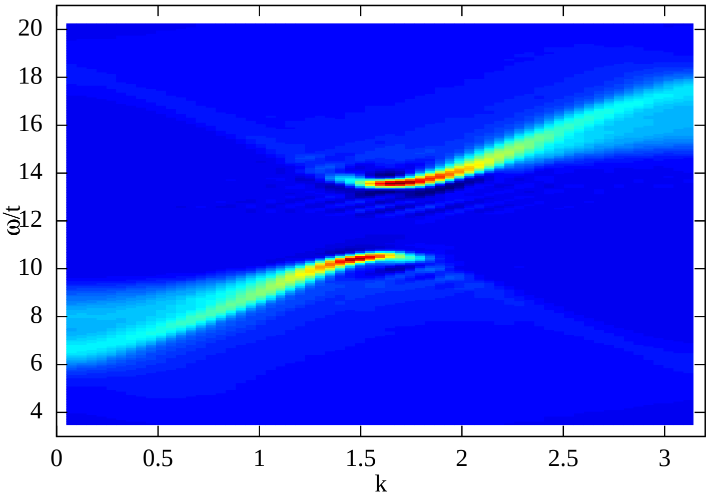

(b) $U/t = 8$

Figure 12.19: Angle-resolved spectral function $A(k, \omega)$ of the half-filled extended Hubbard model for $V/t = 4$ and U/t from 7.86 to 8.

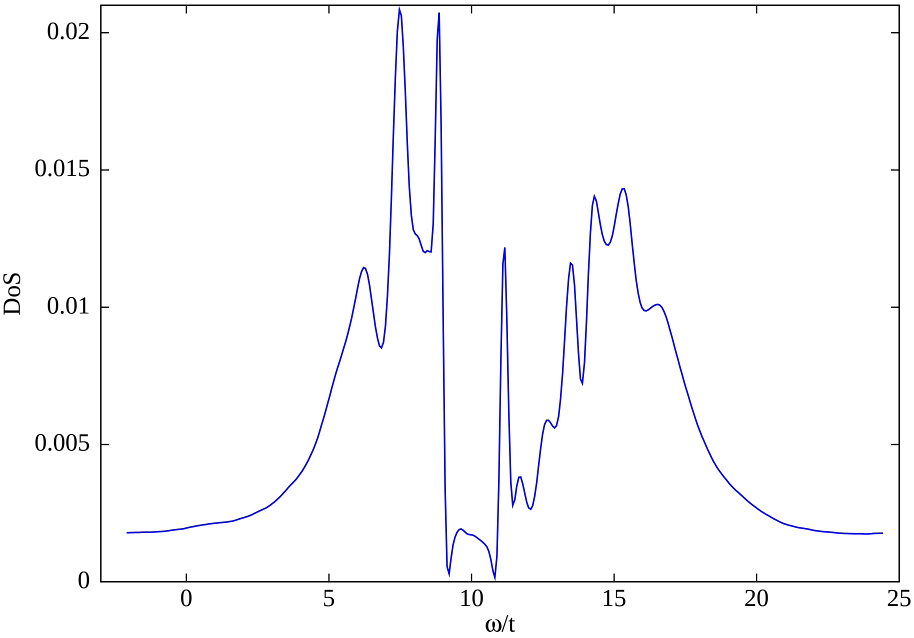

(a) $U/t = 7$

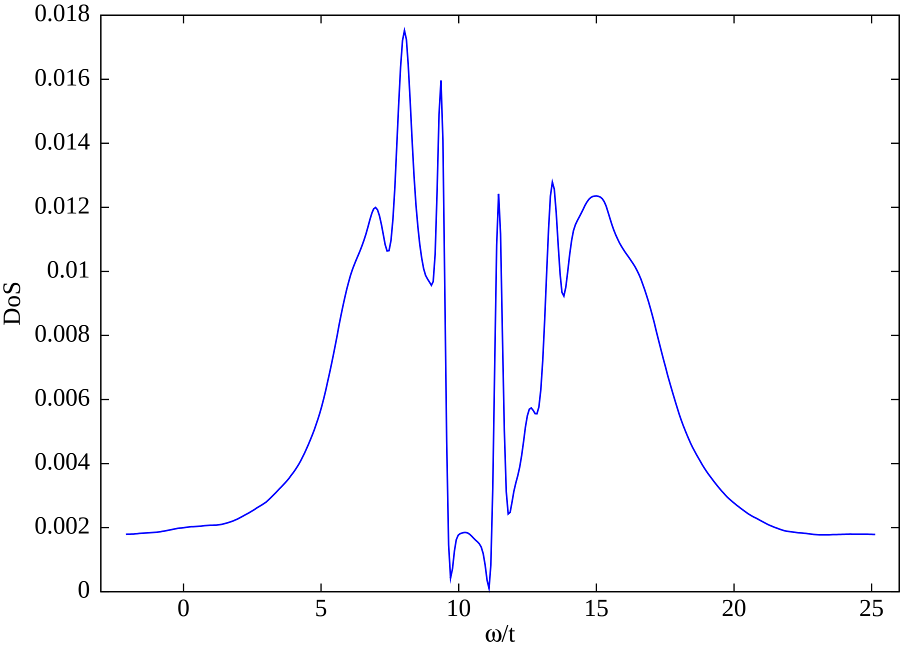

(b) $U/t = 7.25$

Figure 12.20: Density of states $N(\omega)$ of the half-filled extended Hubbard model for $V/t = 4$ and U/t from 7 to 7.25.

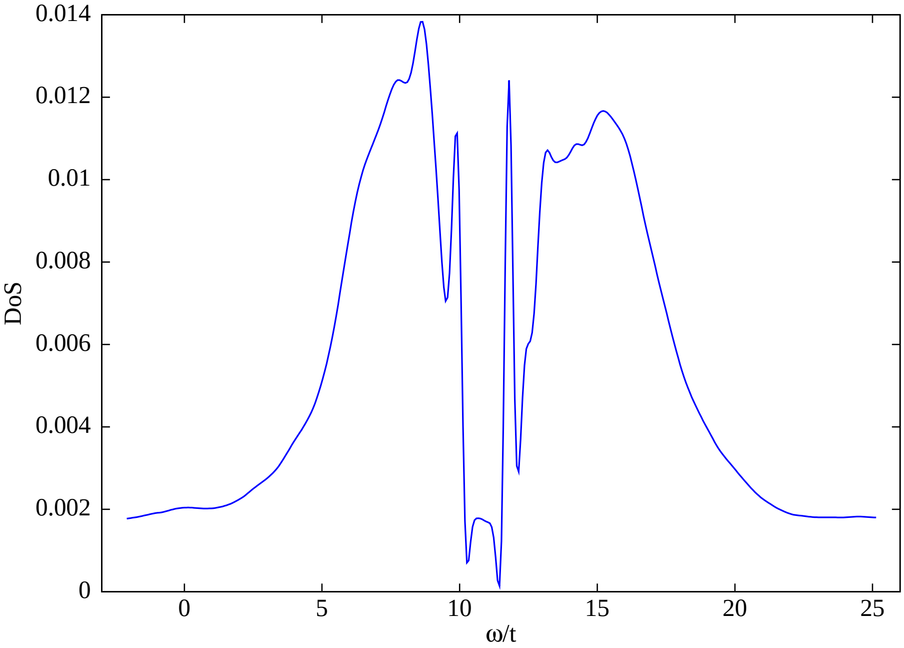

(a) $U/t = 7.5$

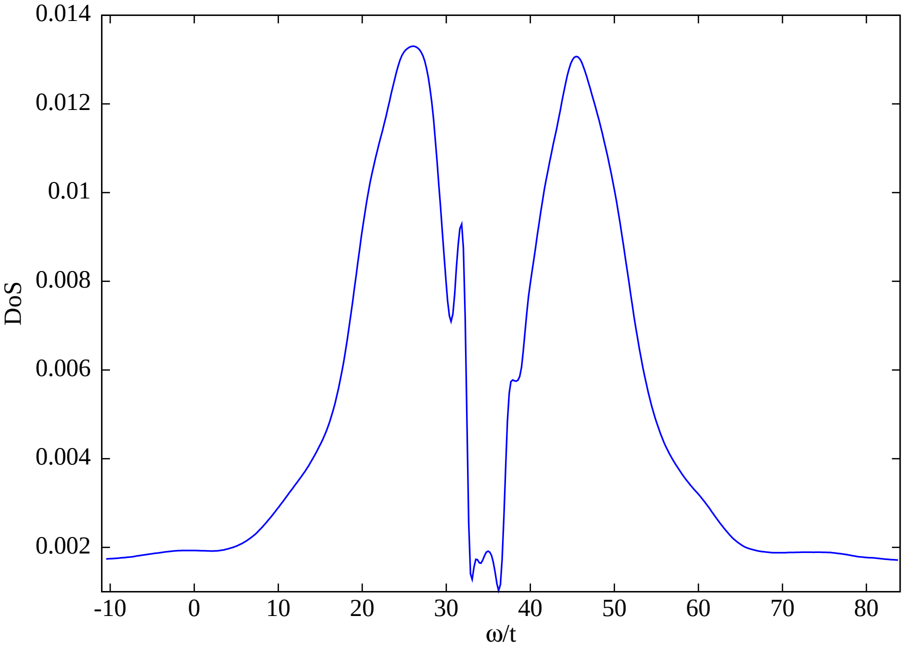

(b) $U/t = 7.77$

Figure 12.21: Density of states $N(\omega)$ of the half-filled extended Hubbard model for $V/t = 4$ and U/t from 7.5 to 7.77.

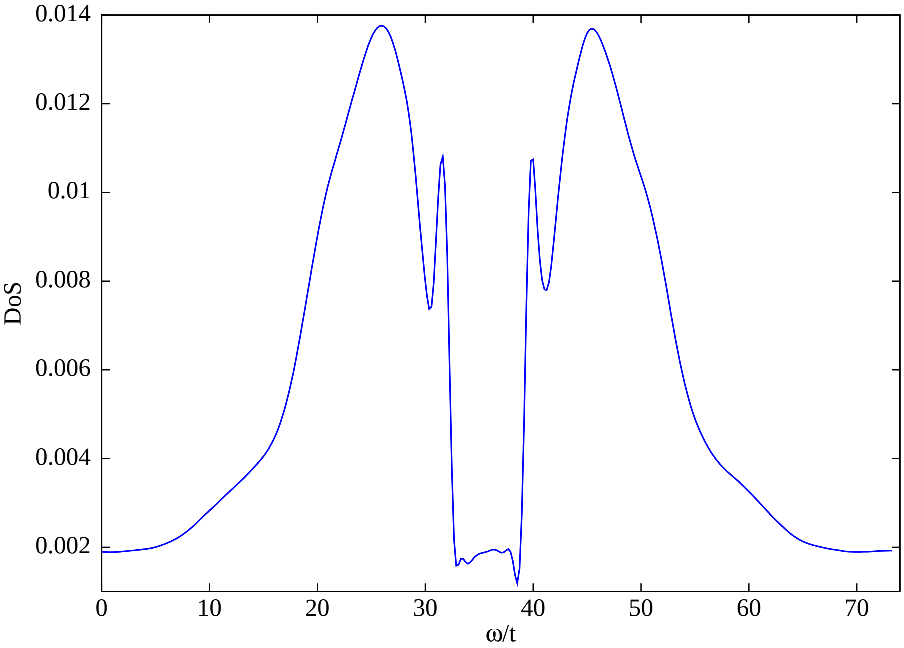

(a) $U/t = 7.86$

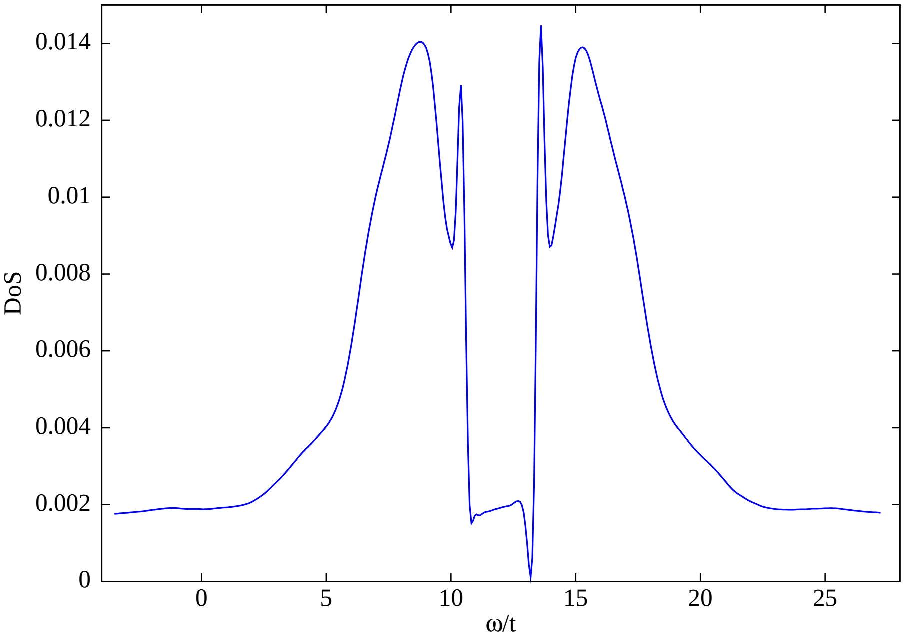

(b) $U/t = 8$

Figure 12.22: Density of states $N(\omega)$ of the half-filled extended Hubbard model for $V/t = 4$ and U/t from 7.86 to 8.

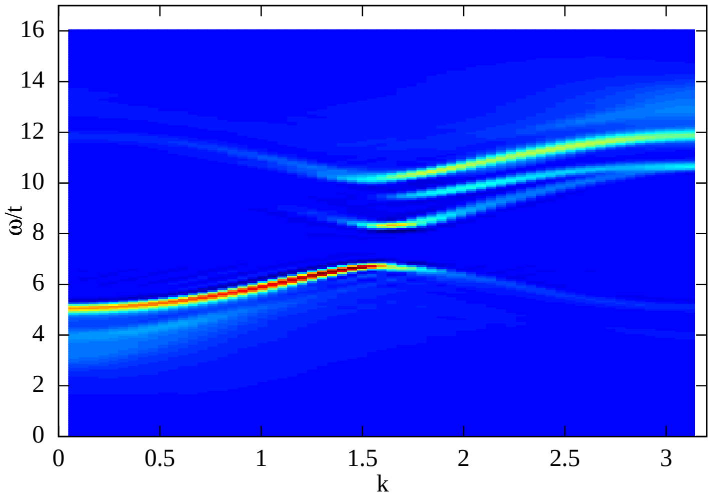

(a) $U/t = 5$

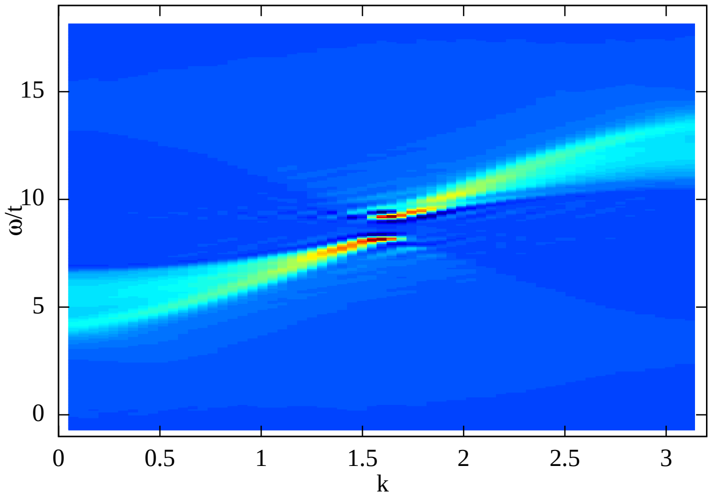

(b) $U/t = 5.75$

Figure 12.23: Angle-resolved spectral function $A(k, \omega)$ of the half-filled extended Hubbard model for $V/t = 3$ and U/t from 5 to 5.75.

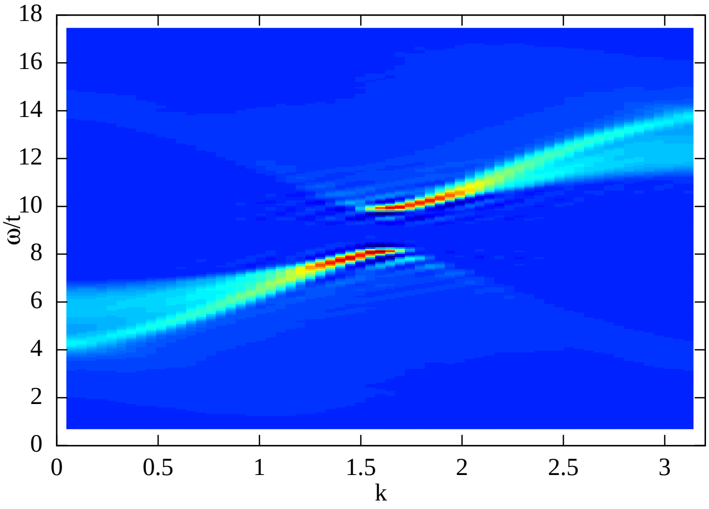

(a) $U/t = 6$

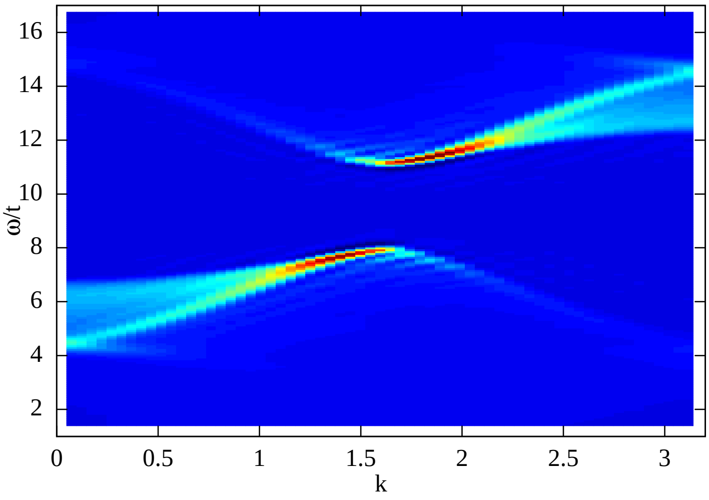

(b) $U/t = 7$

Figure 12.24: Angle-resolved spectral function $A(k, \omega)$ of the half-filled extended Hubbard model for $V/t = 3$ and U/t from 6 to 7.

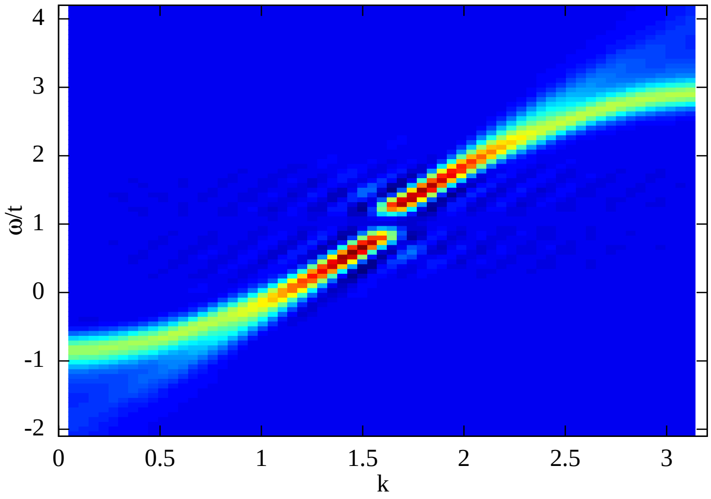

Figure 12.25: Angle-resolved spectral function $A(k, \omega)$ of the half-filled Hubbard model at $U/t = 2$.

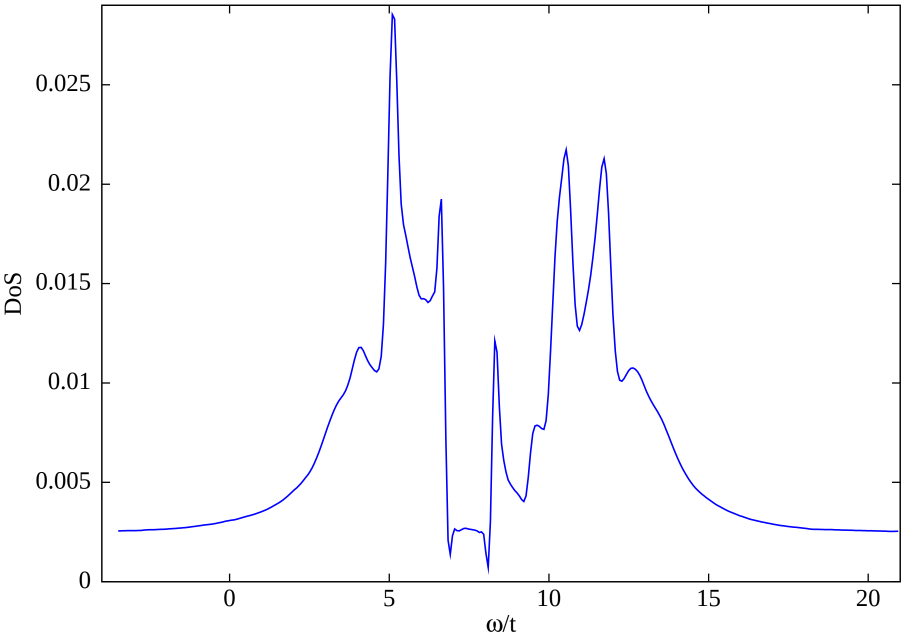

(a) $U/t = 5$

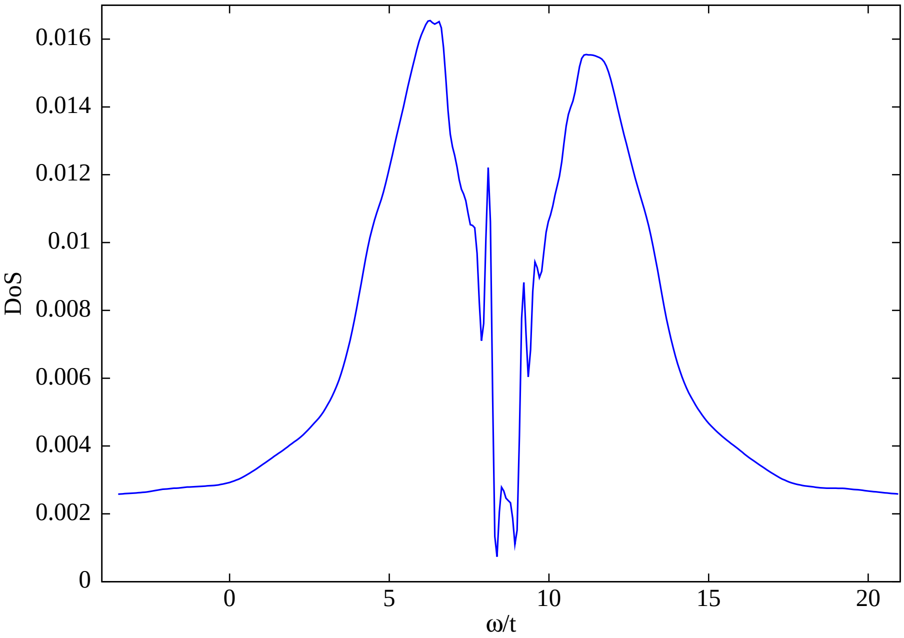

(b) $U/t = 5.75$

Figure 12.26: Density of states $N(\omega)$ of the half-filled extended Hubbard model for $V/t = 3$ and U/t from 5 to 5.75.

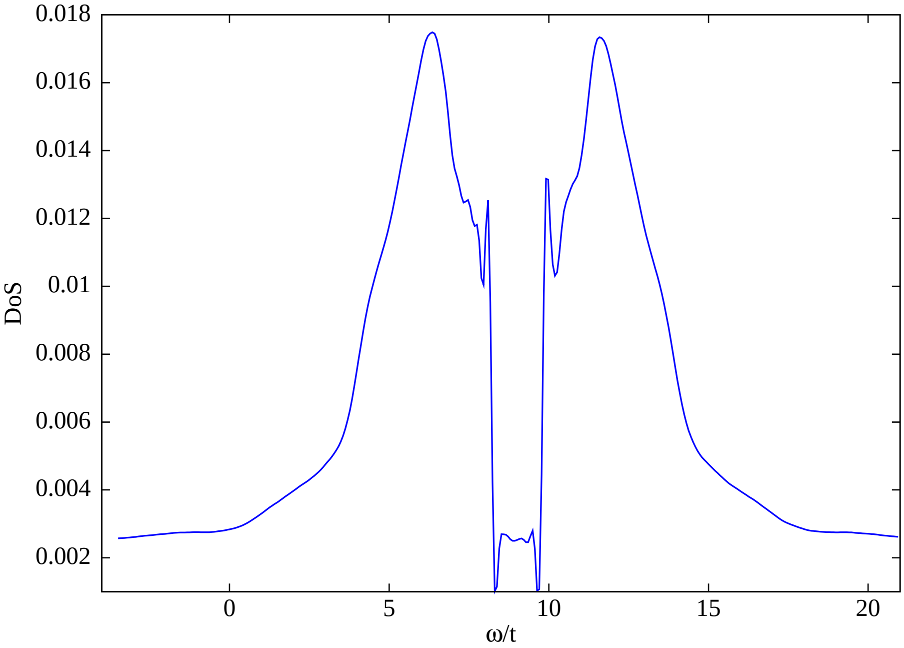

(a) $U/t = 6$

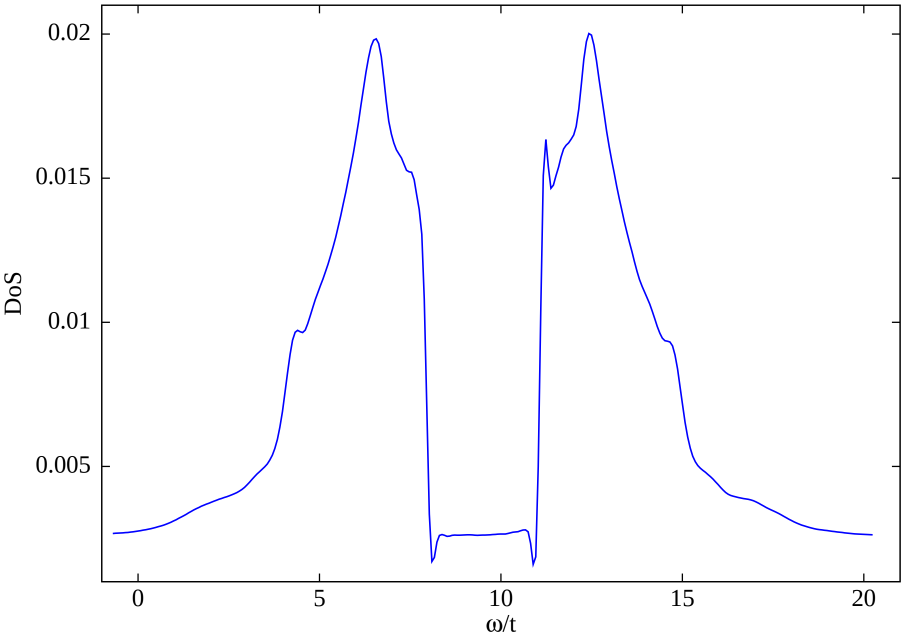

(b) $U/t = 7$

Figure 12.27: Density of states $N(\omega)$ of the half-filled extended Hubbard model for $V/t = 3$ and U/t from 6 to 7.

Chapter 13

Conclusion

13.1 Achievements

The results presented in this thesis consist of two primary parts: In the first part, we have used recently developed quantum-information-based measures within the DMRG (see Sec. 4.1) to calculate the ground-state phase diagram of the one-dimensional extended Hubbard model (2.8). In particular, we have examined the phase transition region in which there is a competition between two phases, showing antiferromagnetic and charge-ordered behavior, respectively. Here we have been able to lend significant support to a recently proposed picture that predicts the existence of a phase featuring alternating bond strength between the two above mentioned phases [2]. Our findings for the phase diagram as well as a discussion of the results and a comparison with previous results are detailed in Chapter 11.

In the second part, we have explained the implementation and adaption of recent ideas for calculating experimentally relevant dynamical response functions using the DMRG. These ideas are based on time-evolving a quantum mechanical system directly to obtain the dynamical response of the system, e.g., the retarded Greens function. Using these ideas, we have proceeded to calculate the angle-resolved spectral function and the density of states for the extended Hubbard model. This is important for understanding and interpreting the results of various scattering experiments such as angle-resolved photoemission or electron scattering. Indications are that these new methods will allow for significantly faster calculations of dynamical response functions. In Chapters 8 and 9 we have explained in detail the theory and algorithms used in our calculations. In Chapter 12, we have presented the calculated data for the angle-resolved spectral functions and the density of states of the extended Hubbard model (2.8). The calculations have been conducted over a broad range of parameters covering all three phases found in the system. Our findings from the first part of this thesis have been used to choose appropriate parameters. In the charge-ordered phase, we have been able to resolve features in the photoemission spectrum that were previously not seen. These features seem to be excitons but further investigation might be needed to determine this.

Additionally, we have discussed recent developments of DMRG algorithms in Chapter 7. These newly developed algorithms have the potential to overcome the problems recent implementations of DMRG algorithms have with one-dimensional systems with periodic boundary conditions and two-dimensional systems. We have explained the basic idea behind these new matrix-product-based methods and have shown how the DMRG can be seen as a subclass of the group of matrix-product-based methods. A working DMRG program using tensor networks has also been implemented as part of this thesis.

13.2 Outlook

There are many opportunities for application and development of these methods. The most important of these possibilities is outlined in the following.

1. The easiest and most straightforward possible extension to this thesis would be to use the newly developed algorithms, i.e., the functionality to calculate dynamical response functions, on other models to calculate their excitation spectrum. These models could include spin models, bosonic systems, narrow ladder systems or a combination of the above and would allow very precise predictions for the excitation spectrum of real materials. An interesting area of application would be the newly discovered spin Bose metals, because their dynamic properties are completely unknown right now.

2. The time evolution algorithm can also be applied along the imaginary time axis to simulate states at finite temperature. Since relatively few low-lying excited states carry the majority of the weight in an ensemble at low temperatures, the Lanczos time evolution is the most promising in this respect. Being able to calculate properties for finite temperature systems is very useful because most experiments take place at temperatures significantly above 0 K.

3. To develop and implement the algorithms presented here in a momentum space (k space) based DMRG program would be an effective way

for examining the dynamical properties of a system with spatial long-range correlations, e.g., the Hubbard model for $U \ll t$, because these systems usually exhibit only short-range interactions in k-space and, therefore, converge quickly within the DMRG algorithm.

4. An efficient implementation of the DMRG and related algorithms using tensor networks, as presented in Chapter 7, would be the most promising endeavor at this point because it would allow for the treatment of systems with periodic boundary conditions with much higher efficiency. It might also be possible, if massive parallelism is used, to calculate larger two-dimensional systems than what is possible with DMRG algorithm currently. This functionality could be one of the first steps in explaining high-T_c superconductivity.

5. Also, all algorithms presented here can easily be adapted to run in the context of a tensor-based DMRG program and could then be used on the systems which cannot be efficiently treated with a standard DMRG implementation. For example, using periodic boundary conditions would rid one of the previously mentioned problem of having to average multiple sites when calculating spectral functions in a system with a dimerized ground state.

Appendices

Appendix A

Solution of the Tight Binding Model

The analytic solution of the tight binding model (2.2) with open boundary conditions (OBC) on a one-dimensional chain of length L is presented in the following.

$$\begin{aligned}
\text{Ansatz:}& \\
c_j^\dagger &= N\sum_{k=0}^{\infty}\sin(kj)c_k^\dagger. \\
c_j &= N\sum_{k=0}^{\infty}\sin(kj)c_k. \\
\text{We have OBC } &\Rightarrow \sin(0)=\sin\left(k(L+1)\right)=0. \\
&\Rightarrow k_n = \frac{n\pi}{L+1} \\
&\Rightarrow c_j^\dagger = N\sum_{n=0}^{L}\sin(k_n j)c_k^\dagger \\
\text{and } c_j &= N\sum_{n=0}^{L}\sin(k_n j)c_k.
\end{aligned}$$

Normalization:

$$\begin{aligned}
\langle 0|c_j c_j^\dagger|0\rangle = 1 &= N^2 \sum_{n,m=0}^{L} \sin(k_n j)\sin(k_m j)\underbrace{\langle 0|c_{k_n} c_{k_m}^\dagger|0\rangle}_{\delta_{n,m}} \\
&= N^2 \sum_{n=0}^{L} \sin^2(k_n j) = N^2 \sum_{n=0}^{L}\left(\frac{1}{2}-\frac{1}{2}\cos(2k_n j)\right) \\
&= \frac{N^2(L+1)}{2} - \frac{N^2}{2}\sum_{n=0}^{L}\cos(2k_n j) \\
&= \frac{N^2(L+1)}{2} - \frac{N^2}{2}\sum_{n=0}^{L}\left(\frac{e^{\frac{i\pi n}{L+1}2j}}{2}+\frac{e^{\frac{-i\pi n}{L+1}2j}}{2}\right) \\
&= \frac{N^2(L+1)}{2} - \frac{N^2}{4}\left(\underbrace{\frac{1-e^{2i\pi j}}{1-e^{\frac{2i\pi}{L+1}j}}}_{=0}+\underbrace{\frac{1-e^{-2i\pi j}}{1-e^{-\frac{2i\pi}{L+1}j}}}_{=0}\right) \\
&= \frac{L+1}{2}N^2. \\
\Rightarrow N &= \sqrt{\frac{2}{L+1}}.
\end{aligned}$$

Inserting this Ansatz into the Hamiltonian, yields

$$\begin{aligned}
H &= \sum_{j=1}^{L-1}\left(c_{j+1}^\dagger c_j + c_j^\dagger c_{j+1}\right) \\
&= \sum_{j=1}^{L-1}\sum_{n,m=0}^{L} N^2 \sin(k_n(j+1))\sin(k_m j)\left(c_{k_n}^\dagger c_{k_m} + c_{k_m}^\dagger c_{k_n}\right) \\
&= \sum_{n,m=0}^{L}\left(c_{k_n}^\dagger c_{k_m} + c_{k_m}^\dagger c_{k_n}\right) N^2 \\
&\times\left(\cos(k_n)\underbrace{\sum_{j=0}^{N}\sin(k_n j)\sin(k_m j)}_{(1)} + \sin(k_n)\underbrace{\sum_{j=0}^{N}\cos(k_n j)\sin(k_m j)}_{(2)}\right).
\end{aligned}$$

Considering $m \neq n$:

$$(1) = \sum_{j=0}^{L}\left(\frac{e^{\frac{i\pi nj}{L+1}} - e^{\frac{-i\pi nj}{L+1}}}{2i} \times \frac{e^{\frac{i\pi mj}{L+1}} - e^{\frac{-i\pi mj}{L+1}}}{2i}\right)$$

$$= -\frac{1}{4}\sum_{j=0}^{L}\left(e^{\frac{i\pi j}{L+1}(n+m)} + e^{\frac{-i\pi j}{L+1}(n+m)} - e^{\frac{i\pi j}{L+1}(n-m)} - e^{\frac{-i\pi j}{L+1}(n-m)}\right)$$

$$= -\frac{1}{4}\left(\frac{1 - e^{i\pi(n+m)}}{1 - e^{\frac{i\pi}{L+1}(n+m)}} + \frac{1 - e^{-i\pi(n+m)}}{1 - e^{\frac{-i\pi}{L+1}(n+m)}} - \frac{1 - e^{i\pi(n-m)}}{1 - e^{\frac{i\pi}{L+1}(n-m)}} - \frac{1 - e^{-i\pi(n-m)}}{1 - e^{\frac{-i\pi}{L+1}(n-m)}}\right).$$

If $n - m = 2a,$ then

$$(1) = -\frac{1}{4}\left(\frac{1 - e^{i2\pi(a+m)}}{1 - e^{\frac{i\pi}{L+1}2(a+m)}} + \frac{1 - e^{-i2\pi(a+m)}}{1 - e^{\frac{-i\pi}{L+1}2(a+m)}} - \frac{1 - e^{i\pi 2a}}{1 - e^{\frac{i\pi}{L+1}2a}} - \frac{1 - e^{-i\pi 2a}}{1 - e^{\frac{-i\pi}{L+1}2a}}\right) = 0.$$

If $n - m = 2a + 1,$ then

$$(1) = -\frac{1}{4}\left(\frac{1 - e^{i2\pi(a+m+\frac{1}{2})}}{1 - e^{\frac{i\pi}{L+1}2(a+m+\frac{1}{2})}} + \frac{1 - e^{-i2\pi(a+m+\frac{1}{2})}}{1 - e^{\frac{-i\pi}{L+1}2(a+m+\frac{1}{2})}} - \frac{1 - e^{i\pi(2a+1)}}{1 - e^{\frac{i\pi}{L+1}(2a+1)}} - \frac{1 - e^{-i\pi(2a+1)}}{1 - e^{\frac{-i\pi}{L+1}(2a+1)}}\right)$$

$$= -\frac{1}{2}\left(\frac{1 - e^{\frac{-i\pi}{L+1}2(a+m+\frac{1}{2})} + 1 - e^{\frac{i\pi}{L+1}2(a+m+\frac{1}{2})}}{(1 - e^{\frac{i\pi}{L+1}2(a+m+\frac{1}{2})})(1 - e^{\frac{-i\pi}{L+1}2(a+m+\frac{1}{2})})} - \frac{1 - e^{\frac{-i\pi}{L+1}2(a+\frac{1}{2})} + 1 - e^{\frac{i\pi}{L+1}2(a+\frac{1}{2})}}{(1 - e^{\frac{i\pi}{L+1}2(a+\frac{1}{2})})(1 - e^{\frac{-i\pi}{L+1}2(a+\frac{1}{2})})}\right) = 0.$$

$$
\begin{aligned}
(2) &= \sum_{j=0}^{L} \left(\frac{e^{\frac{i\pi nj}{L+1}} + e^{\frac{-i\pi nj}{L+1}}}{2} \times \frac{e^{\frac{i\pi mj}{L+1}} - e^{\frac{-i\pi mj}{L+1}}}{2i} \right) \\
&= \frac{1}{4i} \sum_{j=0}^{L} \left(e^{\frac{i\pi j}{L+1}(n+m)} - e^{\frac{-i\pi j}{L+1}(n+m)} + e^{\frac{i\pi j}{L+1}(m-n)} - e^{\frac{-i\pi j}{L+1}(m-n)} \right) \\
&= \frac{1}{4i} \left(\frac{1 - e^{i\pi(n+m)}}{1 - e^{\frac{i\pi}{L+1}(n+m)}} - \frac{1 - e^{-i\pi(n+m)}}{1 - e^{\frac{-i\pi}{L+1}(n+m)}} \right. \\
&\qquad\qquad \left. + \frac{1 - e^{i\pi(m-n)}}{1 - e^{\frac{i\pi}{L+1}(m-n)}} - \frac{1 - e^{-i\pi(m-n)}}{1 - e^{\frac{-i\pi}{L+1}(m-n)}} \right).
\end{aligned}
$$

If $m - n = 2a,$ then

$$
= \frac{1}{4i} \left(\frac{1 - e^{i2\pi(a+n)}}{1 - e^{\frac{i\pi}{L+1}2(a+n)}} - \frac{1 - e^{-i2\pi(a+n)}}{1 - e^{\frac{-i\pi}{L+1}2(a+n)}} + \frac{1 - e^{i\pi 2a}}{1 - e^{\frac{i\pi}{L+1}2a}} - \frac{1 - e^{-i\pi 2a}}{1 - e^{\frac{-i\pi}{L+1}2a}} \right) = 0.
$$

If $m - n = 2a + 1,$ then

$$
\begin{aligned}
&= \frac{1}{4i} \left(\frac{1 - e^{i2\pi(a+n+\frac{1}{2})}}{1 - e^{\frac{i\pi}{L+1}2(a+n+\frac{1}{2})}} - \frac{1 - e^{-i2\pi(a+n+\frac{1}{2})}}{1 - e^{\frac{-i\pi}{L+1}2(a+n+\frac{1}{2})}} \right. \\
&\qquad\qquad \left. + \frac{1 - e^{i\pi(2a+1)}}{1 - e^{\frac{i\pi}{L+1}(2a+1)}} - \frac{1 - e^{-i\pi(2a+1)}}{1 - e^{\frac{-i\pi}{L+1}(2a+1)}} \right) \\
&= \frac{1}{2i} \left(\frac{e^{-\frac{i\pi}{L+1}2(a+n+\frac{1}{2})} - e^{\frac{i\pi}{L+1}2(a+n+\frac{1}{2})}}{(1 - e^{-\frac{i\pi}{L+1}2(a+n+\frac{1}{2})})(1 - e^{\frac{i\pi}{L+1}2(a+n+\frac{1}{2})})} \right. \\
&\qquad\qquad \left. + \frac{e^{-\frac{i\pi}{L+1}2(a+\frac{1}{2})} - e^{\frac{i\pi}{L+1}2(a+\frac{1}{2})}}{(1 - e^{-\frac{i\pi}{L+1}2(a+\frac{1}{2})})(1 - e^{\frac{i\pi}{L+1}2(a+\frac{1}{2})})} \right) \\
&= -\frac{\sin(k_{n+m})}{2 - 2\cos(k_{n+m})} - \frac{\sin(k_{m-n})}{2 - 2\cos(k_{m-n})} \\
&= -\frac{2\sin(k_{n+m}/2)\cos(k_{n+m}/2)}{4\sin^2(k_{n+m}/2)} - \frac{2\sin(k_{m-n}/2)\cos(k_{m-n}/2)}{4\sin^2(k_{m-n}/2)} \\
&= \frac{\sin(k_m)}{\cos(k_n) - \cos(k_m)}.
\end{aligned}
$$

$\Rightarrow$ for $m \neq n$,

$$H = \sum_{\substack{n,m=0\\ n\neq m}}^{L} \left(c^\dagger_{k_n} c_{k_m} + c^\dagger_{k_m} c_{k_n}\right) N^2$$

$$\times \left(\cos(k_n) \underbrace{\sum_{j=0}^{N} \sin(k_n j)\sin(k_m j)}_{(1)} + \sin(k_n) \underbrace{\sum_{j=0}^{N} \cos(k_n j)\sin(k_m j)}_{(2)} \right)$$

$$= \sum_{\substack{n,m=0\\ n\neq m}}^{L} \left(c^\dagger_{k_n} c_{k_m} + c^\dagger_{k_m} c_{k_n}\right) N^2 (1-(-1)^{n-m}) \sin(k_n) \frac{\sin(k_m)}{\cos(k_n)-\cos(k_m)}$$

$$= \sum_{\substack{n,m=0\\ n\neq m}}^{L} c^\dagger_{k_n} c_{k_m} N^2 (1-(-1)^{n-m})$$

$$\times \left(\frac{\sin(k_n)\sin(k_m)}{\cos(k_n)-\cos(k_m)} - \frac{\sin(k_m)\sin(k_n)}{\cos(k_m)+\cos(k_n)} \right) = 0.$$

Considering $n = m$:

$$\sum_{j=1}^{L-1} \sum_{n=0}^{L} 2N^2 \sin(k_n(j+1))\sin(k_n j) c^\dagger_{k_n} c_{k_n} \overset{!}{=} \sum_{n=0}^{L} \epsilon(k_n) c^\dagger_{k_n} c_{k_n}$$

$$\sum_{j=1}^{L-1} \sin(k_n(j+1))\sin(k_n j) = \sum_{j=0}^{L} \sin(k_n(j+1))\sin(k_n j)$$

$$= \frac{1}{2} \sum_{j=0}^{L} (\cos(k_n) - \cos(k_n(2j+1)))$$

$$= \frac{L+1}{2}\cos(k_n) - \sum_{j=0}^{L} \frac{e^{\frac{(2j+1)i\pi n}{L+1}} + e^{-\frac{(2j+1)i\pi n}{L+1}}}{2}$$

$$= \frac{L+1}{2}\cos(k_n) - \frac{1}{2} \left(\underbrace{\frac{1-e^{2i\pi n}}{1-e^{\frac{i\pi n}{L+1}}}}_{=0} + \underbrace{\frac{1-e^{-2i\pi n}}{1-e^{-\frac{i\pi n}{L+1}}}}_{=0} \right) = \frac{L+1}{2}\cos(k_n).$$

$$\Rightarrow \epsilon(k_n) = 2\cos(k_n) = 2\cos\left(\frac{n\pi}{L+1}\right).$$

For half filling the retarded Greens function is:

$$\begin{aligned} G_{\mathrm{ret}}(t) &= -i\Theta(t)\langle\psi_0|[c_j(t), c_j^\dagger(0)]_+|\psi_0\rangle \\ &= -i\Theta(t)\left(\langle\psi_0|c_j(t)c_j^\dagger(0)|\psi_0\rangle + \langle\psi_0|c_j^\dagger(0)c_j(t)|\psi_0\rangle\right). \end{aligned}$$

$$\begin{aligned} \langle\psi_0|c_j(t)c_j^\dagger(0)|\psi_0\rangle &= \langle\psi_0|e^{iHt}\ c_j\ e^{-iHt}\ c_j^\dagger|\psi_0\rangle \\ &= e^{iE_0t}\sum_{n,m=0}^{L}\langle\psi_0|\sin(k_nj)c_{k_n}\ e^{-iHt}\ \sin(k_mj)c_{k_m}^\dagger|\psi_0\rangle \\ &= \sum_{n=0}^{L}\sum_{m=\frac{L}{2}+1}^{L}\sin(k_nj)\sin(k_mj)e^{iE_0t}e^{-i(E_0+2\cos(k_m))t}\underbrace{\langle\psi_0|c_{k_n}c_{k_m}^\dagger|\psi_0\rangle}_{=\delta_{n,m}} \\ &= \sum_{n=\frac{L}{2}+1}^{L}\sin^2(k_nj)e^{-2i\cos(k_n)t}. \end{aligned}$$

$$\begin{aligned} \langle\psi_0|c_j^\dagger(0)c_j(t)|\psi_0\rangle &= \langle\psi_0|c_j^\dagger\ e^{iHt}\ c_j\ e^{-iHt}|\psi_0\rangle \\ &= \sum_{n=0}^{L}\sum_{m=0}^{\frac{L}{2}}\sin(k_nj)\sin(k_mj)e^{-iE_0t}e^{i(E_0-2\cos(k_m))t}\underbrace{\langle\psi_0|c_{k_m}^\dagger c_{k_n}|\psi_0\rangle}_{=\delta_{n,m}} \\ &= \sum_{n=0}^{\frac{L}{2}}\sin^2(k_nj)e^{-2i\cos(k_n)t}. \end{aligned}$$

$$\begin{aligned} G_{\mathrm{ret}}(t) &= -i\Theta(t)\left(\sum_{n=\frac{L}{2}+1}^{L}\sin^2(k_nj)e^{-2i\cos(k_n)t} + \sum_{n=0}^{\frac{L}{2}}\sin^2(k_nj)e^{-2i\cos(k_n)t}\right) \\ &= -i\Theta(t)\sum_{n=0}^{L}\sin^2(k_nj)e^{-2i\cos(k_n)t}. \end{aligned}$$

Appendix B

Fourier Transformation of the Green's Function

The retarded Green's function is defined as

$$G^{\text{ret}}_{A,A^\dagger}(t) = -i\Theta(t)\left\langle \psi_0 \left| \left[A(t), A^\dagger(0)\right]_+ \right| \psi_0 \right\rangle$$

$$= -i\Theta(t)\left(\underbrace{\left\langle \psi_0 | A(t) A^\dagger(0) | \psi_0 \right\rangle}_{G^{\text{ret},U}_{A,A^\dagger}(t)} + \underbrace{\left\langle \psi_0 | A^\dagger(0) A(t) | \psi_0 \right\rangle}_{G^{\text{ret},L}_{A^\dagger,A}(t)} \right).$$

$$\begin{aligned}
\Rightarrow G^{\text{ret},U}_{A,A^\dagger}(\omega) &= \int_0^\infty dt\; G^{\text{ret},U}_{A,A^\dagger}(t) e^{i\omega t} \\
&= -i \int_0^\infty dt \left\langle \psi_0 \right| A(t) A^\dagger(0) \left| \psi_0 \right\rangle e^{i\omega t} \\
&= -i \int_0^\infty dt\; e^{i\omega t} \left\langle \psi_0 \right| e^{iHt}\, A\, e^{-iHt}\, A^\dagger \left| \psi_0 \right\rangle \\
&= -i \int_0^\infty dt \left\langle \psi_0 \right| e^{i(\omega + E_0)t}\, A\, e^{-iHt}\, A^\dagger \left| \psi_0 \right\rangle \\
&= -i \int_0^\infty dt \left\langle \psi_0 \right| A\, e^{i(\omega + E_0 - H)t}\, A^\dagger \left| \psi_0 \right\rangle \\
&= -i \lim_{\eta \to 0^+} \int_0^\infty dt \left\langle \psi_0 \right| A\, e^{i(\omega + i\eta + E_0 - H)t}\, A^\dagger \left| \psi_0 \right\rangle \\
&= \lim_{\eta \to 0^+} \left\langle \psi_0 \right| A \left(\omega + i\eta + E_0 - H\right)^{-1} A^\dagger \left| \psi_0 \right\rangle.
\end{aligned}$$

$$
\begin{aligned}
\Rightarrow G^{\mathrm{ret},L}_{A^\dagger,A}(\omega) &= \int_0^\infty dt\; G^{\mathrm{ret},L}_{A^\dagger,A}(t) e^{i\omega t} \\
&= -i \int_0^\infty dt \left\langle \psi_0 \right| A^\dagger(0) A(t) \left| \psi_0 \right\rangle e^{i\omega t} \\
&= -i \int_0^\infty dt\; e^{i\omega t} \left\langle \psi_0 \right| A^\dagger\, e^{iHt}\, A\, e^{-iHt} \left| \psi_0 \right\rangle \\
&= -i \int_0^\infty dt \left\langle \psi_0 \right| e^{i(\omega - E_0)t}\, A^\dagger\, e^{iHt}\, A \left| \psi_0 \right\rangle \\
&= -i \int_0^\infty dt \left\langle \psi_0 \right| A^\dagger\, e^{i(\omega - E_0 + H)t}\, A \left| \psi_0 \right\rangle \\
&= -i \lim_{\eta \to 0^+} \int_0^\infty dt \left\langle \psi_0 \right| A^\dagger\, e^{i(\omega + i\eta - E_0 + H)t}\, A \left| \psi_0 \right\rangle \\
&= \lim_{\eta \to 0^+} \left\langle \psi_0 \right| A^\dagger \left(\omega + i\eta - E_0 + H \right)^{-1} A \left| \psi_0 \right\rangle .
\end{aligned}
$$

Appendix C

Spectral Representation of the Green's Function

The spectral density is defined as

$$S_{A,B}(t) = \frac{1}{2\pi}\langle\psi_0|[A(t),B(0)]_+|\psi_0\rangle.$$

$$\begin{aligned}
\langle\psi_0|A(t)A^\dagger(0)|\psi_0\rangle &= \sum_n \langle\psi_0|A(t)|\psi_n\rangle\langle\psi_n|A^\dagger(0)|\psi_0\rangle \\
&= \sum_n \langle\psi_0|\, e^{iHt}\, A\, e^{-iHt}\, |\psi_n\rangle\langle\psi_n|A^\dagger|\psi_0\rangle \\
&= \sum_n \langle\psi_0|A|\psi_n\rangle\langle\psi_n|A^\dagger|\psi_0\rangle\; e^{i(E_0-E_n)t} \\
&= \sum_n \left|\langle\psi_n|A^\dagger|\psi_0\rangle\right|^2 e^{i(E_0-E_n)t}.
\end{aligned}$$

$$\begin{aligned}
\langle\psi_0|A^\dagger(0)A(t)|\psi_0\rangle &= \sum_n \langle\psi_0|A^\dagger(0)|\psi_n\rangle\langle\psi_n|A(t)|\psi_0\rangle \\
&= \sum_n \langle\psi_0|A^\dagger|\psi_n\rangle\langle\psi_n|\, e^{iHt}\, A\, e^{-iHt}\, |\psi_0\rangle \\
&= \sum_n \langle\psi_0|A^\dagger|\psi_n\rangle\langle\psi_n|A|\psi_0\rangle\; e^{i(E_n-E_0)t} \\
&= \sum_n |\langle\psi_n|A|\psi_0\rangle|^2\, e^{-i(E_0-E_n)t}.
\end{aligned}$$

$$\Rightarrow S_{A,A^\dagger}(t) = \frac{1}{2\pi}\left(\sum_n \left|\langle\psi_n|A^\dagger|\psi_0\rangle\right|^2 e^{i(E_0-E_n)t} + \sum_n |\langle\psi_n|A|\psi_0\rangle|^2\, e^{-i(E_0-E_n)t}\right).$$

$$\begin{aligned}\Rightarrow S_{A,A^\dagger}(\omega) &= \int_{-\infty}^{\infty} dt\, e^{i\omega t} S_{A,A^\dagger}(t) \\ &= \sum_n \left|\langle\psi_n|A^\dagger|\psi_0\rangle\right|^2 \delta(\omega-(E_0-E_n)) \\ &+ \sum_n |\langle\psi_n|A|\psi_0\rangle|^2 \delta(\omega-(E_n-E_0)).\end{aligned}$$

With the spectral representation of the retarded Green's function

$$\begin{aligned}G^{\text{ret}}_{A,A^\dagger}(\omega) &= \lim_{\eta\to0^+}\int_{-\infty}^{\infty} d\omega' \frac{S_{A,A^\dagger}(\omega)}{\omega-\omega'+i\eta} \\ &= \lim_{\eta\to0^+}\frac{\sum_n \left|\langle\psi_n|A^\dagger|\psi_0\rangle\right|^2}{\omega-(E_0-E_n)+i\eta} \\ &+ \lim_{\eta\to0^+}\frac{\sum_n |\langle\psi_n|A|\psi_0\rangle|^2}{\omega-(E_n-E_0)+i\eta}\end{aligned}$$

and the Dirac identity

$$\lim_{\eta\to0^+}\frac{1}{x-x_0+i\eta} = \mathcal{P}\frac{1}{x-x_0} - i\pi\delta(x-x_0),$$

where $\mathcal{P}$ is identifies the principal value, we get the spectral representation of the retarded Green's function

$$S_{A,A^\dagger}(\omega) = -\frac{1}{\pi}\Im(G^{\text{ret}}_{A,A^\dagger}(\omega)).$$

Appendix D

Continued Fraction Method

The upper part of the Green's function is defined as

$$\begin{aligned} G^U_{A,A^\dagger}(\omega + i\eta + E_0) &= \langle\psi_0|A\left(\omega + i\eta + E_0 - H\right)^{-1}A^\dagger|\psi_0\rangle \\ |u_0\rangle &= \left(\langle\psi_0|AA^\dagger|\psi_0\rangle\right)^{-\frac{1}{2}}A^\dagger|\psi_0\rangle \\ |u_n\rangle &= H^n|u_0\rangle. \\ \Rightarrow G^U_{A,A^\dagger}(\omega + i\eta + E_0) &= \cfrac{\langle\psi|AA^\dagger|\psi\rangle}{z - a_0 - \cfrac{b_1^2}{z - a_1 - \cfrac{b_2^2}{z - a_2 - \dots}}}. \end{aligned}$$

Now we consider

$$(z - H)(z - H)^{-1} = Id.$$

If we express this in the basis of $|u_n\rangle$, then

$$\begin{aligned} \sum_n (z - H)_{mn}(z - H)^{-1}_{np} &= \delta_{mp}. \\ \text{Thus, for } p = 0, \\ \sum_n (z - H)_{mn}x_n &= \delta_{m0} \\ \text{with } x_n &= (z - H)^{-1}_{n0}. \\ \Rightarrow x_0 &= \langle u_0|(z - H)^{-1}|u_0\rangle. \end{aligned}$$

Cramer's rule:

$$\begin{aligned} &\text{If } Ax = b \\ &\Rightarrow\ x_i = \frac{\det(A_i)}{\det(A)}, \end{aligned}$$

where A_i is the matrix A where the ith column is replaced by b.

$$\begin{aligned}
\Rightarrow\ x_0 &= \frac{\det(B_0)}{\det(z-H)} \\
&= \frac{\det(D_1)}{(z-a_0)\det(D_1)+b_1\det(D_2)} = \frac{1}{z-a_0+b_1\frac{\det(D_2)}{\det(D_1)}}. \\
\frac{\det(D_2)}{\det(D_1)} &= \frac{-b_1\det(E_2)}{(z-a_1)\det(E_2)+b_2\det(E_3)}. \\
\Rightarrow x_0 &= \cfrac{1}{z-a_0-\cfrac{b_1^2}{z-a_1-b_2\cfrac{\det(E_3)}{\det(E_2)}}}
\end{aligned}$$

with:

$$B_0 = \begin{pmatrix} 1 & -b_1 & 0 & \cdots \\ 0 & z-a_1 & -b_2 & \\ 0 & -b_2 & z-a_2 & \\ \vdots & & & \ddots \end{pmatrix},$$

$$D_1 = \begin{pmatrix} z-a_1 & -b_2 & 0 & \cdots \\ -b_2 & z-a_2 & -b_3 & \\ 0 & -b_3 & z-a_3 & \\ \vdots & & & \ddots \end{pmatrix},$$

$$D_2 = \begin{pmatrix} -b_1 & -b_2 & 0 & \cdots \\ 0 & z-a_2 & -b_3 & \\ 0 & -b_3 & z-a_3 & \\ \vdots & & & \ddots \end{pmatrix},$$

$$E_1 = \begin{pmatrix} z-a_2 & -b_3 & 0 & \cdots \\ -b_3 & z-a_3 & -b_4 & \\ 0 & -b_4 & z-a_4 & \\ \vdots & & & \ddots \end{pmatrix},$$

$$\text{and } E_2 = \begin{pmatrix} -b_2 & -b_3 & 0 & \cdots \\ 0 & z-a_3 & -b_4 & \\ 0 & -b_4 & z-a_4 & \\ \vdots & & & \ddots \end{pmatrix}.$$

Bibliography

[1] H. Benthien and E. Jeckelmann. Spin and charge dynamics of the one-dimensional extended hubbard model. *Physical Review B (Condensed Matter and Materials Physics)*, 75(20):205128, 2007.

[2] Anders W. Sandvik, Leon Balents, and David K. Campbell. Ground state phases of the half-filled one-dimensional extended hubbard model. *Physical Review Letters*, 92(23):236401, 2004.

[3] Reinhard M. Noack and Salvatore R. Manmana. Diagonalization- and numerical renormalization-group-based methods for interacting quantum systems. In Adolfo Avella and Ferdinando Mancini, editors, *LECTURES ON THE PHYSICS OF HIGHLY CORRELATED ELECTRON SYSTEMS IX: Ninth Training Course in the Physics of Correlated Electron Systems and High-Tc Superconductors*, volume 789. AIP, 2005.

[4] Steven R. White. Density matrix formulation for quantum renormalization groups. *Phys. Rev. Lett.*, 69(19):2863–2866, Nov 1992.

[5] Steven R. White. Density-matrix algorithms for quantum renormalization groups. *Phys. Rev. B*, 48(14):10345, 1993.

[6] Attila Szabo and Niels S. Ostlund. *Modern Quantum Chemistry: Introduction to Advanced Electronic Structure Theory.* McGraw-Hill, 1989.

[7] M. Born and R. Oppenheimer. Zur quantentheorie der moleküle. *Annalen der Physik*, 4(84):457–484, 1927.

[8] Neil W. Ashcroft and David N. Mermin. *Solid State Physics.* Thomson Learning, January 1976.

[9] Martin C. Gutzwiller. Effect of correlation on the ferromagnetism of transition metals. *Phys. Rev. Lett.*, 10(5):159–162, Mar 1963.

[10] Junjiro Kanamori. Electron correlation and ferromagnetism of transition metals. *Progress of Theoretical Physics*, 30(3):275–289, 1963.

[11] J. Hubbard. Electron correlations in narrow energy bands. *Proc. Roy. Soc. A*, 276(1365):238–257, Nov 1963.

[12] P. W. ANDERSON. The Resonating Valence Bond State in La2CuO4 and Superconductivity. *Science*, 235(4793):1196–1198, 1987.

[13] Elliott H. Lieb and F. Y. Wu. Absence of mott transition in an exact solution of the short-range, one-band model in one dimension. *Phys. Rev. Lett.*, 20(25):1445–1448, Jun 1968.

[14] Satoshi Ejima and Satoshi Nishimoto. Phase diagram of the one-dimensional half-filled extended hubbard model. *Phys. Rev. Lett.*, 99(21):216403, 2007.

[15] S. R. Manmana, V. Meden, R. M. Noack, and K. Schönhammer. Quantum critical behavior of the one-dimensional ionic hubbard model. *Phys. Rev. B*, 70(15):155115, Oct 2004.

[16] Shu-Sa Deng, Shi-Jian Gu, and Hai-Qing Lin. Block-block entanglement and quantum phase transitions in the one-dimensional extended hubbard model. *Physical Review B (Condensed Matter and Materials Physics)*, 74(4):045103, 2006.

[17] R. E. Peierls. *Quantum Therory of Solids.* Oxford University Press, 1955.

[18] S. Daul and R. M. Noack. Phase diagram of the half-filled hubbard chain with next-nearest-neighbor hopping. *Phys. Rev. B*, 61(3):1646–1649, Jan 2000.

[19] G. I. Japaridze, R. M. Noack, D. Baeriswyl, and L. Tincani. Phases and phase transitions in the half-filled t-t' hubbard chain. *Physical Review B (Condensed Matter and Materials Physics)*, 76(11):115118, 2007.

[20] L. D. Landau. Theory of fermi-liquids. *Sov. Phys. JETP*, 1957.

[21] Thierry Giamarchi. *Quantum Physics in One Dimension.* Oxford Science Publications, 2004.

[22] Florian Gebhard. *The Mott Metal-Insulator Transition.* Springer, 1997.

[23] J M Kosterlitz and D J Thouless. Ordering, metastability and phase transitions in two-dimensional systems. *Journal of Physics C: Solid State Physics*, 6(7):1181–1203, 1973.

[24] Subir Sachdev. *Qunatum Phase Transitions.* Cambridge University Press, 1999.

[25] J.M. Yeomans. *Statistical Mechanics of Phase Transtions.* Oxford Science Publications, 1992.

[26] William K. Wootters. Entanglement of formation of an arbitrary state of two qubits. *Phys. Rev. Lett.*, 80(10), Mar 1998.

[27] G. Vidal and R. F. Werner. Computable measure of entanglement. *Phys. Rev. A*, 65(3), Feb 2002.

[28] John Preskill. Lecture notes for physics 229: Quantum information and computation, 1998.

[29] Ö. Legeza and J. Sólyom. Two-site entropy and quantum phase transitions in low-dimensional models. *Phys. Rev. Lett.*, 96(11):116401, 2006.

[30] Jörg Rissler, Reinhard M. Noack, and Steven R. White. Measuring orbital interaction using quantum information theory. *Chemical Physics*, 323:519, Apr 2006.

[31] Shi-Jian Gu, Shu-Sa Deng, You-Quan Li, and Hai-Qing Lin. Entanglement and quantum phase transition in the extended hubbard model. *Phys. Rev. Lett.*, 93(8), 2004.

[32] Ö. Legeza and J. Sólyom. Optimizing the density-matrix renormalization group method using quantum information entropy. *Phys. Rev. B*, 68(19), Nov 2003.

[33] G. Vidal, J. I. Latorre, E. Rico, and A. Kitaev. Entanglement in quantum critical phenomena. *Phys. Rev. Lett.*, 90(22), Jun 2003.

[34] J. T. Stewart, J. P. Gaebler, and D. S. Jin. Using photoemission spectroscopy to probe a strongly interacting fermi gas. *Nature*, 454, 2008.

[35] C. Lanczos. An iteration mathod for the solution of the eigenvalue problem of linear differential and integral operators. *Journal of Research of the National Bureau of Standards*, 45, 1951.

[36] Ernest R. Davidson. The iterative calculation of a few of the lowest eigenvalues and corresponding eigenvectors of large real-symmetric matrices. *Journal of Computational Physics*, 17(1), 1975.

[37] Gerard L. G. Sleijpen, Albert G. L. Booten, Diederik R. Fokkema, and Henk A. van der Vorst. Jacobi-davidson type methods for generalized eigenproblems and polynomial eigenproblems. *BIT Numerical Mathematics*, Sep. 1996.

[38] John Cardy. *Scaling and Renormalization in Statistical Physics*. Cambride Lecture Notes in Physics, 1996.

[39] Kenneth G. Wilson. The renormalization group: Critical phenomena and the kondo problem. *Rev. Mod. Phys.*, 47(4), Oct 1975.

[40] I. Peschel, X. Wang, M. Kaulke, and K. Hallberg, editors. *Density-Matrix Renormalization - A New Numerical Method in Physics*. Springer Verlag, 1999.

[41] S. R. White and R. M. Noack. Real-space quantum renormalization groups. *Phys. Rev. Lett.*, 68(24):3487–3490, Jun 1992.

[42] Ö. Legeza, J. Röder, and B. A. Hess. Controlling the accuracy of the density-matrix renormalization-group method: The dynamical block state selection approach. *Phys. Rev. B*, 67(12):125114, Mar 2003.

[43] Stellan Östlund and Stefan Rommer. Thermodynamic limit of density matrix renormalization. *Phys. Rev. Lett.*, 75(19):3537–3540, Nov 1995.

[44] F. Verstraete and J. I. Cirac. Matrix product states represent ground states faithfully. *Physical Review B (Condensed Matter and Materials Physics)*, 73(9):094423, 2006.

[45] F. Verstraete and J.I. Cirac. Renormalization algorithms for quantum-many body systems in two and higher dimensions. arXiv:cond-mat/0407066.

[46] Norbert Schuch, Michael M. Wolf, Frank Verstraete, and J. Ignacio Cirac. Computational complexity of projected entangled pair states. *Physical Review Letters*, 98(14):140506, 2007.

[47] U. Schollwöck. The density-matrix renormalization group. *Rev. Mod. Phys.*, 77(1):259–315, Apr 2005.

[48] Ian P McCulloch. From density-matrix renormalization group to matrix product states. *Journal of Statistical Mechanics: Theory and Experiment*, 2007(10):P10014, 2007.

[49] C. Eckart and G. Young. *The approximation of one matrix by another of lower rank.* Psychometrika, 1936.

[50] G. W. Stewart. On the early history of the singular value decomposition. *SIAM Review*, 35(4):551–566, 1993.

[51] Shoudan Liang and Hanbin Pang. Approximate diagonalization using the density matrix renormalization-group method: A two-dimensional-systems perspective. *Phys. Rev. B*, 49(13):9214–9217, Apr 1994.

[52] R. M. Noack, S. R. White, and D. J. Scalapino. Correlations in a two-chain hubbard model. *Phys. Rev. Lett.*, 73(6):882–885, Aug 1994.

[53] Norbert Schuch, Michael M. Wolf, Frank Verstraete, and J. Ignacio Cirac. Computational complexity of projected entangled pair states. *Physical Review Letters*, 98(14):140506, 2007.

[54] Steven R. White and Adrian E. Feiguin. Real-time evolution using the density matrix renormalization group. *Phys. Rev. Lett.*, 93(7):076401, Aug 2004.

[55] Marlis Hochbruck and Christian Lubich. On Krylov subspace approximations to the matrix exponential operator. *SIAM Journal on Numerical Analysis*, 34(5):1911–1925, 1997.

[56] Masuo Suzuki. Relationship between d-dimensional quantal spin systems and (d+1)-dimensional ising systems equivalence, critical exponents and systematic approximants of the partition function and spin correlations . *Prog. Theor. Phys.*, 56(5):1454–1469, 1976.

[57] Elbio Dagotto. Correlated electrons in high-temperature superconductors. *Rev. Mod. Phys.*, 66(3):763–840, Jul 1994.

[58] Till D. Kühner and Steven R. White. Dynamical correlation functions using the density matrix renormalization group. *Phys. Rev. B*, 60(1):335–343, Jul 1999.

[59] Eric Jeckelmann. Dynamical density-matrix renormalization-group method. *Phys. Rev. B*, 66(4):045114, Jul 2002.

[60] E. Jeckelmann, F. Gebhard, and F. H. L. Essler. Optical conductivity of the half-filled hubbard chain. *Phys. Rev. Lett.*, 85(18):3910–3913, Oct 2000.

[61] Steven R. White and Ian Affleck. Spectral function for the s = 1 heisenberg antiferromagetic chain. *Physical Review B (Condensed Matter and Materials Physics)*, 77(13):134437, 2008.

[62] A. V. Oppenheim, R. W. Schafer, and J. R. Buck. *Discrete-time signal processing*. Prentice Hall, 1999.

[63] P. Gambardella, A. Dallmeyer, K. Maiti, M. C. Malagoli, W. Eberhardt, K. Kern, and C. Carbone. Ferromagnetism in one-dimensional monatomic metal chains. *Nature*, 416(6878):301–304, Mar. 2002.

[64] Xinluo Zhao, Yoshinori Ando, Yi Liu, Makoto Jinno, and Tomoko Suzuki. Carbon nanowire made of a long linear carbon chain inserted inside a multiwalled carbon nanotube. *Phys. Rev. Lett.*, 90(18):187401, May 2003.

[65] Michael Springborg. Quasi-one-dimensional materials: polymers and chains. *Journal of Solid State Chemistry*, 176(2):311–318, 2003.

[66] Seiichi Kagoshima, Hiroshi Nagasawa, and Takashi Sambongi. *One-Dimensional Conductors*. Springer Verlag, 1988.

[67] V. G. Lifshits, Alexander A. Saranin, A. V. Zotov, and M. Katayama. *Surface Science: An Introduction*. Springer Verlag, 2003.

[68] S. Glocke, A. Klümper, and J. Sirker. Half-filled one-dimensional extended hubbard model: Phase diagram and thermodynamics. *Physical Review B (Condensed Matter and Materials Physics)*, 76:155121, 2007.

[69] N. Laflorencie, E. S. Sørensen, M.-S. Chang, and I. Affleck. Boundary effects in the critical scaling of entanglement entropy in 1d systems. *Phys. Rev. Lett.*, 96(100603), 2006.

[70] Ö. Legeza, J Sólyom, L. Tincani, and R. M. Noack. Entropic analysis of quantum phase transitions from uniform to spatially inhomogeneous phases. *Phys. Rev. Lett.*, 99(11):087203, 2007.

[71] Ö. Legeza and J. Sólyom. Quantum data compression, quantum information generation, and the density-matrix renormalization-group method. *Phys. Rev. B*, 70(20):205118, 2004.

[72] P. G. J. van Dongen. Extended hubbard model at strong coupling. *Phys. Rev. B*, 49(12):7904–7915, Mar 1994.

[73] R. Claessen, M. Sing, U. Schwingenschlögl, P. Blaha, M. Dressel, and C. S. Jacobsen. Spectroscopic signatures of spin-charge separation in the quasi-one-dimensional organic conductor ttf-tcnq. *Phys. Rev. Lett.*, 88(9):096402, Feb 2002.

[74] H. W. Yeom, Y. K. Kim, E. Y. Lee, K.-D. Ryang, and P. G. Kang. Robust one-dimensional metallic band structure of silicide nanowires. *Phys. Rev. Lett.*, 95(20):205504, Nov 2005.

[75] Eric Jeckelmann. Optical excitations in a one-dimensional mott insulator. *Phys. Rev. B*, 67(7):075106, Feb 2003.

[76] K. W. Kim, G. D. Gu, C. C. Homes, and T. W. Noh. Bound excitons in Sr_2CuO_3. *Physical Review Letters*, 101(17):177404, 2008.

[77] M. Aichhorn, H. G. Evertz, W. von der Linden, and M. Potthoff. Charge ordering in extended hubbard models: Variational cluster approach. *Phys. Rev. B*, 70(23):235107, Dec 2004.

Danksagung

Zunächst danke ich meinem Doktorvater Prof. Reinhard Noack. Ohne die Aufnahme in seine Arbeitsgruppe, sowie seinen ausführlichen Erklärungen und Ratschlägen, insbesondere während meiner Einarbeitungszeit, wäre diese Arbeit nicht möglich gewesen.
Auch der restlichen Arbeitsgruppe, Dr. habil. Jörg Bünemann, Dipl. Phys. Tobias Schickling und Prof. Dr. Florian Gebhard, gilt mein Dank für wiederholte Diskussion und eine gute Arbeitsatmosphäre. Ein besondere Dank geht hier an Dipl. Phys. Daniel Ruhl, der mir durch sein fortwährendes Interesse, sowie eine immer vorhandene Diskussions- und Erklärungsbereitschaft eine ständige Reflexionsmöglichkeit und ein deutlich besseres Verständiss vieler Sachverhalte ermöglichte.
Last but not least gilt mein Dank meinen Eltern Inge und Klaus Mund, sowie all meinen Freunden, für ihre beständige seelische und moralische Unterstützung während der gesamten Promotionszeit.

Lebenslauf

Persönlich Daten

Name: Cornelius Mund

Adresse: Wendelgasse 2
35037 Marburg
Deutschland

Geburtsdatum: 15.07.1982

Tel.: +49 6422 897359

eMail: Cornelius.Mund@physik.uni-marburg.de

Ausbildung

Name der Institution	**Abschluss**	**von - bis**
Stiftsschule St. Johann Amöneburg	Abitur	7/93 - 06/02
Philipps Universität Marburg	Vordiplom	4/03 - 10/04
Philipps Universitat Marburg	(weiteres Studium der Physik)	11/04 - 8/05
University of Massachusetts Dartmouth	Master of Science	9/05 - 9/06
Philipps Universität Marburg	Promotion	10/06 - 12/09

Arbeitsverhltnisse

Arbeitgeber	**von - bis**
Grundwehrdienst	07/02 - 03/03
Wissenschaftlicher Mitarbeiter	11/06 - 12/09

Marburg, December 14, 2009